Particle Beaching: A Study on the Transport of Buoyant Microplastics in the Swash Zone

Carlos Abarca

A dissertation
submitted in partial fulfillment of the
requirements for the degree of

Doctor of Philosophy

University of Washington

2026

Reading Committee:

Michelle DiBenedetto, Chair

Alberto Aliseda, Chair

Brian Polagye

Program Authorized to Offer Degree:
Mechanical Engineering

University of Washington

Abstract

Particle Beaching: A Study on the Transport of Buoyant Microplastics in the Swash Zone

Carlos Abarca

Co-Chairs of the Supervisory Committee:
Michelle DiBenedetto
Mechanical Engineering

Alberto Aliseda
Mechanical Engineering

Predicting the transport of microplastics on beaches is critical to modeling plastic pollution in coastal environments. The transport of these particles is dependent on the particle characteristics and local swash zone hydrodynamics. The swash zone is the region where broken waves travel up and down the beach's slope. Individual swash events are capable of transporting microplastic particles, as well as sediments. To study microplastics, some previous experiments studied small particles in continuous wave forcing in wave tanks. While these studies can measure particle transport after a number of waves, they are unable to isolate the interactions between one wave and one particle. In this dissertation, we focus on simplifying the study of microplastics in the swash zone. Specifically, we consider the transport of buoyant microplastics in a single swash event, where we can isolate the swash zone's role in transporting buoyant plastic particles onto and off of beaches.

In Chapter 2, we designed an experimental wave tank that isolates small swash-like flows; using this tank, we tracked disk-shaped particles which were initially placed on the beach. Our observations showed that smaller particles were carried higher up the beach during the uprush phase of a single swash event, and that they were more

likely to remain on the shore after backwash. In contrast, larger particles had reduced uprush transport and were more likely to leave the beach. We explain these results by calculating the Stokes number at the instant the wave first impacts each particle. We find that this Stokes number correlates with both the maximum and final beaching positions of the particles. Lower-inertia particles generally stayed near the swash front during uprush, leading to high maximum positions and resulting in higher beaching locations. In contrast, higher-inertia particles lagged behind the swash front, leading to lower maximum and final positions and had a greater likelihood of returning to the water. These findings demonstrate the importance of particle inertia to buoyant particle transport in the swash zone.

In Chapter 3, we develop a statistical model to predict particle residence times on beaches and the evolution of the distribution of particle positions across multiple waves. This model uses empirically-derived beaching probabilities from our laboratory experiments for a single swash event. Our simulations results show that buoyant particles continuously leave the beach, such that the particle count decreases exponentially over time. We use an exponential fit to particle count over time to estimate the average residence time of particles on the beach in our simulations. With our simulations, we find that residence time decreases with increasing particle size and decreasing average wave run-up length. We characterize this relation with the average particle Stokes number, where we find that the residence time of particles on the beach decreases with increasing Stokes number. We observe that particles that on the beach are generally transported to high positions where they form a wrack line. Over time, the largest run-ups will move the wrack line farther up the beach. Finally, we also consider the relative effect of tides, where we find that falling tides lead to particles having higher residence times on the beach, whereas rising tides reduce particle residence times on the beach. Overall, our simulations provide a useful tool for describing buoyant particle transport on a beach under variable wave forcing.

In Chapter 4, we review and analyze the relevant forces for the incipient motion of buoyant microplastics in the swash zone. This work provides a short review on sediment incipient motion, highlighting the challenges when extending to buoyant microplastics in the swash. In our analysis, we focus on identifying a characteristic timescale of microplastic incipient motion considering the effects of lubrication and drag. We define a lubrication timescale by scaling the lubrication force with net buoyancy of the particle. The timescale due to drag is characterized by the particle relaxation time, which is the time it takes for a particle to go with a surrounding flow. We find these due timescales differ with particle and flow characteristics. Moreover, we compare both estimates with a timescale derived from experiments, and find that relaxation time scales closer with our experimental values compared to the lubrication timescale. This suggests that buoyant particles on a beach may be easily mobilized by incoming swash waves. Overall, this work highlights the need to accurately describe the incipient motion for buoyant particles, as well as presents an analysis of timescales derived from relevant forces in the system for disks on an impermeable beach. Finally, in Chapter 5, we summarize the contributions from this thesis and describe some important avenues for future work.

TABLE OF CONTENTS

Page

LIST OF FIGURES

LIST OF TABLES

ACKNOWLEDGMENTS

This PhD would never have been possible without the people in my life who support me each and every day.

First, I want to start by thanking my advisor Michelle. Michelle has supported me through all the trials that come with the PhD. She was an important role model, advisor, and friend to have in my corner. Her joy when talking about science was inspiring and motivating, and she pushed me in right ways so I could become a better researcher. Michelle, I am honored that I am one of your first PhD students, and the best part about it was getting to watch your growth as an advisor. I am excited to see what the future holds for you and the lab. Additionally, I would also like to acknowledge my committee members, Alberto Aliseda, Brian Polagye, Chris Chickadel, Christie Hegermiller, and Melissa Moulton (an honorary committee member), for helping me along the way, and always being there to talk about science or life.

I would like to acknowledge the DiBen Lab. My fellow lab members have been nothing but supportive. I appreciate all the times we have had laughing and sharing research together. I want to especially shout out undergrads who helped with experiments: Aaron and Tong. Both were fundamental in getting my experiments done and I know they are thriving in their future endeavors. To Lou, Julio, and Helena, I cannot thank you guys enough for not only supporting me through my research, but also being my friends. I am thankful for the memories we've made and the amount we've learned from each other. I am proud of all of you and I know you guys are going to continue to be amazing in anything you do. Also never forget the Husky

Dawg Dash, what an exhilarating race.

Next, I want to shout out members of the mechanical engineering department. The Polagye lab was very helpful to my development and transition to UW. They were very welcoming and some of the first students that I met at UW. I also want to acknowledge the MEGA org. I was honored to serve as a social chair for them. The officers and members of MEGA, past and present, have been awesome friends and people to talk to. I especially want to shout out my fellow social chair Mia. She has been a close friend since my first day in grad school. I am thankful for her support, her jokes, and for keeping me accountable to finish this thesis!

To the EFM group, I am thankful for all the memories. I never met a group of people who are so motivated by their research and so supportive of one another. I am thankful for the senior students who provided a welcoming environment for me when I first joined, and I hope I provided the same environment to those who have come after me. I know that the future of environmental fluid mechanics is in good hands. I wish I could be just as confident in the Bernoulli Brigade, but I hope you guys win a championship in some intramural sport!

First of all, I would like to thank the Millennium Scholars Program at Penn State for introducing me to research and providing endless support in my pursuit of excellence. I am thankful for Margaret Byron for allowing me to join her lab as a freshman and pushing me to be the best researcher I could be. I especially want to thank my cohort for being my community at Penn State. You are all so inspirational and I know that cohort 5 has a bond that will last forever.

To my crew outside of science, Bruce and the gang as we are known. You guys have accepted me for who I am from day one, and I cannot thank you enough for being my friends. I have missed y'all a lot since I've been in Seattle, but no matter how long it has been you have always supported me and picked me up when I was down. So thank you all from the bottom of my heart!

To my other friends from home, you have been here form the very beginning and seeing how you all have grown has been amazing to watch. As time has gone on, I am always reminded how lucky I am to call you my friends. You have kept me sane when I was stressed, and always remind me of who I am and what I am capable of.

To my family both in the Pennsylvania and Costa Rica, I am happy to say that your endless love and support has powered me through to get this degree. I know the sacrifices and effort you have put in to allow me to be where I am today, and I am grateful for you all. And to my younger cousins, I hope I can be a role model to you all and I know you are all going to be amazing.

To my parents, I cannot thank you enough for what you have done to allow me to be here. And not just allow me to be here, but allow me to be me. You have taught me to fight for my place and to be unapologetically myself. The work you have put in does not go unnoticed and everything that I do is to make you proud. I love you both very much.

To my brother Cristian, you are my best friend. You have pushed me to be the best version of myself each and every day. You are my biggest role model and someone I will always look up to and respect. I can't even describe the amount of pride I have in saying you're my brother. I appreciate you being my Marvel Rivals duo and fellow peak enjoyer. I love you brother, and I'm grateful for every conversation and laugh we have.

I was supported by the Department of Defense (DoD) through the National Defense Science & Engineering Graduate (NDSEG) Fellowship Program. Specifically, this funding was through the Office of Naval Research (ONR). I am thankful for the support to not only do research, but also present at the NDSEG conference.

Chapter 1
INTRODUCTION

1.1 Introduction

Plastic pollution is a growing threat to the health of ocean ecosystems (Landrigan et al., 2020), with studies estimating that up to 20 million metric tons of plastic enter the oceans annually (Borrelle et al., 2020; Jambeck et al., 2015). In particular, microplastics, which are plastics smaller than 5 mm, are especially troublesome as they infiltrate and spread throughout ocean ecosystems (Critchell et al., 2016; Sebille et al., 2020; Thornton et al., 1998). Given the widespread presence of ocean microplastics, predicting their transport is essential to effectively address this problem.

Closing the plastic mass balance in the ocean is still a challenge. One uncertainty is boundary conditions, including sources and sinks. While the ocean is a significant plastic reservoir, it is not a permanent sink; e.g., plastic is frequently observed washing up on beaches (Chubarenko, Bagaev, et al., 2016; Corcoran et al., 2020; Rey et al., 2021). Beyond observations, high rates of ocean plastic beaching have also been predicted in global simulations (Chassignet et al., 2021; Onink et al., 2021). Thus, beaches act as a sink for microplastics and larger debris, such as meso- and macroplastics (Hinata, Mori, et al., 2017; Isobe et al., 2014). Plastic debris trapped on a beach can undergo accelerated degradation and fragmentation because of exposure to high levels of solar radiation and continuous wave forcing (Barnes, Galgani, et al., 2009; Efimova et al., 2018; Esiukova et al., 2026). As a result, fragmentation of larger marine plastic debris on beaches leads to the creation of 'secondary' microplastics, demonstrating how a beach can also serve as a source of ocean microplastic pollution. Along with 'secondary' microplastic formation, land-based microplastic sources include river outflows and local littering (Lebreton et al., 2017). In summary, beaches serve as both a source and a sink for microplastics in the ocean, and therefore understanding transport along beaches is crucial for informing and mitigating widespread microplastic pollution.

Global models cannot resolve nearshore processes that control particle transport on beaches. Therefore, these models tend to use simplified coastal boundary conditions, such as a fixed probability of beaching that depends on distance to coastline (Chassignet et al., 2021; Onink et al., 2021). *Beaching* is here defined as the process of a particle settling on a beach. This process is dictated by swash zone flows — the wave-driven flows traveling up and down a beach. Therefore, this current work is motivated to address the knowledge gap: how are microplastics transported in the swash zone?

This dissertation is focused on plastic transport and beaching in swash flows, primarily focused on particles that start on a beach and are impacted by incoming waves. In the remainder of Chapter 1, we further describe the swash zone, sediment transport in the swash zone, and review previous works that focus on microplastics in relevant flows. Next, we highlight our work that was designed to address the current knowledge gaps. In Chapter 2, we design experiments where we track particles in a swash flow to study the transport of buoyant particles on an impermeable beach. We ultimately find that particle transport is highly dependent on particle inertia. While these experiments are for a single swash event, Chapter 3 presents a statistical model to predict particle transport across many swash events. In this model, particle beaching is empirically derived from our experiments from Chapter 2. In Chapter 4, we study the incipient motion of a buoyant particle in the swash. We start with a review of the incipient motion of particles generally and then analyze the importance of lubrication to buoyant microplastics incipient motion in the swash zone. Finally, Chapter 5 summarizes the findings of this dissertation and discusses potential future work.

1.2 Background

1.2.1 Swash zone

The swash zone is the region on a beach where broken waves travel up and down the slope as a swash bore in an approximately ballistic motion (Peregrine, 1983). This ballistic motion can be divided into three phases: uprush, flow reversal, and backwash. Uprush is the initial phase where the swash bore travels up the beach, decelerating due to gravity and friction until it reaches its maximum position on the beach, known as wave run-up. At wave run-up, the transitional phase of flow reversal starts as it begins to traverse down the slope. This downward motion signifies the start of backwash, the final phase of a swash event (Masselink and Puleo, 2006). Wave run-up on a beach is determined by local factors such as the mean water level, the beach morphology, and the incident waves. The area around the wave run-up is often referred to as the wrack line or wrack zone because it is where dead vegetation (wrack) and debris are observed to accumulate (Thornton et al., 1998; Wickham et al., 2020). While plastic debris is also found to accumulate by the wrack line, field studies routinely find plastic all across beaches, including between the wrack line and the mean water line (Battisti et al., 2020; Cesarini et al., 2021; Chubarenko, Esiukova, et al., 2018; Chubarenko, Krivoshlyk, et al., 2024; Guerrero-Meseguer et al., 2020). This suggests that plastic particles may be constantly moving throughout the swash zone under wave action, rather than accumulating only in one area.

To understand how plastics may be constantly transported, we need to understand the local fluid mechanics of the swash zone. To illustrate, we present an example of a swash bore climbing a sloped boundary in Figure 1.1 (Baldock, Grayson, et al., 2014). To model this type of flow, previous work utilizes nonlinear shallow water wave equations to estimate positions and velocities of the swash bore front, or shoreline

(Hughes and Baldock, 2004; Shen et al., 1963). The initial shoreline velocity at the beginning of uprush has been used to derive the wave run-up (Shen et al., 1963; Yeh et al., 1989), along with other parameters such as beach slope, gravity, and friction. In the swash bore, the fluid velocity is highest on the surface and decays with depth (O'Donoghue et al., 2010), causing fluid convergence towards the swash bore front (Baldock, Grayson, et al., 2014). Therefore, particles experience different fluid velocities dependent on where they are in the water column, i.e., particles on the surface converge towards the shoreline. Particles can be stirred and suspended in a swash bore's water column due to turbulence. During uprush, swash bores can be quite turbulent depending on the wave breaking dynamics in the surf zone (Lanckriet et al., 2013). Along with bore-generated turbulence from wave breaking, local turbulence generation is driven by bed shear stress. However, swash flows are highly dissipative; thus, as uprush continues, turbulence dissipation rates exceed local production. As the swash bore approaches flow reversal, bore-generated turbulence is completely dissipated (Kim et al., 2017). Overall, swash zone hydrodynamics vary across the swash bore depth and between swash phases. Thus, it is important to consider these variations when estimating particle transport in the swash zone.

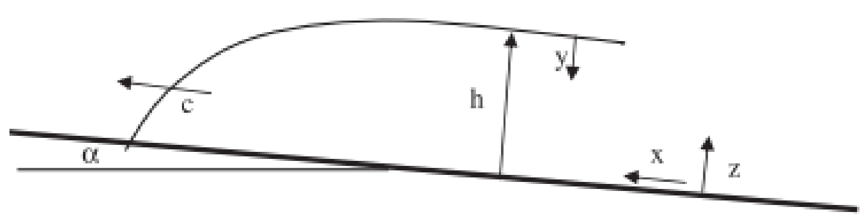

Figure 1.1: Example schematic of a swash bore traveling up a slope, provided by Baldock, Grayson, et al. (2014)

1.2.2 Sediment transport in the swash zone

The study of small particle dynamics in the swash zone has historically been concerned with sediment transport. Generally, sediment transport can be categorized as either the transport of suspended sediment concentrations or bedload concentrations. Suspended sediment concentrations refer to the sediments that are suspended in the water column, while bedload concentrations refer to sediments that remain close to the bed and are transported as a 'sheet'. In the swash zone, these concentrations and subsequent transport can vary across swash phases. At the onset of uprush, suspended sediment concentrations increase rapidly (Alsina and Cáceres, 2011; Masselink, Evans, et al., 2005; Masselink and Puleo, 2006; Puleo, Blenkinsopp, et al., 2014), due to rising water levels and high levels of bore-generated turbulence, which stir and suspend sediments (Alsina, Falchetti, et al., 2009; Brocchini et al., 2008; Guard et al., 2007). As uprush continues, bed shear stress mobilizes particles near the bed, thus increasing bedload concentrations, which can even exceed suspended concentrations (Lanckriet et al., 2013; Puleo, Blenkinsopp, et al., 2014; Puleo, Lanckriet, et al., 2015). Despite large bedload concentrations during uprush, the resultant 'sheet' transport is low compared to the transport of suspended sediment concentrations, which is primarily due to high flow velocities and turbulence in the water column (Puleo, Lanckriet, et al., 2015; Ruju et al., 2016).

As the bore reaches flow reversal, flow velocities and bore-generated turbulence dissipate. This results in both suspended and bedload concentrations approaching zero. At the start of backwash, suspended sediment concentrations start to increase again, although they remain low compared to those during uprush (Hughes and Moseley, 2007; Masselink, Evans, et al., 2005; Masselink and Puleo, 2006; Puleo, Lanckriet, et al., 2015; Ruju et al., 2016). Bedload concentrations also rise during backwash, as bed shear stress increases. As opposed to uprush, the primary driver of turbulence in backwash is bed shear stress, which results in increased transport of bedloads, such that 'sheet' transport exceeds suspended concentration transport (Puleo, Lanckriet, et al., 2015; Ruju et al., 2016). Additionally, decreasing water levels along with lower flow velocities contribute to the total sediment transport of backwash, which is dominated by bedload concentrations.

While there exists a large body of research on sediment transport in the swash (e.g., see Chardón-Maldonado et al. (2016) for a review), sediment transport models cannot be directly applied to microplastic particles for two main reasons: (1) Sediment is much denser than water ($\rho_p/\rho_f \gg 1$ where ρ_p and ρ_f are the particle and fluid density, respectively), whereas microplastics are close to the density of water ($\rho_p/\rho_f \approx 1$) and can be either positively or negatively buoyant. (2) Suspended sediment can reach high enough concentrations to affect the flow via a two-way coupling, whereas microplastic concentrations in the ocean are low enough that a one-way coupling is an appropriate assumption. In this dissertation, we only consider buoyant particles. In contrast to sediment, which accumulates near the bottom of the water column, we expect buoyant particles to stay near the free surface of the swash flow. As stated in Section 1.2.1, swash flow velocities at the surface are faster than lower in the water column. This sheared flow means that we expect buoyant microplastics' transport to differ from sediment transport in a swash flow. This disparity between microplastics and sediment highlights the necessity for further research on microplastics transport in the swash zone.

1.2.3 Microplastics in the swash zone

The dynamics of microplastic transport in the swash zone are complex, as they depend on local hydrodynamics, the beach (e.g., sand grain size, beach slope), and the properties of the plastic particles themselves. A study by Critchell et al. (2016) aimed to identify influential factors of this coastal plastic transport. They suggest that the plastic source location, plastic quantities, and the debris resuspension are the most important; however, it is difficult to quantify some of these, given the limited physical knowledge of buoyant particle transport in a swash flow. Experimental field studies have provided some insight into the transport of buoyant plastics on beaches. Two field studies consisted of researchers deploying buoyant, marked objects (ranging from 1-13 cm in size) on a beach within the swash zone and surveying their locations over two years (Hinata, Mori, et al., 2017; Kataoka et al., 2015). These studies found that the objects' residence time on the beach increased with increasing object size. It was also observed that the larger, more buoyant objects were typically found higher on the beach. While these results highlight the importance of object size and buoyancy to plastic transport on beaches, these field studies only reveal long-term trends and do not provide insight into the interactions over a single wave period. Additionally, the objects in these studies were large, given that performing similar field experiments would be difficult with smaller particles. Therefore, studies on smaller particles have typically been conducted in the lab.

A number of laboratory experiments have studied particle transport in nearshore flows (Forsberg et al., 2020; Kerpen et al., 2020; Larsen et al., 2023; Núñez et al., 2023). These experiments all introduce small particles to a wave tank, run the wave tank over multiple wave cycles, and record the final particle positions (among other measurements of transport). There is some variation from study to study, e.g., the inclusion of sediment or wind. But overall, these studies also find that increasing particle buoyancy (often via decreasing particle density) correlates with an increasing likelihood of particles beaching. However, because each of these experimental setups included effects from nonbreaking waves, breaking waves in the surf zone, and swash waves, it is difficult to disentangle the separate effects of each flow. For example, only the most buoyant particles would be able to overcome the turbulent mixing in the surf zone and make it into the swash zone, which could be why buoyancy was found to be a controlling factor. Additionally, the majority of these studies focus on particle transport from the water to the beach, without considering transport from the beach to the water. The exception is Núñez et al. (2023) who also conducted experiment with particles that started on the beach. They found that the waves were able to remove the particles from the beach; however, they did not track individual particles and were therefore unable to precisely identify the controlling parameters. Thus, uncertainty remains surrounding what controls particle beaching behavior in the swash zone.

Alongside lab experiments, models have been developed to address the transport of microplastics in the swash zone. Hinata, Sagawa, et al. (2020) developed a statistical beaching model based on observations of the residence time of large (i.e., > 10 mm) debris on a beach Kataoka et al., 2013, 2015. The observed residence times, applicable for this particular size class, serve as model inputs to derive beaching and resuspension probabilities and simulate the particle count density on the beach over time. Because beaching probabilities are determined empirically from input resident times, it is uncertain how these probabilities will vary with different particles and wave conditions. Recent work by Mørk et al. (2026) applied a statistical model, validated with wave tank experiments, to predict the beaching process for particles in the nearshore region, defining a probability p for whether a beached particle will be washed off. Using their model, they predict the distribution of particles on a beach over time. However, the authors discuss how the beaching parameter p is still an unknown, and rather use it as a variable to tune. They suggest that it is a function of particle position on the beach, beach morphology, and wind, but they are unable to configure an exact function of p based on field observations in the literature. Thus, further work is needed to develop physics-informed parameterizations that describe beaching for generic particle and wave characteristics. Nevertheless, current nearshore statistical models (Hinata, Sagawa, et al., 2020; Mørk et al., 2026) provide an important framework for modeling the particle beaching process.

Chapter 2

EXPERIMENTAL STUDY OF BUOYANT PARTICLE TRANSPORT IN A SMALL SWASH FLOW

The work in this Chapter is Co-Authored by Tong Ling and Michelle DiBenedetto. Tong Ling helped with experimental setup and data collection. Michelle DiBenedetto provided insight for analysis and contributed to manuscript drafting and editing.

2.1 Motivation

Previous work, outlined in Chapter 1, focuses on the transport of positively buoyant particles in the swash zone. However, necessary future work is required to improve our understanding of the physics behind this transport. One recent study has been able to address some of these questions by considering inertial particle transport confined to within the swash zone (Davidson et al., 2023). The authors applied a modified Maxey-Riley equation (Maxey et al., 1983) to an ideal ballistic swash model (Shen et al., 1963), focusing on particles that start offshore in the water as they enter the swash flow. This model, validated by wave tank experiments, finds that particles with higher inertia were both more likely to beach and more likely to deposit higher on the beach. While this model provides insight into particle transport from the water to the beach in swash flows, it is still not clear how particle inertia will affect the transport of particles that initially start on the beach.

In Appendix A, we discuss our exploratory experiments to investigate open questions. While our preliminary study found trends with particle size and initial positions, we could not fully characterize the transport of the particles. Thus, we aim to expand on the exploratory experiments with a new set of experiments described in this chapter. The ultimate goal of this chapter is to understand what controls the fate of particles that begin on the beach. While previous studies that combined surf and swash dynamics identified particle buoyancy (often via density) as an important control parameter, these studies were unable to isolate the role of the swash itself. This suggests that buoyancy may govern whether particles reach the beach in the first place, but once they are already on the beach, other parameters may become more important. Therefore, in our experiments, we hold density constant and focus instead on particle size and inertia, which research suggests are central to particle transport in the swash zone (Davidson et al., 2023).

In the remainder of this paper, we first describe our methods in section 2.2, including an outline of our experimental setup and methods, a description of the flows, and relevant nondimensional parameters to the system. Then, we report and discuss our results in section 3.3 before ending with concluding thoughts in section 2.4.

2.2 Methods

In this section we first describe the experimental facility used in our study. We next describe the flow and the particles before ending with a summary of the relevant non-dimensional parameters.

2.2.1 Experimental facility

We designed and constructed a wave tank that generates a small-scale, swash-like flow, focusing specifically on the swash bore front. A schematic of the facility is depicted in Figure 2.1: the tank is 225 cm long, 30 cm wide, and 25 cm tall. It has a relatively narrow design to reduce alongshore variability, allowing us to focus on cross-shore forcing on the beach. Cross-shore position lies along the x-axis where $x = 0$ denotes the mean water line and $x > 0$ corresponds to the beach. We use disk-shaped particles as model plastics instead of spherical particles to avoid any effects from particles rolling. The beach is impermeable and made of acrylic which is set to a constant slope of $\beta = 1/10$. On top of the acrylic, we affixed a layer of black canvas which served two main purposes: it provided contrast for the particles in our images, and the canvas became hydrophilic once wet which minimized capillary instabilities in the swash bore front. We use an impermeable beach as it is approximately representative of a saturated beach where water flux into the beach can be close to zero (Kikkert et al., 2012; Steenhauer et al., 2011).

The tank is designed to generate one swash event at a time using a piston-type wavemaker. Each wave is initiated close to the shoreline, thus limiting the space it can freely propagate prior to breaking. Once it breaks on the slope, the broken wave travels up the slope to a point of maximum run-up. The goal of generating individual swash events is to simplify the complex particle-fluid interactions present in the swash zone. While on a real beach, a particle will often experience interacting swash waves, there is still limited research on how a buoyant particle is transported in a single swash event. Thus, we designed the study to isolate buoyant particle interactions with an individual swash event to build insight that can inform future experiments in more complex scenarios.

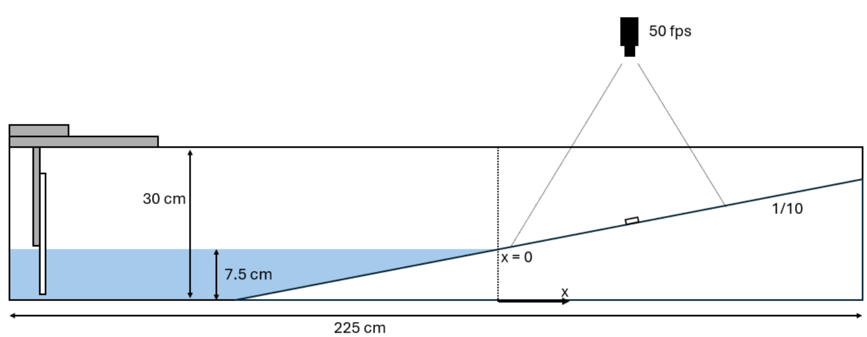

Figure 2.1: Side view schematic of experimental wave tank equipped with wave paddle and overhead camera. Not drawn to scale.

2.2.2 Flow description

We use an overhead camera (Basler boost R boA4096-93cm) to measure the shoreline position x_s, or swash bore front, over time. We show an example image from an experiment near the point of maximum run-up in Figure 2.2, where we see the shoreline is clearly visible and has some alongshore variation. By tracking this shoreline, we measure both how the shoreline evolves over time and the maximum run-up L for a given swash event. Note that we only measure x_s during uprush, as backwash is generally difficult to track given it does not typically have a well-defined front. In these experiments, we characterize wave cases using L: we generate three different wave cases, denoted as W1, W2, and W3, with measured maximum run-up lengths of $L = 0.33, 0.49$, and 0.70 m, respectively. These statistics are summarized in Table 2.1. In general, our experimental swash flows are small compared to well-documented swash studies (e.g., Stockdon et al. (2006)). While large, energetic swash flows (with run-ups on the order of 10 meters) are typically studied due to their ability to transport heavy sediment, buoyant microplastics can be mobilized by much weaker flows. Furthermore, a significant portion of marine plastic pollution originates from and is observed in coastal communities (Jambeck et al., 2015; Vianello et al., 2013), which are often characterized by protected coastlines (including bays, estuaries, and harbors) with naturally small waves. Because buoyant plastics will be transported in any flow capable of reaching them (that is also deep enough to suspend them), studying particle transport in a small swash flow is therefore relevant for understanding the fate of plastic pollution.

We show x_s as a function of time (defined here as the maximum cross-shore position in each frame) for our experimental wave cases in Figure 2.3, with the data representing the average of 20 experimental trials for each wave case. For reference, we compare our data to the swash model presented by Hughes and Baldock (2004). This model is an extension of the ballistic shoreline solution of Shen et al. (1963)

(originally derived for flow over an impermeable, uniformly-sloped beach), but with the additional effects of bed friction. The model predicts the shoreline position x_s and maximum run-up L for a single swash event. The model equations describing uprush are as follows:

$$x_s = \frac{2\delta}{f} \ln\left(\frac{\cos(At + B)}{\cos(B)}\right) \tag{2.1}$$

and

$$L = \frac{-2\delta}{f} \ln(\cos(B)), \tag{2.2}$$

where

$$A = -\sqrt{\frac{gf\sin(\beta)}{2\delta}}, \qquad B = \tan^{-1}\left(\frac{U_s\sqrt{f}}{\sqrt{2g\delta\sin(\beta)}}\right). \tag{2.3}$$

Here, f is the friction factor, δ is the nominal lengthscale of the bore, and U_s is the initial shoreline velocity. The nominal bore lengthscale δ is defined as the maximum swash depth at the mid-swash position, following Hughes (1995). We estimate f and U_s by simultaneously minimizing the root-mean-square error between the model and experimental x_s data. We treat f as a constant parameter across our three wave cases and U_s as a free parameter independent for each wave case. We find $f = 0.006$, which is reasonable compared to reported values for uprush in the literature (Conley et al., 2004; Puleo and Holland, 2001). We report the best fit values for U_s in Table 2.1. While this model treats the initial shoreline velocity as occurring instantaneously at $t = 0$, bore collapse is not an instantaneous process (Pujara et al., 2015). Thus, the modeled U_s values serve as estimates of the initial shoreline speeds. Despite this simplification, the model shows good agreement with our experimental shoreline positions for uprush, as shown in Figure 2.3, where experimental measurements match the characteristic parabolic shape of the swash.

Next, we further characterize the flow by plotting the shoreline velocity u_s which is defined as:

$$u_s = \frac{dx_s}{dt}. \tag{2.4}$$

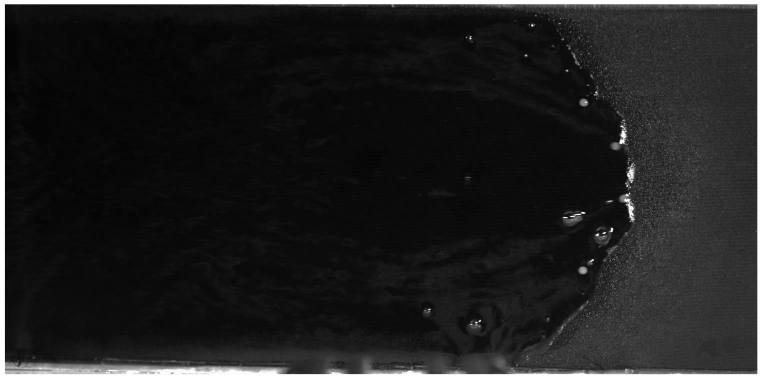

Figure 2.2: Example image of the experimental shoreline for the W2 wave case near the point of maximum run-up.

We measure the shoreline velocity using central differencing of x_s, again averaging over 20 experimental runs. We plot u_s against x_s in Figure 2.4 for the three wave cases. Each case is plotted such that the run-up lengths L all align on the x-axis. Plotted in this way, we see that the data all follow a similar trend. Note that we cannot measure the shoreline velocity near $x = 0$ because the wave is still collapsing near $x = 0$, making it difficult to identify a well-defined swash front.

In Figure 2.5, we plot the converged model solution of u_s as a function of x_s alongside the experimental data for each wave case. Note that the model comparison with our experimental data is for the uprush only. From these plots, we see that the model and experimental data have overall good agreement and show the bore velocity decelerating due to gravity and friction. For additional context, in Appendix B we compare our lab-scale flows to a larger, modeled field-scale swash event to show how the small, lab-scale flow can also approximately represent the uppermost portion of a large swash flow, which is the area closest to the wrack line.

Given that the shoreline kinematics in our experiments are well-described by the swash model, we use the same model framework to estimate the swash water depth.

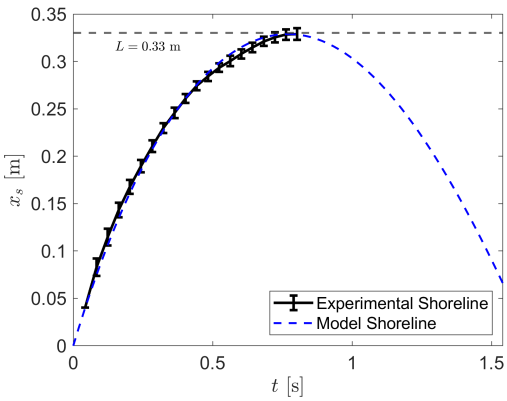

(a)

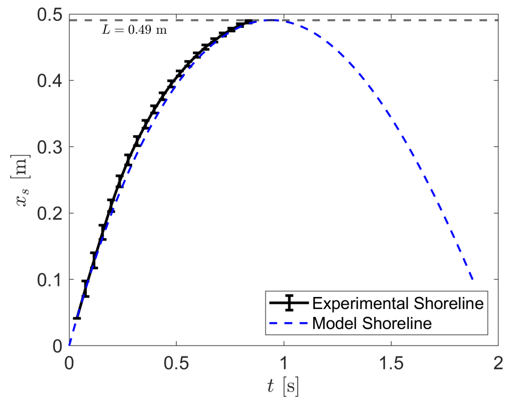

(b)

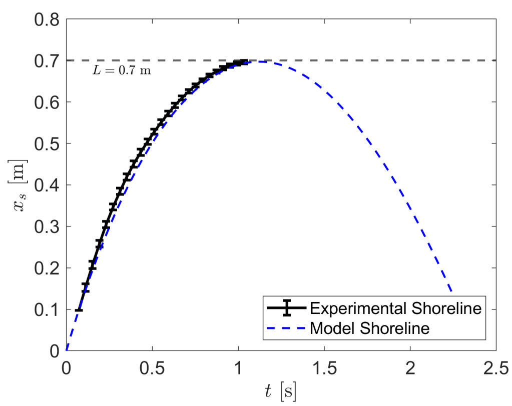

(c)

Figure 2.3: Experimental shoreline position (-) plotted as a function of time for wave case (a) W1, (b) W2, and (c) W3. Model shorelines (–) are plotted as a comparison. Maximum run-up L is represented by the dashed line. L values are approximately 0.33 m, 0.49 m, and 0.70 m, respectively.

Following Hughes and Baldock (2004), the water depth η is defined as:

$$\eta = \frac{U_s^2}{4g}\left(\frac{x_s - x}{x_s}\right)^C \left(\frac{T_s - t}{T_s}\right)^D, \tag{2.5}$$

where C and D are empirical coefficients; we use $C = 0.75$ and $D = 2$ based on

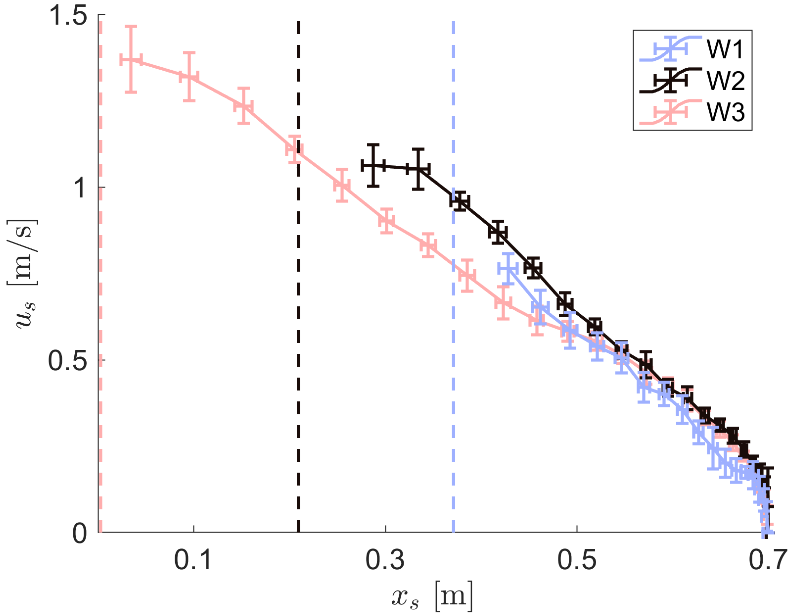

Figure 2.4: Uprush shoreline velocity u_s against position x_s for experimental swash. Each dataset is translated such that they have the same maximum run-up point. The vertical dashed lines represent the reference mean water line ($x = 0$) for each experimental wave case. Errorbars indicate the standard deviation.

Baldock and Holmes (1997), and T_s is the swash period. We approximated the swash period as twice the time it takes the bore to reach its maximum position (i.e., the run-up length L) which occurs at $t_{max} = B/A$. To compare the depth profiles across the different wave cases, we plot η at the time of maximum run-up t_{max} for $x = [0, L]$ in Figure 2.6. We also report the spatially average cross-shore water depth at t_{max} defined by $h^* = \frac{1}{L}\int_0^L \eta(x, t_{max})dx$ in Table 2.1. As expected, the water depth increases with run-up length. This highlights an important difference across our experiments: while the shoreline velocities are approximately self-similar across our wave cases, they show stronger differences with respect to their water depth. This follows from Equation 2.5 where η is proportional to U_s^2. Therefore, the major physical differences

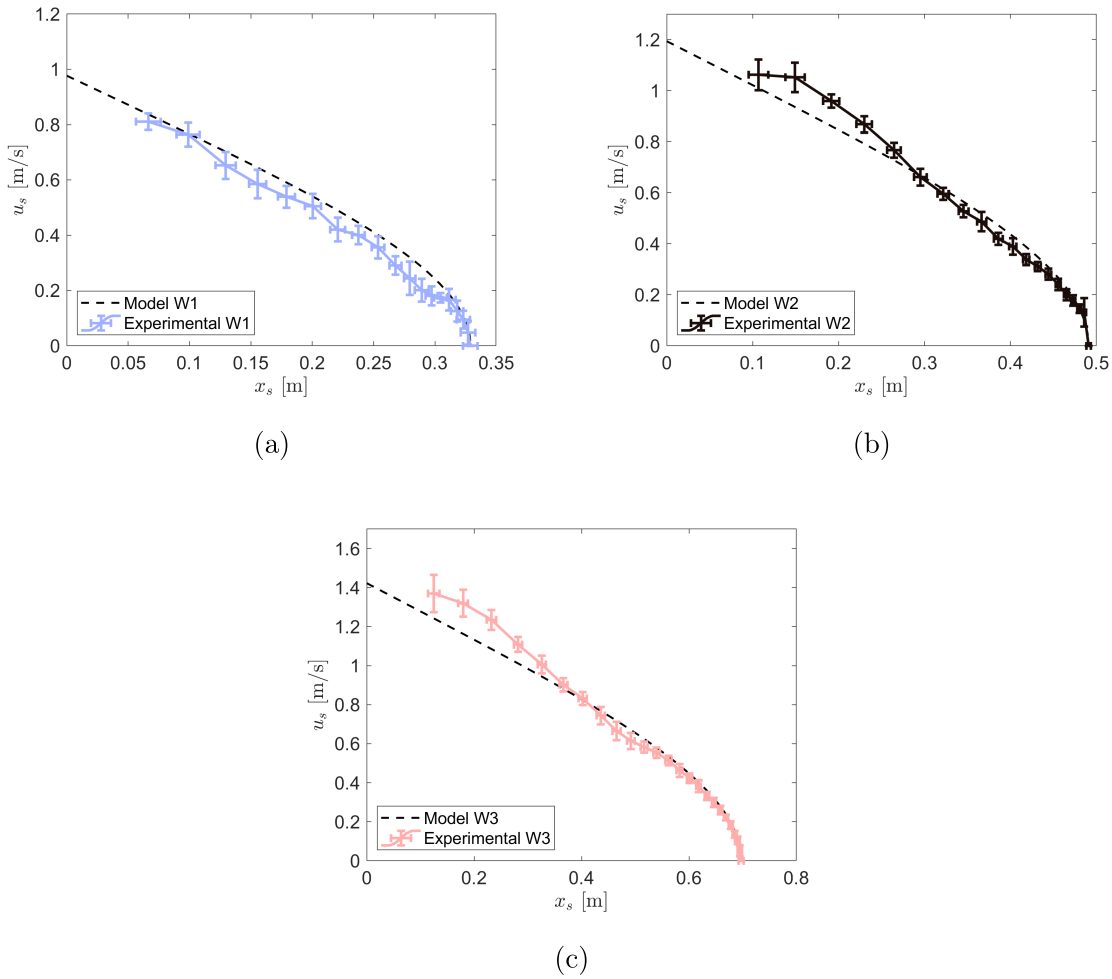

Figure 2.5: Model and experimental data comparison for shoreline velocity plotted against shoreline position. Separate plots show each wave case: (a) W1, (b) W2, and (c) W3. Errorbars indicate the standard deviation across 20 wave cases.

between our three wave cases in our study are their water depth and total run-up lengths L.

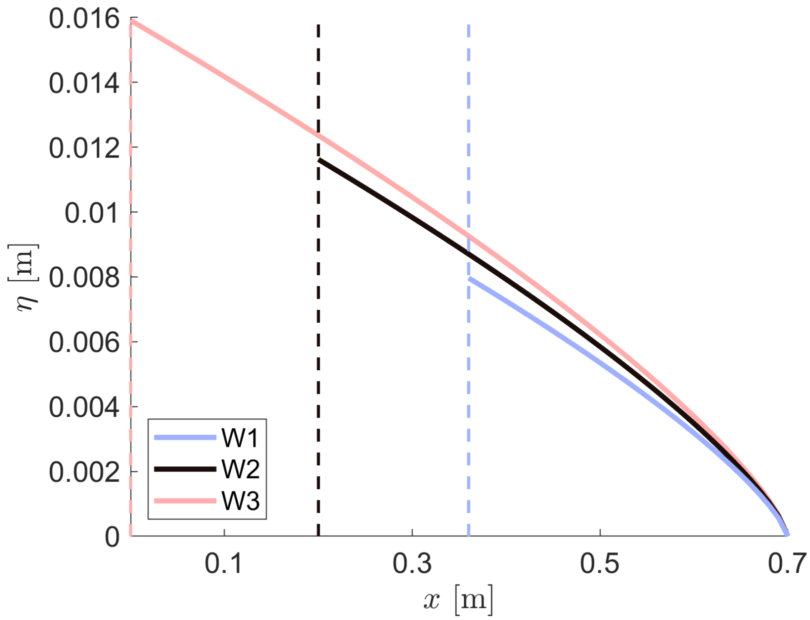

Figure 2.6: Modeled surface elevation η of the experimental swash flows plotted over $x = [0, L]$ at $t = t_{max}$. Following Figure 2.4, we align the plots such that their maximum run-up points overlap. The vertical dashed lines represent the reference mean water line ($x = 0$) for each experimental wave case.

Table 2.1: Wave parameters for the three wave cases considered. Data represents mean of N = 20 runs and error shows the standard deviation across N wave cases.

	W1	W2	W3
Run-up L (m)	$0.33 \pm .0062$	$0.49 \pm .0025$	$0.70 \pm .0046$
Initial shoreline speed U_s (m/s)	0.97	1.12	1.42
Swash period $T_s(s)$	$1.79 \pm .02$	$2.16 \pm .02$	$2.52 \pm .02$
Average water depth, $h^*(mm)$	4.5	6.6	9.1
Beach slope β	0.1	0.1	0.1

Table 2.2: Summary of experimental particle parameters.

	P1	P2	P3
Density ρ_p (kg/m^3)	970	970	970
Diameter d_p (mm)	5.0	7.0	10
Height h_p (mm)	0.79	0.79	0.79
Aspect Ratio λ	0.16	0.11	0.08

2.2.3 Particle experiments

We perform experiments to observe how buoyant particles are transported in our flow. We used positively-buoyant, disk-shaped particles with three different diameters ($d_p =$ 5,7, and 10 mm). The particles were die-cut from high-density polyethylene (HDPE) sheets with a constant height of $h_p = 0.79$ mm and density of $\rho_p = 970$ kg/m^3. The equilibrium floating draft of these particles is 7.7×10^{-4} m which is shallower than the depth across the majority of our swash flow. This means that the water is deep enough to suspend the particles. For reference, we summarize the properties of the particles, labeled P1, P2, and P3, in Table 2.2.

The experimental procedure is summarized as follows: we initialize particles on the beach above the mean water line; we generate a single swash event; and we track the particles until they either come to rest or leave the beach entirely. Due to the initially high speeds and light scattering off the leading edge of the swash front, we are unable to reliably track the particles when they are first impacted by the wave. However, because the particles are thin and the swash is shallowest at the front of the bore, the particles only have to rise a short distance to reach the surface. Thus, we observe the particles floating flat on the surface shortly after the initial pick-up where we are able to resume tracking them for the remainder of the swash event. For each experimental trial, we start four particles with the same initial cross-shore position

x_0, spread out in the alongshore direction. We vary x_0 over L for each wave case: three points for W2 and W3 but only one for W1 due to its short run-up length. For each experimental condition (unique initial position x_0, wave case, and particle size), we conducted 20 experimental trials for a total of 80 data points for each of the 21 unique combinations of parameters.

In Figure 2.7, we show an example of trajectories from multiple experimental trials (all corresponding to large particles P3 in each wave case) where we have plotted particle cross-shore position as a function of time. For reference, we also plot the experimental shoreline position. While all particles in each example share the same initial position, their overall transport varies. Some particles are transported in the backwash offshore, while others remain deposited on the beach. Notably, the resulting trajectories are smooth, indicating that the transport is primarily governed by the bulk flow with minimal turbulence.

We show another example of particle trajectories for an individual experimental run in Figure 2.8a in $x - y$ space, but this time in the smallest wave case. Again, we see the characteristic smooth ballistic motion. From the particle trajectories, we extract three key cross-shore points: particle initial position x_0, maximum position x_{max}, and final position x_f.

Additionally, here we again observe that there is some alongshore variability in our swash flow due to the effects of the side walls. To account for this, we define $L(y)$ which is the wave run-up length as a function of the alongshore coordinate y, shown by a schematic in Figure 2.8b. We measure $L(y)$ using the same overhead camera, and show how $L(y)$ evolves over time for each wave case in Figure 2.9. This demonstrates that the alongshore variability is most prominent at the maximum run-up. Therefore, we use $L(y)$ to normalize our data for particle maximum positions x_{max} to avoid any bias in the alongshore. However, we normalize all the final position x_f data by the maximum wave run-up L, as particle alongshore position can slightly shift over the course of their trajectory. Note that on average over the whole experiment, $L(y)$ and

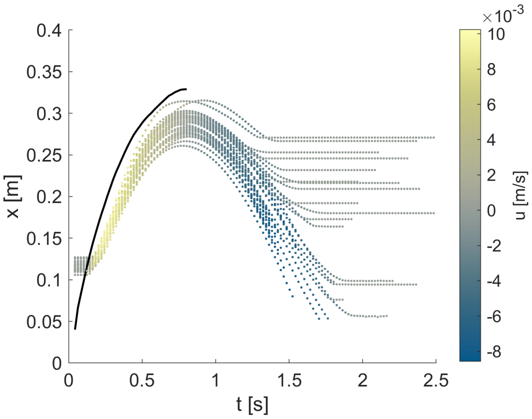

(a)

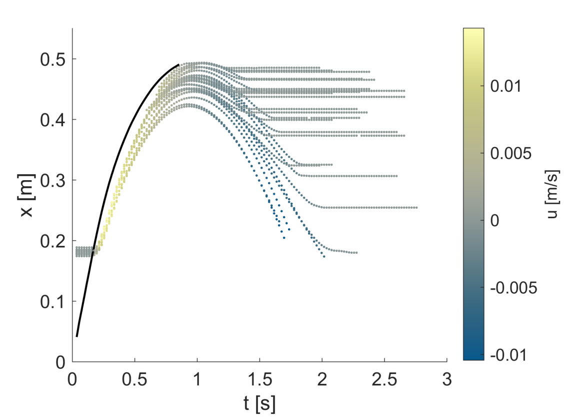

(b)

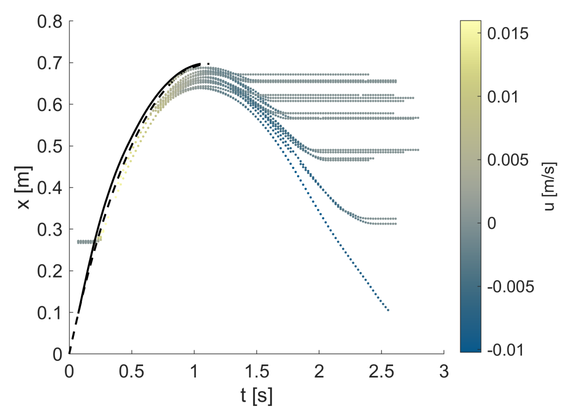

(c)

Figure 2.7: Examples of cross-shore particle trajectories as a function of time. These examples represent P3 particles in a (a) W1, (b) W2, and (c) W3 wave case. Experimental shoreline (-) is plotted as a function of time. Color bars represents local particle velocities u.

L have less than a 5% difference in our data, with the largest difference occurring at t_{max}.

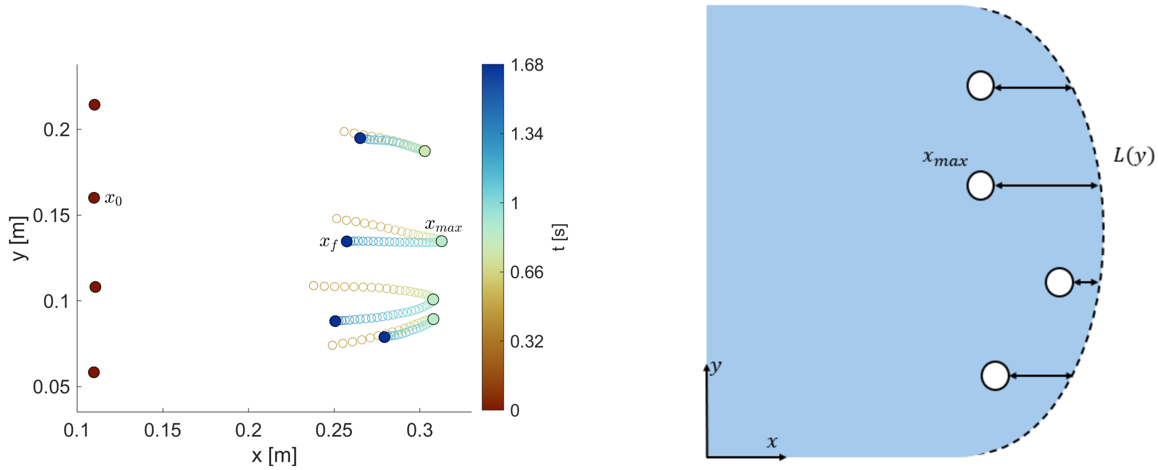

(a) (b)

Figure 2.8: (a) Example of experimental particle tracks with labels showing initial position x_0, maximum position x_{max}, and final position x_f. This is example considers P2 particles in a W1 wave case. Colorbar indicates the time during the experimental run. (b) Diagram showing alongshore variability at maximum run-up. Arrows indicate the distance between the maximum position x_{max} and the swash bore front.

2.2.4 Nondimensional parameters

In this section, we define the relevant nondimensional parameters governing the transport of particles in our experiment. First, we normalize the initial cross-shore positions x_0 by the maximum run-up length L. The resulting x_0/L values characterize the initial range of particle positions; the range is given in Table 2.3. Because the swash uprush is decelerating over time, particles starting at different cross-shore positions experience a different initial swash velocity. To account for this variability, we choose our characteristic velocity scale $u_{s,0}$ to be the instantaneous shoreline velocity at the moment the wave first impacts the particle ($x_s = x_0$). Defining a characteristic swash depth is not as straightforward because the swash depth is defined to be zero at x_s.

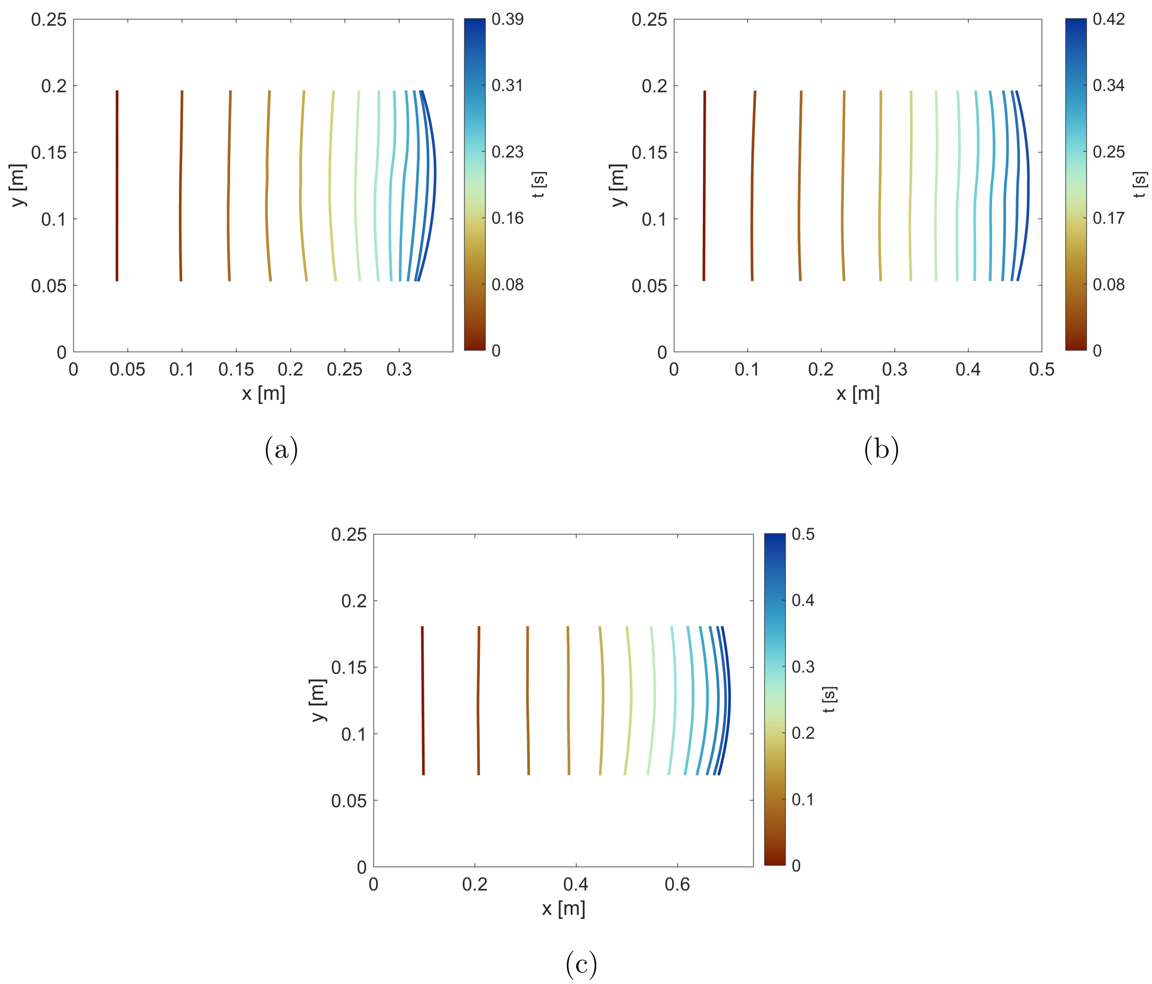

Figure 2.9: Alongshore variability of experimental shoreline as a function of time, for wave case (a) W1, (b) W2, and (c) W3. Data for each wave case is averaged over 20 experimental trials. Color bars indicate the time t during each wave case.

Thus, we choose the average swash depth at wave run-up denoted as h^*, as described in Section 2.2.2.

Following the framework of Davidson et al. (2023), we identify the Stokes number as the relevant nondimensional parameter to quantify the particle's relative inertia. The Stokes number is a ratio of the particle relaxation time τ_p to a characteristic fluid timescale. For consistency, we define these timescales in a similar manner as that of Davidson et al. (2023) which was derived by scaling the Maxey-Riley equation in a swash flow. First, we define the fluid timescale as $u_{s,0}/g$. This fluid timescale characterizes the deceleration of the flow due to gravity. We define τ_p at the point when the wave initially impacts the particle at x_0; this is a measure of how long the particle takes to accelerate from rest to the fluid velocity via drag. The particle is at rest when it is first impacted by the wave, so we define the slip velocity to be the fluid velocity $u_{s,0}$. The drag on the particle is a function of $Re_p = u_{s,0}d_p/\nu$, another important nondimensional parameter. Values of Re_p are moderately large ($\mathcal{O}(10^3 - 10^4)$), so we use the Schiller-Naumann drag model (Clift et al., 2005) to estimate the relaxation time τ_p as given by equation 2.6. This formulation is parameterized for the drag on a submerged sphere, but following Davidson et al. (2023), we use it to estimate τ_p for the disks in our experiments:

$$\tau_p = \frac{d_p^2(\rho_p/\rho_f + C_m)}{18\nu(1 + 0.15Re_p^{0.687})}, \tag{2.6}$$

where d_p is the particle's diameter and C_m is the added mass coefficient, which is set to 0.5. With these definitions, we define the Stokes number as $St_0 = \tau_p g/u_{s,0}$.

Finally, we consider secondary nondimensional parameters to quantify the relative importance of surface tension and relative depth. To assess surface tension, we define the Weber number $We = \rho_f d_p u_{s,0}^2/\gamma$ where γ is the surface tension of water. Next, we consider the relative height of particles to the average depth of the swash flow by defining the particle relative depth h_p/h^*. We report the ranges of all the discussed nondimensional numbers in Table 2.3, along with particle specific gravity ρ_p/ρ_f, which is held constant in these experiments. Because varying particle diameter and wave case simultaneously affects We, h_p/h^*, Re_p, and St_0, we cannot independently isolate the contributions of surface tension or relative depth from those of particle inertia in our experiments. However, we note that we are in the $We \gg 1$ regime across all trials, and therefore expect surface tension forces are likely small relative to inertia.

Table 2.3: Measured ranges for all non-dimensional parameters in the experiments.

Π group	Experimental range
ρ_p/ρ_f	0.97
Re_p	$3.01 \cdot 10^3 - 1.36 \cdot 10^4$
We	$25.2 - 257.2$
h_p/h^*	$0.11 - 0.28$
St_0	$0.22 - 2.12$

Additionally, we find that h_p/h^* is less than 1, and therefore our flow is deep enough for particles to float on the surface. Thus, we only focus on the effects of fluid and particle inertia via the Re_p and St_0 in our results discussion.

2.3 *Results* & *discussion*

2.3.1 Particle beaching

We first report particle convergence and beaching percentages in Table 2.4 as a function of particle size and wave case, with the data combined across all particle initial positions. We define the *convergence percentage* as the percentage of particle trajectories that intersect the uppermost region of the run-up (defined here to be the top 5% of L). This metric indicates how well the particles track the front of the swash bore and whether they approach the run-up line. However, it does not measure whether the particles beach at the point of maximum wave run-up, only that their maximum position approached it during uprush. In contrast, the *beaching percentage* represents the percentage of particles that remain on the beach after the wave has receded.

Across all scenarios, we see that the beaching percentages exceed the convergence percentages, indicating that the particles do not need to reach the uppermost part of the run-up to remain on the beach. In all three wave cases, we observe that the largest

Table 2.4: Measured convergence and beaching percentages for each experimental wave case and particle type. This data includes all initial positions.

Wave	Particle	Convergence %	Beaching %
W1	P1	93.8	98.8
	P2	56.3	93.8
	P3	3.8	36.3
W2	P1	92.9	100
	P2	77.9	98.8
	P3	52.9	72.9
W3	P1	86.3	99.2
	P2	77.5	97.1
	P3	72.5	89.6

particles have the lowest convergence and beaching percentages, whereas the smallest particles almost always beach no matter the wave case. This variation in beaching percentage as a function of particle size and wave case suggests that our study captures a regime where particle beaching is variable, i.e. where particle inertia is large enough to affect transport. Furthermore, it suggests low particle inertia increases beaching percentages, as the smallest particles had the highest beaching percentages while the largest particles in the smallest wave had the lowest beaching percentages.

To further explore the relationship between particle convergence and beaching, we plot the beaching percentage as a function of the average particle maximum position x_{max} normalized by the alongshore swash run-up $L(y)$ in Figure 2.10. Each data point represents the average for particles with the same initial position, particle size, and wave case. We find that the data generally collapses onto a single curve, and we see that large particles typically have the lowest $x_{max}/L(y)$ and beaching percentages, which matches what we report in Table 2.4. Overall, we observe that higher values of $x_{max}/L(y)$ correspond to higher beaching percentages. This trend aligns with physical intuition: particles that travel farther up the beach are more likely to remain there, as they are less susceptible to the backwash, which is initially weak near the top of the run-up (Zhang et al., 2008).

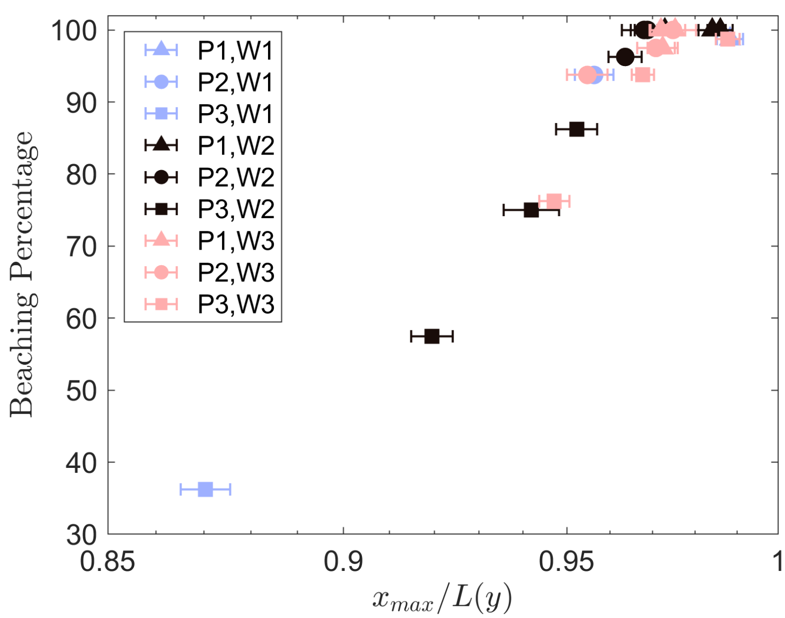

Figure 2.10: Beaching percentage as a function of $x_{max}/L(y)$. Data points represent the average x_{max} and beaching percentage ($N = 80$) given a set of initial conditions (x_0/L), wave case, and particle size. Errorbars indicate standard error.

2.3.2 Particle beaching locations

While beaching and convergence percentages gave us insight into the average transport of each particle in each wave case, we now consider the distribution of maximum positions and beaching positions for particles that beach in the experiments. To do this, we plot the distributions of $x_{max}/L(y)$ and x_f/L as a function of particle size and wave case in Figure 2.11, combining data across all initial positions. With respect to $x_{max}/L(y)$ (Figures 2.11a, c, and e), we see that the distribution is narrow around unity for the smallest particles. However, as particle size increases, the distribution of $x_{max}/L(y)$ spreads out and away from unity. This is consistent with the observed decrease in convergence percentages. Similarly with respect to x_f/L (Figures 2.11 b, d, and f), we see that the spread also increases with particle size. We also observe that the distributions are strongly skewed, with particles more likely to beach higher on the slope. Notably, only the largest particles exhibit significant beaching in the lower half of the run-up. These results show that while final beaching positions do vary, the smallest particles tend to reach higher maximum positions and higher final beaching positions.

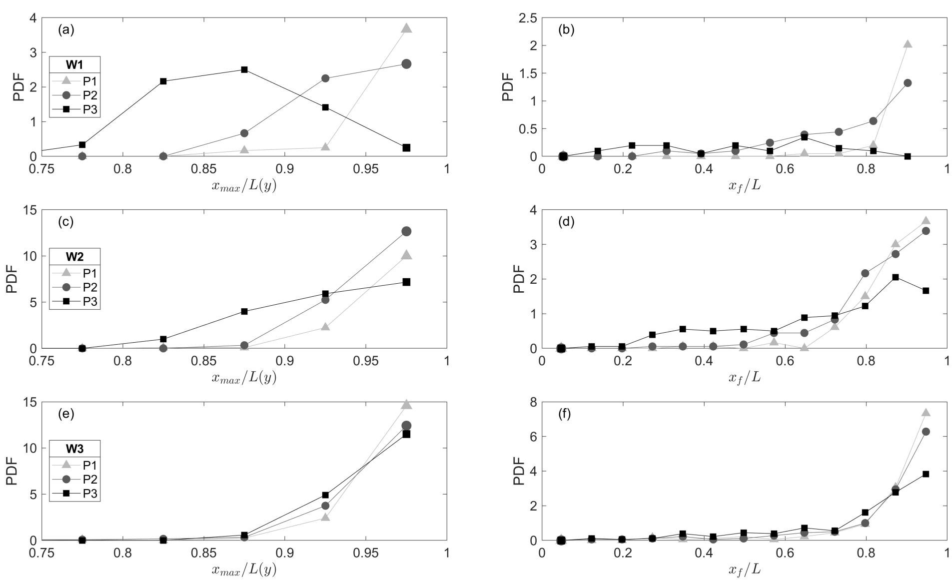

Figure 2.11: Probability distribution functions (PDF) of normalized particle maximum position $x_{max}/L(y)$ (a,c,e) and final position x_f/L (b,d,f) for each wave case and particle size. Each PDF includes data from all initial positions, only including data from particles that beach.

Next, we consider only the final locations of the particles that beach. Because we found a strong agreement between the average beaching percentage and $x_{max}/L(y)$, we suspect that $x_{max}/L(y)$ also controls the particle beaching location. Thus, we plot the normalized final particle positions x_f/L against $x_{max}/L(y)$ in Figure 2.12 in two different ways. First, we bin all of the data for each wave case, averaging across particle size in Figure 2.12a. We see that this binned data follows a similar trend regardless of wave condition: namely, that particles with larger $x_{max}/L(y)$ beach higher on the slope. This agrees with the beaching analysis in Figure 2.10. Because the swash velocities are approximately self-similar across the three wave cases, with the main differences being their maximum run-up length and water depth, we expect normalization by L to collapse the wave cases. Indeed, we find minimal variation between wave cases in Figure 2.12a, suggesting that relative depth is not a strong controlling factor in these experiments.

In contrast, we plot the same data again in Figure 2.12b, but now we average across all wave cases and separate the data by particle size. We find that in this case, although the data from each particle follows a similar trend, there is clear separation between the particle sizes. Notably, we see that the small particles end up beaching higher than the large particles with similar $x_{max}/L(y)$. Comparing Figure 2.12a with Figure 2.12b, we see that the differences in particle size are more important than the differences in the wave cases in determining particle transport across our experiments. This is consistent with the self-similarity of shoreline velocities across wave cases as previously noted. Overall, this suggests that as long as the water depth is deep enough to suspend the particles, the particle characteristics are most important to their transport, especially within the intermediate regimes considered in this study.

Regardless of how we bin the data, we see a clear relationship between $x_{max}/L(y)$ and x_f/L which makes physical sense. For example, the maximum position is an upperbound to the particle beaching locations. In addition, smaller $x_{max}/L(y)$ corresponds to particles being lower down on the beach at the time of flow reversal.

This will correspond to the particles experiencing deeper water and stronger initial backwash, allowing the flow to more easily carry the particles backwards on the slope before they beach.

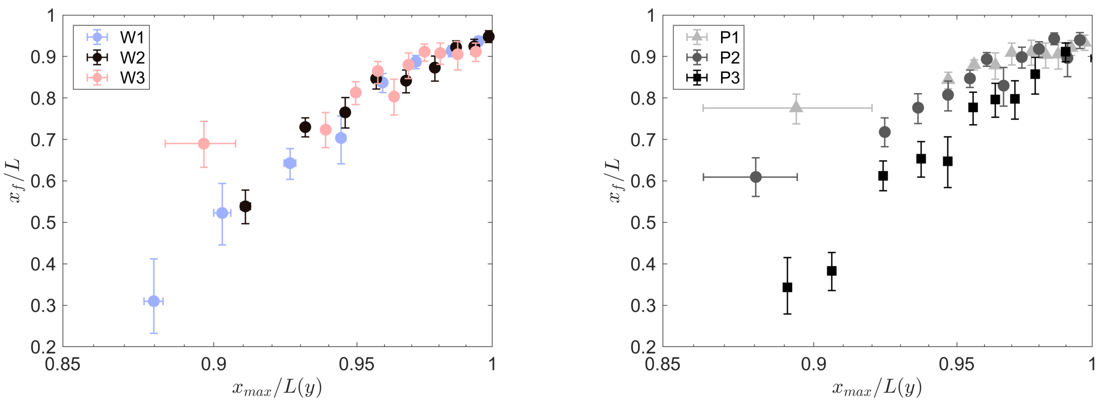

(a) (b)

Figure 2.12: Normalized particle final position x_f/L as a function of normalized maximum position $x_{max}/L(y)$. (a) Experimental data binned by wave case and (b) experimental data binned by particle size. Errorbars represent 95% confidence intervals determined via the bootstrap method.

2.3.3 Role of initial position

The swash bore's deceleration due to gravity and friction means that the strength of the initial wave-impact depends on the particle's starting location on the beach. This implies that the particle's initial location is critical to its transport in the flow. Therefore, as mentioned in Section 2.2.4, we define the shoreline velocity at the particle's initial position $u_{s,0}$ as an important velocity scale.

We first assess transport as a function of the particle Reynolds number Re_p. We plot Re_p defined at the moment of wave impact as a function of $x_{max}/L(y)$ and x_f/L

in Figure 2.13. Note that for a fixed particle size, $Re_p = u_{s,0}d_p/\nu$ varies only through $u_{s,0}$, so varying Re_p at constant d_p is equivalent to varying the initial position x_0 along the decelerating bore. While we observe no coherent trend for the entire data set, we see that for an individual particle size, lower Re_p corresponds to a lower $x_{max}/L(y)$ and x_f/L, most notably for the largest particles. Additionally, we see that for a constant Re_p, the larger particle size corresponds to lower $x_{max}/L(y)$ and x_f/L. These plots indicate that both Re_p and particle size are important to describe particle transport in these experiments.

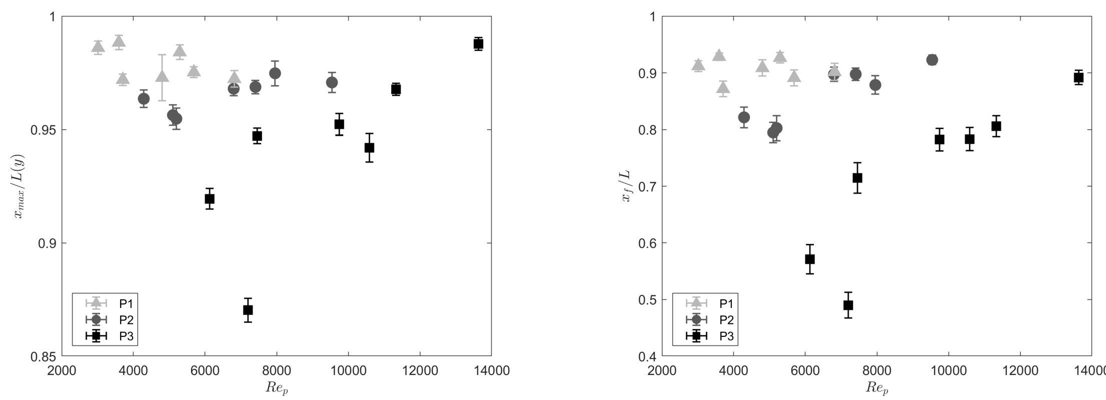

(a) (b)

Figure 2.13: (a) Average normalized maximum particle positions $x_{max}/L(y)$ plotted as a function of Re_p estimated at initial wave impact. (b) Normalized average particle final positions x_f/L as a function of Re_p. Each point represents the average values for each unique initial position, wave case, and particle size. The colors and shapes correspond to a specific particle size. Errorbars indicate standard error.

To synthesize the effects of both particle size and the fluid flow, we next assess the transport as a function of the particle Stokes number St_0 defined at x_0. This number is a measure of the particle's inertia relative to the flow and should relate to how long it takes the particle to accelerate to the swash flow's velocity. This implies that the larger the Stokes number, the more we expect the particles to lag the swash front. Thus, we plot the average $x_{max}/L(y)$ as a function of this St_0 in Figure 2.14a. Indeed, we see agreement that large St_0 corresponds to lower $x_{max}/L(y)$. Moreover, we see a collapse of the total data as compared to Figure 2.13a, suggesting that this St_0 alone captures the relevant dynamics of initial wave impact. While there is still scatter in the data, we observe a transition at $St_0 \approx 1$, where for $St_0 \lesssim 1$ we see $x_{max}/L(y)$ approach unity and for $St_0 \gtrsim 1$ we see $x_{max}/L(y)$ start to decrease. These results make sense given that lower inertia particles are more tracer-like and thus will follow the swash bore more closely, achieving higher maximum positions. In contrast, particles with higher St_0 will lag behind the swash bore initially and are therefore likely to remain further behind the bore front at the time of flow reversal.

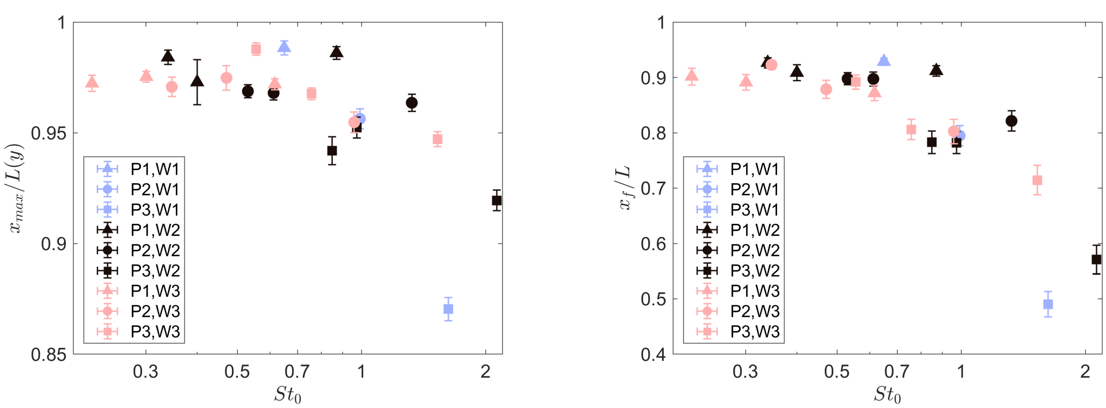

(a) (b)

Figure 2.14: (a) Average normalized maximum particle positions $x_{max}/L(y)$ plotted as a function of St_0 estimated at initial wave impact. (b) Normalized average particle final positions x_f/L as a function of St_0. Each point represents the average values for each unique initial position, wave case, and particle size. Errorbars indicate standard error.

Given that the particle maximum position $x_{max}/L(y)$ correlates with particle final position x_f/L (as in Figure 2.12), we also expect the final position to be correlated with St_0. Therefore, we plot the average x_f/L for each particle size, wave case, and initial position as a function of St_0 in Figure 2.14b. We see that the data also show a similar collapse, where we observe that particles with lower St_0 tend to beach higher on the slope with a transition at $St_0 \approx 1$. This result is somewhat counterintuitive when we compare it to the published results of Davidson et al. (2023). In their study, they found the opposite trend: namely, that particles with higher Stokes numbers were more likely to beach. However, this discrepancy can be clearly explained by the differences between their experimental setup and ours. In the experiments of Davidson et al. (2023), particles started in the water—not on the beach— and their Stokes number was therefore defined by the particles' initial condition as they entered the swash flow at the shoreline. This implies that the dynamics and parameters controlling particles entering the swash zone from offshore are not the same as particles which start on the beach and are impacted by an incoming wave. However, the results of both our study and that of Davidson et al. (2023) suggest that particle inertia and the initial condition are important parameters to the particle transport and beaching in swash flows and that there is not a single, governing Stokes number to describe the system. For example, we have shown that particle inertia is important to the pick-up process for particles on the beach, whereas the findings in Davidson et al. (2023) show particle inertia is also important to the transport once floating in the swash. Together with Davidson et al. (2023), we find that while the Stokes number is important to capturing particle transport trends, defining the relevant Stokes number is crucial during each regime of transport.

Our findings indicate that, within the regimes studied, particle inertia at initial wave impact is the primary control on net transport. Inertia governs how quickly a particle accelerates to the swash velocity, and this initial lag sets both its maximum and final positions. Thus, it is particle inertia together with the initial condition that is most important to particle transport in this flow. Finally, while this Stokes number formulation does collapse the data, there is still scatter in the collapse which is most notable in Figure 2.14a. This scatter is unsurprising for two reasons. The first concerns the assumptions made in calculating the Stokes number: e.g., the Schiller-Naumann drag model which assumes steady drag on a submerged sphere, whereas in our experiments the particles are flat disks in an unsteady shallow flow. Another assumption is that we neglect any potential friction or lubrication forces which may exist between the particle and the bed; these may also affect the particle's response to the wave at initial impact. However, despite these limitations, we argue that this Stokes number formulation does capture qualitative trends in the importance of inertia to this system, indicating its importance to the particle dynamics and the significance of the initial pick-up of the particle to its final beaching location.

2.4 Conclusions

In this study, we experimentally investigated buoyant particles in a model swash event. We focused on particles which initially started on a beach above the mean water line to study whether swash flows could remove them from the beach and under what conditions this might happen. By varying both particle size and wave conditions, we did indeed find that most particles remained onshore after a single swash event. For the particles on the beach, their final positions depended strongly on both their size and the strength of the wave impact. Smaller particles, which have lower inertia relative to the surrounding flow, tended to follow the uprush more closely, allowing them to reach higher maximum positions and avoid significant backwash transport. Conversely, particles with larger inertia lagged behind the swash front and tended to have lower final positions or be washed back offshore altogether. We find that the particle Reynolds number together with particle size can explain some of these trends. To combine the effects of both particle Reynolds number and particle size, we used the particle's Stokes number at the moment the incoming swash bore first contacts the particle. This Stokes number was found to inversely correlate with both the particles' maximum and final positions on the beach.

From a broader perspective, these results suggest that plastics stranded above the mean water line can still be picked up, moved around, and in some cases removed entirely from the beach by incoming waves. It also contrasts earlier work suggesting that higher Stokes number correlates with higher likelihood of beaching (Davidson et al., 2023) or that increasing particle buoyancy should increase the likelihood of particle beaching. Our results, which come from a different experimental setup from these previous studies, suggest that the beaching dynamics are more complex than can be captured by a single parameter, and that more work is needed to fully understand the system. We recommend future work to explore more of the complexity introduced by real plastics in real swash flows including interacting waves, diverse particle shapes, and sediment transport.

Chapter 3

STATISTICAL MODEL FOR THE CROSS-SHORE DISTRIBUTION AND REMOVAL OF BEACHED BUOYANT MICROPLASTICS IN THE SWASH ZONE

This work is Co-Authored by Michelle DiBenedetto, Melissa Moulton, and Chris Chickadel. Michelle DiBenedetto helped with model suggestions, data analysis, and manuscript drafting. Melissa Moulton helped with result suggestions and manuscript drafting. Chris Chickadel assisted with model development, focusing on statistical analysis.

3.1 Motivation

Beaches serve an important role in microplastic transport, acting as both a source and a sink. Therefore, understanding and predicting how these microplastics can be transported along beaches is crucial for combating the issue of widespread microplastic pollution. To model transport on beaches, there is a necessity to develop physics-informed parameterizations for beaching probabilities that consider varying combinations of particle and wave characteristics.

Some previous studies have developed physics-based models to understand the beaching of buoyant microplastics. For instance, Larsen et al. (2023) identified the particle Dean number, which characterizes particle buoyancy, as an important non-dimensional parameter; specifically, particles with a lower Dean number, or higher rise velocity, tend to beach more quickly. Additionally, Davidson et al. (2023) finds that Stokes number influences particle beaching, with higher Stokes numbers leading to higher beaching positions. However, these studies only consider particles that start in the water, while previous studies have shown that the effects of key non-dimensional parameters can differ for particles that start in the water compared to those starting on the beach (Abarca et al., 2026; Davidson et al., 2023).

Therefore, we develop a statistical model to study buoyant particle transport in the swash zone. We focus on studying how particles that start on a beach are transported up and down the beach slope by continuous swash events, or run-ups, using beaching probabilities. Beaching probabilities refer to the likelihood that a particle remains on the beach after a run-up event. If a particle does remain on the beach, its position relative to the run-up height is predicted using a statistical model. Our model is informed by experimental observations by Abarca et al. (2026) which parameterize beaching probabilities and distributions of beaching positions as a function of Stokes number, itself a function of particle properties and position as well as flow characteristics. We conducted these experiments in a wave tank to observe small-scale particle-swash interactions for a single swash event, mimicking small run-ups on low-energy beaches. In the following sections, we outline our model structure and inputs, highlight model outputs, and discuss model sensitivity to variations in key parameters.

3.2 Statistical model

3.2.1 Overview of model approach

The model framework simulates the cross-shore transport (in the x-direction) of a group of buoyant particles that start at rest on an impermeable beach with uniform slope β (Figure 3.1) subject to a sequence of wave run-ups. Particles are simulated according to their beaching probability and distribution of final positions, both of which are informed by laboratory experiments and based on particle characteristics and the swash bore velocity at the initial particle location. Particles are initialized on the beach at positions x_p. Each model timestep corresponds to an individual run-up of cross-shore length L randomly sampled from a Rayleigh distribution, a commonly used model to represent wave run-ups on a beach (Battjes, 1971; Nielsen et al., 1991); we describe the distribution in more detail in Section 3.2.2. In our model, particles are exclusively transported along the beach by individual waves, i.e., we do not consider effects of wind, swash-swash interactions, or particle-particle interactions. Finally, in order to isolate the transport of buoyant particles due to swash forcing, this model only studies particles which start on a beach. We do not consider any input of particles from offshore to the beach as this would necessitate consideration of surf zone dynamics; thus, once particles leave the beach, they do not return.

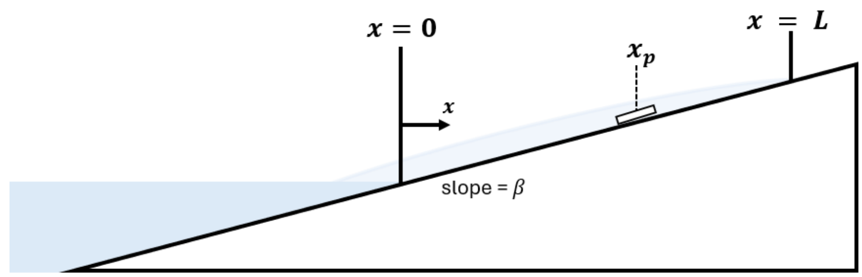

Figure 3.1: Schematic of dimensions used in the model. The x coordinate is the cross-shore position on the beach relative to the location of the mean water line. x_p represents the particle position along the beach.

We summarize the model framework and the process of updating particle positions in a flow chart in Figure 3.2. For each timestep, we first determine whether each particle on the beach is hit by the wave. If the particle is too high on the beach, ($x_p > L$), the particle's position remains the same for the next timestep. If the particle is hit by the wave ($x_p < L$), we derive a Stokes number to define the relative inertia of the particle on the beach when it is hit by the wave. The Stokes number is the input to a set of parameterizations that determine the particle's probability of remaining on the beach, and, for particles that do remain on the beach, the probability distribution of their beached position following the run-up. Physically, this is motivated by our experimental observations that particle Stokes number determines an initial lag during particle pick-up, where lower Stokes numbers refer to particles responding more quickly to the flow, while larger Stokes numbers refer to particles which have a longer response time to the flow's acceleration (Abarca et al., 2026). This lag determines how far the particles travel up with the run-up and whether they are likely to wash off the beach.

Using the Stokes number, we first probabilistically determine whether the particle remains on the beach or not with a beaching probability model described in Section 3.2.3. If a particle remains on the beach, we next update its position on the beach, where updated positions are sampled randomly from a physics-informed distribution derived from observations, also described in Section 3.2.3. If the particle does not remain on the beach, it is considered to be offshore of the mean water line ($x_p < 0$) and is not simulated in future timesteps. During the simulation, we compute the percentage of particles that remain on the beach, and we track the evolution of the beached particle positions. We define a residence time τ_r based on the e-folding timescale of the remaining fraction of beached particles.

3.2.2 Wave run-up distribution

Nielsen et al. (1991) show that a Rayleigh distribution can be used to describe the range of run-up elevations L_z on a beach, where run-up elevations are the maximum vertical excursions of run-ups. To define the distribution, we start with initial inputs of significant wave height H_s, wave period T, and beach slope β. In this model, we use a constant wave period T to simplify complexities of a real beach and focus on the impact of significant wave height H_s. Following Mørk et al. (2026) and using equations from Bosboom et al. (2023), we use these inputs to calculate a H_{rms} and

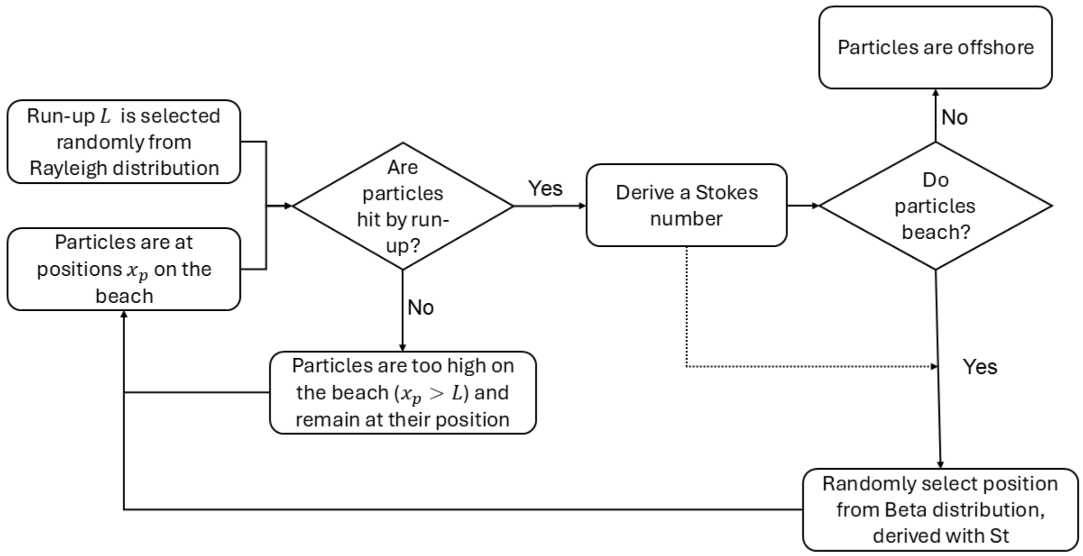

Figure 3.2: Flow chart describing the process of updating particle positions.

λ, such that:

$$H_{rms} = \frac{1}{\sqrt{2}} H_s, \tag{3.1}$$

$$\lambda = \frac{gT^2}{2\pi}, \tag{3.2}$$

where H_{rms} is the root-mean-square deep water wave height and λ is the deep water wavelength.

Nielsen et al. (1991) show that H_{rms}, λ, and β can be used to define $L_{z,rms}$, the root-mean-square value of run-up elevations L_z. Values of $L_{z,rms}$ are defined as:

$$L_{z,rms} = \begin{cases} 0.6\beta\sqrt{H_{rms}\lambda} & \beta \gtrsim 0.1 \\ 0.05\sqrt{H_{rms}\lambda} & \beta \lesssim 0.1. \end{cases} \tag{3.3}$$

Next, we define the shape parameter of the Rayleigh distribution σ, which is equal to $\frac{1}{\sqrt{2}} L_{z,rms}$ (Nielsen et al., 1991). Finally, the Rayleigh distribution has a probability density function of:

$$f(L_z|\sigma) = \frac{L_z}{\sigma^2} e^{-\frac{(L_z)^2}{2\sigma^2}}. \tag{3.4}$$

Note that this formulation is for run-up elevations L_z. However, our simulations require run-up cross-shore length L. To achieve this, we assume a uniformly sloped beach and divide L_z distributions by beach slope, i.e., $L = L_z/\beta$ and $L_{rms} = L_{z,rms}/\beta$, where L is the horizontal run-up length and L_{rms} is the root-mean-square value of the horizontal run-up lengths.

Following this formulation, we generate example wave run-up distributions for different input wave parameters and plot them in Figure 3.3. In these distributions, we use a constant beach slope of $\beta = 0.11$ and constant wave period of $T = 6$ s, while varying the significant wave height H_s. Differences in the run-up distributions are therefore due to differences in H_s which results in varying L_{rms}; specifically, higher H_s leads to higher L_{rms} for a constant $beta$ and T. Overall, the L_{rms} values plotted here are between $1-2$ m. Thus, small run-ups (< 1m) are common in our simulations; this is consistent with the experimental data the model is based on. However, large run-ups (e.g., > 5m) are still possible but less common.

3.2.3 Empirically-derived inputs

Here, we describe the model inputs based on our previous experiments which found that the particle's relative inertia in the swash wave largely controlled its net transport and beaching probability (Abarca et al., 2026). In the experiments, small disk-shaped buoyant plastic particles (< 10 mm) were initialized on a beach, then particle positions were tracked during a single run-up event. We found that the Stokes number defined at run-up impact on the particle was an important parameter for predicting particle transport and beaching. The Stokes number St is the ratio of a particle's inertia to that of the surrounding fluid, i.e., it represents how quickly a particle responds to the surrounding flow. We solve for this Stokes number as defined in Abarca et al. (2026),

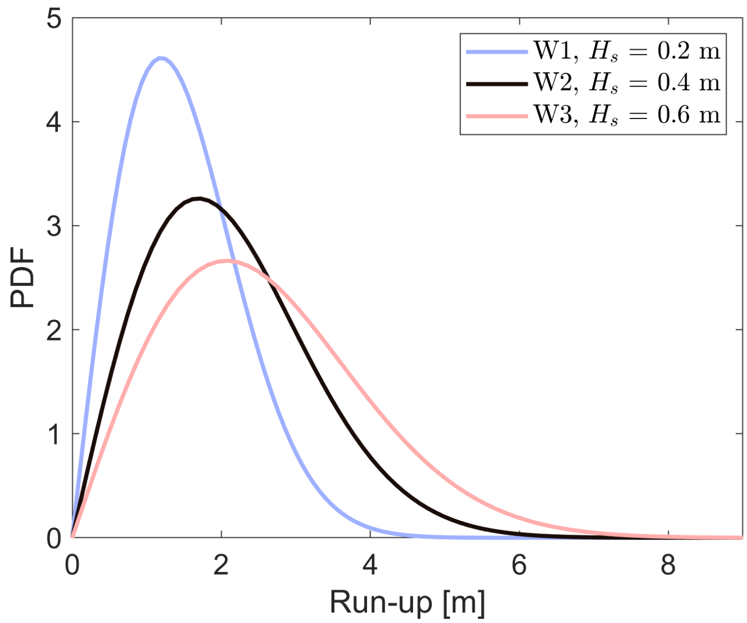

Figure 3.3: Wave run-up distributions used to select random run-ups in the present model. Each line is a PDF generated using a Rayleigh distribution. For a constant slope β and wave period T, the wave distributions vary via their significant wave height H_s.

such that $St = \tau_p/\tau_f$ where τ_p is the particle relaxation time given by:

$$\tau_p = \frac{d_p^2(\rho_p/\rho_f)}{18\nu(1 + 0.15Re_p^{0.687})}, \tag{3.5}$$

using particle diameter d_p and particle Reynolds number Re_p. The fluid timescale τ_f is derived using the shoreline velocity at the particle's location $u_s(x_p)$, where $\tau_f = u_s/g$. The particle Reynolds number is also defined with this velocity: $Re_p = u_s d_p/\nu$ where ν is the fluid kinematic viscosity. The shoreline velocity is the speed of the swash bore front, so τ_f characterizes the time it take for the flow to fully decelerate due to gravity. We derive the shoreline velocity using a swash model (Hughes and Baldock,

2004) with the following equations:

$$x_s = \frac{2\delta}{f} \ln\left(\frac{\cos(At + B)}{\cos(B)}\right), \tag{3.6}$$

$$u_s = \frac{dx_s}{dt}, \tag{3.7}$$

and

$$L = \frac{-2\delta}{f} \ln(\cos(B)), \tag{3.8}$$

where

$$A = -\sqrt{\frac{gf\sin(\beta)}{2\delta}}, \qquad B = \tan^{-1}\left(\frac{U_s\sqrt{f}}{\sqrt{2g\delta\sin(\beta)}}\right). \tag{3.9}$$

Here, x_s is the cross-shore shoreline position, f is the friction factor set at 0.007 based on the averages from Puleo and Holland (2001), and δ is the nominal lengthscale of the bore, which is defined as the maximum swash depth at the mid-swash position (Hughes, 1995). Using this shoreline (i.e., run-up) velocity, we define the St. From the experiments, we find that generally low St leads to higher particle beaching percentages and high beaching positions, compared to particles with an intermediate and high St.

Beaching probability

Mørk et al. (2026) used a beaching probability (here p_{beach}) to represent the likelihood that a particle hit by a wave remains on the beach. In their simulations, they used p_{beach} as a free parameter as they were unable to successfully parameterize it given the lack of available data. However, they did acknowledge it should depend jointly on both the particle and swash properties. Here, we attempt to address this gap by developing a physics and data-informed parameterization of the beaching probability. We define beaching probability p_{beach} as a function of Stokes number, informed by our laboratory experiments which cover the range $St = [0.22 - 9.23]$. The beaching probability for each St value is found by measuring the remaining number of particles on the beach after a wave run-up, normalized by the total number of particles initially on the beach ($n = 80$ for each data point). In Figure 3.4, we plot p_{beach} as a function of St. In this plot, we clearly see that there are three regimes, where there is a transition occurring around unity at $St \approx 1$, and a second transition occurring at $St \approx 2$. In the regime of $St \leq 1$, particles follow the run-up closely due to minimal lag at wave impact leading to high positions on the beach, resulting in a greater chance of particles remaining on the beach. This regime corresponds to small particles in faster initial shoreline speeds, i.e., starting lower on the beach where flow speeds are the fastest during uprush. In contrast, particles that are initially higher on the beach typically fall into the $1 < St \leq 2$ regime, and are more likely to wash off the beach. This behavior is due to the high St particles having a larger initial lag when picked up by the wave. This causes the particles to trail behind the swash front during uprush, thus allowing the backwash to more easily wash the particles off the beach (Abarca et al., 2026). While the regime of $1 < St \leq 2$ comprises of high inertia particles that lag significantly behind the swash front, there is a limit for how high a particle's inertia can be while still being transported by the run-up. For instance, a particle with a large τ_p can lag long enough behind the shoreline such that the shoreline can recede past the particle before mobilizing it. Because a swash event can be modeled as a ballistic process (Shen et al., 1963), τ_p would need to be roughly twice τ_f for the shoreline to fully recede past the particle before it can react to flow. Therefore, the third regime is defined for $St > 2$. Within the particle size regime studied (< 10 mm), these high St values occur near the point of run-up L, where flow velocities are close to zero. Moreover, flow depth at L is very shallow, and thus typically not deep enough to lift particles from the bed with buoyancy.

In Figure 3.4, we plot a fitted line to these St regimes, where p_{beach} is a constant for both regimes of $St \leq 1$ and $St > 2$, and p_{beach}decreases linearly with increasing $1 < St \leq 2$. We see that there is relatively high uncertainty associated with the data and the fitted line for our p_{beach} formulation, especially for $1 < St \leq 2$. Consistent with other studies, defining p_{beach} is still a challenge. However, we note that as more data becomes available, this parameterization can be updated. Additionally, we conduct a sensitivity analysis on p_{beach} to test the parameterization's importance in our simulations in Appendix C. In summary, the three different regimes for beaching probability p_{beach} are defined as a function of St, such that:

$$p_{beach} = \begin{cases} 0.99 & St \leq 1 \\ -0.41(St) + 1.35 & 1 < St \leq 2 \\ 0.95 & St > 2. \end{cases} \tag{3.10}$$

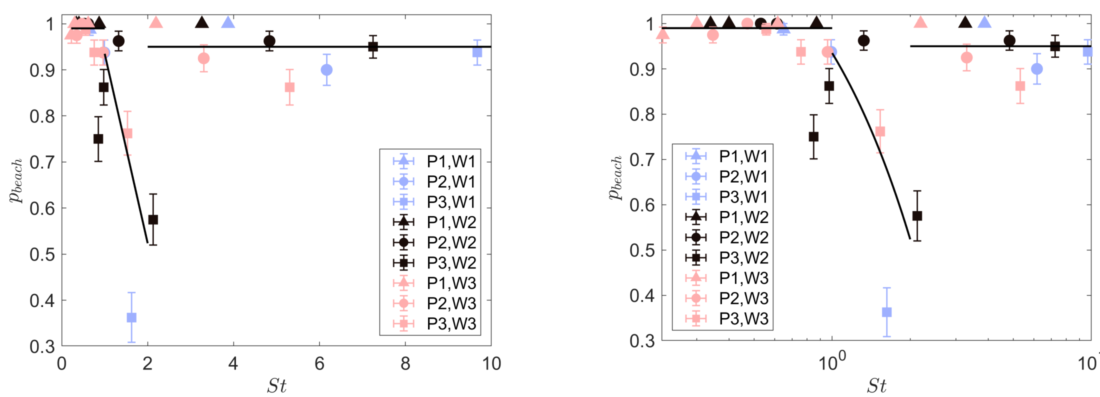

(a) (b)

Figure 3.4: Experimental and modeled beaching probabilities as a function of Stokes number, plotted with a (a) linear and (b) logarithmic x axis. Legend entries indicate experimental data. Modeled probabilities from Equation 3.10 (-).

Beached particle positions

In addition to beaching probabilities, distributions for the new particle positions on the beach after each wave are also derived from our experimental results. For particles that remain on the beach in our model, we use St to determine their updated positions.

We first define the distribution of particles for a single St from our experiments, then fit a probability density function of a Beta distribution B to our particle position data for each Stokes number.

The Beta distribution is a natural choice for this model because particle positions are bound between the mean water line ($x = 0$) and the wave run-up ($x = L$), and the Beta distribution is bound between $[0, 1]$. Thus, we normalize positions by L to map directly to the Beta distribution. It is also flexible enough to capture the regimes we observed in our experiments: low-St particles, which have low inertia, respond quickly to the flow and beach near the wave run-up with a narrow distribution, and high-St particles, which lag the swash bore, are thus more likely to beach with lower positions relative to the run-up with a broader distribution of positions across the beach. Finally, the Beta distribution has also been shown to match particle distributions in single wave experiments (Mørk et al., 2026). Its probability density function (PDF) is given as:

$$f(x_p|a, b) = \frac{\Gamma(a+b)}{\Gamma(a)\Gamma(b)} x_p^{a-1}(1-x_p)^{b-1}, \tag{3.11}$$

where Γ represents the Gamma function, and a and b are shape parameters. We fit the PDFs to our experimental data in order to estimate a and b and how they vary with Stokes number. We obtain the following parameterization:

$$a = 0.58(St)^2 - 1.53(St) + 3.41, \tag{3.12}$$

$$b = 0.56(St) + 0.17. \tag{3.13}$$

Using these parameterizations, we build Beta distributions for varying Stokes numbers as shown in Figure 3.5. As expected, the distribution for low-St favors particles ending up high on the beach, while the distributions for $1 < St \leq 2$ are more spread across more of the beach. For $St > 2$, distributions begin to favor high final positions, although not as strongly as low-St which is similar to lower p_{beach} in this regime compared to $St < 1$. We also plot the means of the Beta distributions given by $\overline{B} = a/(a + b)$ alongside the means from our experimental data in Figure 3.6. Again, this confirms that the Beta distribution is a suitable model for our particle position data. Finally, we highlight that these distributions are derived from a limited data set, but they are a good starting point as they capture the range of responses we expect due to particle inertia in the swash.

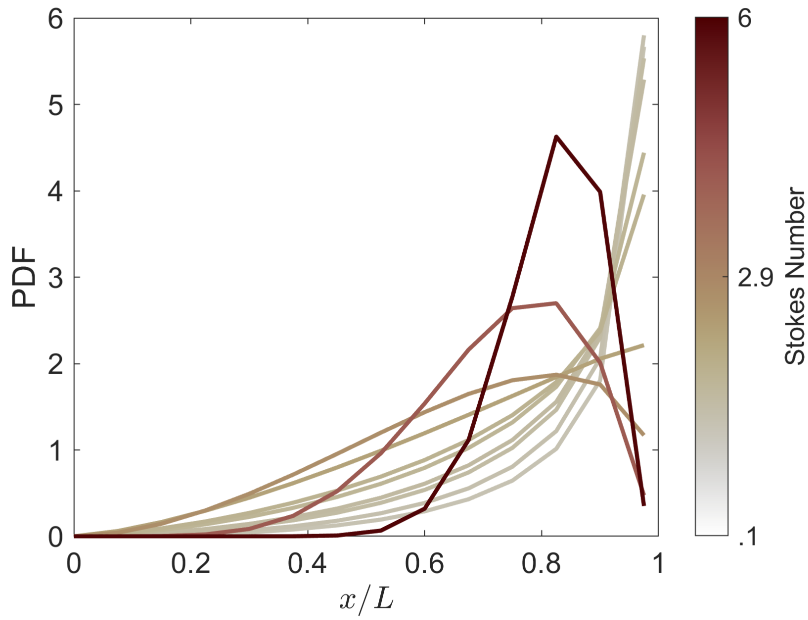

Figure 3.5: Beta distributions that are used to estimate where particles beach in our model. Beta distributions are derived from fitting to the experimental particle position data.

3.2.4 Statistical model description

The model takes a constant beach slope input β and wave inputs of T and H_s, from which we derive L_{rms} (Equation 3.3). Additionally, we specify the number of wave run-ups N_w over which we simulate, the initial number of particles on the beach N_p^0, and the particle properties: diameter d_p, height h_p, and density ρ_p, as in the experiments with disk-shaped particles the model is based on (Abarca et al., 2026).

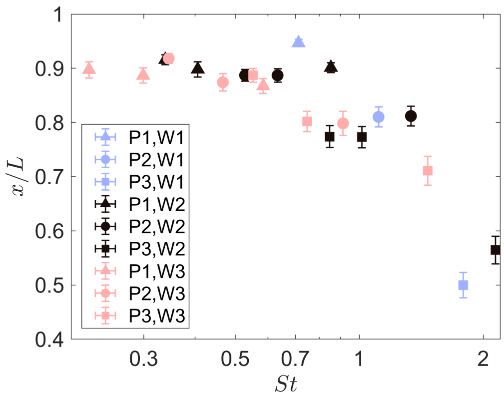

(a)

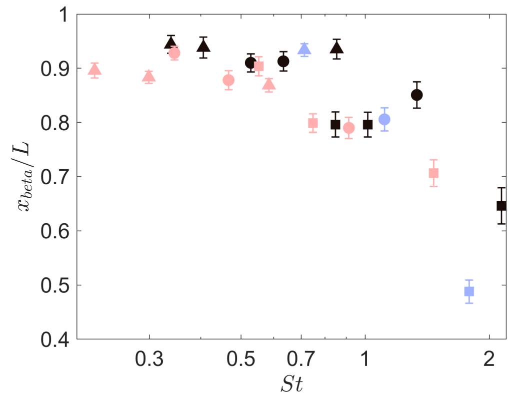

(b)

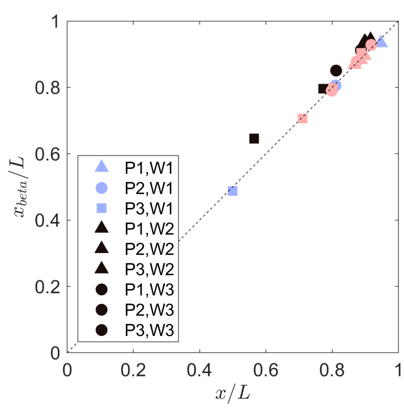

(c)

Figure 3.6: Experiment and simulation comparison. (a) Experimental results of normalized mean position as a function of Stokes number. (b) Model results of the normalized final position as a function of Stokes number. (c) Normalized final positions from both experimental and model results. Each point represents a unique combination of initial conditions as listed in the legend. Errorbars are the standard error.

Before the initial time-step at $t = 0$, N_p^0 particles are evenly distributed across the beach in the region between the MWL ($x = 0$) and $x = L_{rms}$.

At each timestep $n = t/T$, a run-up length L^n is randomly selected from the Rayleigh distribution defined in Section 3.2.2. For each particle on the beach with $x_p^n < L^n$, the particle is impacted by the wave and its Stokes number St_p^n is computed from its current position x_p^n and the shoreline velocity $u_{s,p}^n$ at the moment the run-up reaches the particle, as described in Section 3.2.3. Using St_p^n and Equation 3.10, we compute p_{beach} and then use this probability to predict whether the particle remains on the beach. If the particle does remain, its updated position is randomly sampled from the Beta distribution defined by Equations 3.12 and 3.13. If the particle does not remain, it is considered to have left the beach ($x_p < 0$) and is removed from all future timesteps. The position updating procedure can be summarized as:

$$x_p^{n+1} = \begin{cases} \sim \text{Beta}(a(St_p^n), b(St_p^n)) \cdot L^n & \text{with probability } p_{beach}(St_p^n) \\ \text{offshore; } (x_p < 0) & \text{with probability } 1 - p_{beach}(St_p^n) \end{cases} \tag{3.14}$$

further illustrated in Figure 3.7. If $x_p^n > L^n$, then the wave does not reach the particle, and the particle's position remains unchanged ($x_p^{n+1} = x_p^n$). Particles with $x_p^n \gg L_{rms}$ may go several timesteps without updates to their positions; these dynamics are associated with more extreme run-up events that occur infrequently.

During each simulation, we track the cross-shore positions of all beached particles and the fraction remaining on the beach over time. From these data, we define a residence time τ_r as the e-folding timescale of the beached particle fraction over time. To calculate τ_r, we fit the equation $N_p(t) = N_p^0 \exp(-t/\tau_r)$ where N_p is the number of particles on the beach at any given timestep. In the following sections, we use the model to study how variations in wave height and particle properties affect particle residence times τ_r and particle distributions on the beach over time.

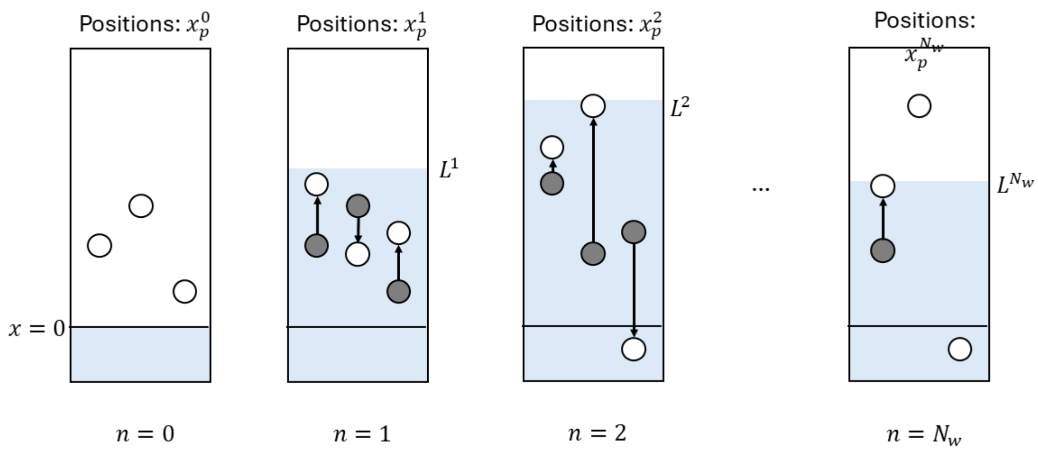

Figure 3.7: Schematic structure of the model as a function of n. Particle positions are updated during each timestep using the particle Stokes number, which is a function of particle position, wave run-up, and shoreline speed. Gray circles indicate the particle positions in the previous time step, while white circles represent positions in the current time step.

3.3 *Results* & *discussion*

3.3.1 Evolution of cross-shore particle distributions in continuous run-ups

We present results from a baseline simulation to illustrate the model outputs and general behavior we observe for beached particles under continuous wave forcing. We use a uniform beach slope $\beta = 0.11$, consistent with our previous experiments (Abarca et al., 2026), a constant wave period $T = 6$s chosen to represent a short-period swell (Bosboom et al., 2023), and a significant wave height $H_s = 0.2$m, chosen to represent lower energy run-ups that might be observed on protected beaches. Together, these result in a run-up distribution defined by $L_{rms} = 1.19$ m. We are interested in studying these relatively small to intermediate wave run-ups because they are especially important to the transport of buoyant microplastics. For example, while large, energetic waves are needed to suspend and transport negatively-buoyant sediment, waves of any size can transport buoyant particles, and thus studying beaches with relatively small waves can become increasingly important. We simulate disk-shaped particles consistent with our laboratory experiments with diameter $d_p = 0.005$ m, height $h_p = 0.00079$ m, and density $\rho_p = 970$. We first initialize $N_p^0 = 1000$ particles uniformly from $x = 0$ to $x = L_{rms}$ and simulate $N_w = 100$ waves.

In Figure 3.8a, we plot a heatmap of the resulting particle cross-shore locations over time for a single simulation. The colorbar indicates particle count density normalized by the initial number of particles, and the median particle position is plotted with a black-dotted line. Additionally, a line representing the mean water line (MWL) is plotted at $x = 0$; below this line, we keep track of particles that have left the beach. From this plot, we observe how the beached particle distribution changes over time. Particles initially rapidly move up the beach before slowly continuing to move up over time. This upward transport is intermittent: as the particles move up the beach, an increasingly smaller fraction of waves in the distribution will be large enough to reach the highest particles. Thus, the transport up the beach slows over time. This is further illustrated by Figure 3.8b, which plots the median particle positions on top of the wave run-ups over time. The median particle position is only able to advance when there is a sufficiently large run-up, generating discrete jumps in its evolution. Additionally, we clearly observe the highest density of particles at the top of the beach; this is similar to the 'wrack line' which forms on a real beach.

Over the course of the simulation, we also see particle count density offshore increasing over time. This indicates that particles are continuously leaving the beach. Even when wave run-ups do not reach the median positions (e.g., after $t/T = 20$ or 70 as seen in Figure 3.8b), particle count density below the MWL is still increasing.

This indicates that particles lower on the beach are still able to be washed off by smaller run-ups. Thus, even though the particles at the top of the beach may become relatively stationary, particles lower on the beach will be continuously transported.

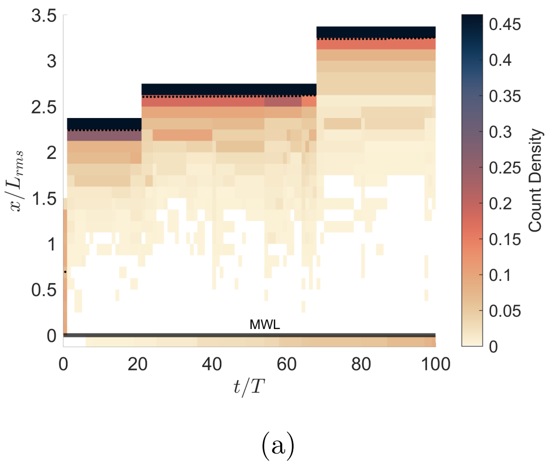

Figure 3.8: (a) Particle count density of modeled particles on a beach as a function of wave and position. The color bar indicates the count density. This individual simulation starts with 1000 particles evenly distributed from 0 to L_{rms} on a beach. (b) Run-ups and median positions as a function of wave. The black points represent the median position and the light blue line represents the run-ups for each wave.

3.3.2 Beached particle residence time

While an individual simulation provides insight into the dynamics of particles on a beach from wave to wave, averaging over many simulations allows us to smooth out the jumps and isolate overall trends. Therefore, we run 300 simulations with the same initial parameters as the baseline simulation ($N_w = 100$, $N_p^0 = 1000$, and $L_{rms} = 1.19$ m), which is sufficient for the ensemble average of the simulations to converge. Figure 3.9 shows the ensemble average heatmap. Again, we see that particles initially move up the beach quickly and continue to move upward at a decreasing rate over time. Unlike the single simulation, we see a broad distribution in particles both above and below the median position and a smooth evolution of the median position. Therefore, while on average we expect the transport of buoyant particles in the swash to follow a smooth trend, transport in individual realizations occurs in discrete jumps.

Next, we analyze the rate at which particles leave the beach by plotting the fraction of particles remaining on the beach N_p/N_p^0 over time in Figure 3.10a. In this plot, the black line represents the ensemble average over the simulations, while the light blue lines represent a subset of individual simulations. As expected, N_p/N_p^0 decreases monotonically as particles are removed. Fitting an exponential decay as defined in Section 3.2.4, we estimate a residence time $\tau_r = 268 \pm 12$ wave periods. This quantifies how long it will take for particles which initially start on the beach to be removed by continuous swash waves. Recall that our model only simulates particles leaving the beach and does not account for any input of particles from the surf zone.

We next consider how the median position of the particles that remain on the beach changes over time. In Figure 3.10b, we plot the average median position overlaid on a subset of individual simulations. We observe that the average particle median position moves to over $2L_{rms}$ within the first 10 waves, increasing slowly but continuously after this initial rapid transport. These trends are largely similar to those found in Mørk et al. (2026), where particles quickly reach high positions on the beach before continuing to be transported slowly up the beach.

3.3.3 Sensitivity to wave run-up length

Next, we study how varying the wave run-up distribution affects particle transport and residence time. Because the Rayleigh distribution is fully described by L_{rms}, we vary L_{rms} by varying H_s and keeping β and T constant. We test H_s of 0.2 m, 0.4 m, and 0.6 m resulting in L_{rms} values of 1.19 m, 1.69 m, and 2.07 m, which we label as W1, W2, and W3 respectively. All other parameters match the baseline simulation.

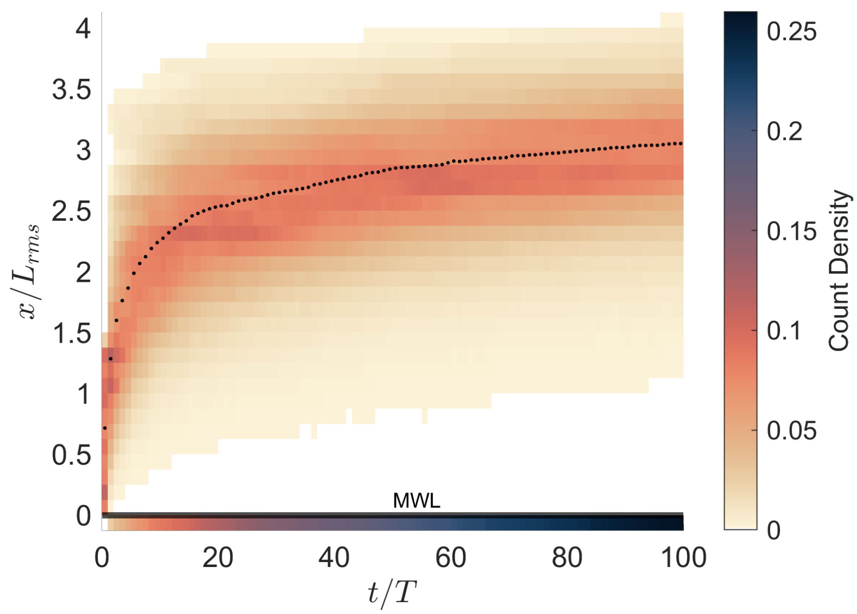

Figure 3.9: Heatmap averaged across 300 simulations. Colorbar represents the particle count density which is the number of particles normalized by the original particle count. The black points represent the average median positions across 300 simulations.

We run 300 simulations for each case.

First, we plot the average heat maps for particle distributions over time in Figure 3.11a for each case. Despite differences in L_{rms}, all three cases show the same qualitative behavior: particles rapidly accumulate near a wrack line. As expected, the particles in W3, the case with the largest L_{rms}, reach the highest absolute positions. The normalized heatmaps in in Figure 3.11b show that the behavior is consistent across cases when scaled by L_{rms}. This is further emphasized by plotting the dimensional and normalized median positions over time in Figures 3.12b and 3.12c, where we see the data collapse when normalized. Thus, L_{rms} is the main control on the particle position on the beach and therefore the wrack line position.

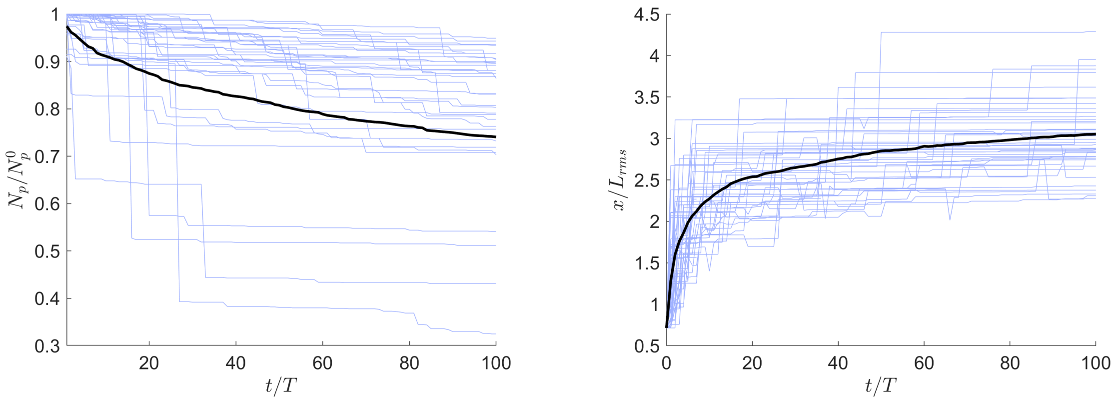

(a)

(b)

Figure 3.10: (a) is the average particle count on the beach as a function of waves. (b) is the average particle median positions on the beach as a function of waves. The dark blue line represents the average value across 300 simulations. Light blue lines represent a random subset of individual simulations from the total 300.

We see some differences between the cases when we analyze the particles remaining on the beach in Figure 3.12a. We also calculate τ_r for each case and find the values to be 450 ± 17, 633 ± 27, and 694 ± 36 wave periods for W1, W2, and W3 respectively. This demonstrates that the smaller run-ups result in smaller τ_r. This can be explained by the fact that smaller run-ups correspond to less energetic waves, meaning that the particles will have higher relative inertia and therefore higher Stokes numbers. In our model, higher Stokes number particles tend to have both a lower probability of beaching and resulting lower positions on the beach after being hit by the waves. This illustrates that changing L_{rms} for a given wave run-up distribution has a strong effect on particle residence time.

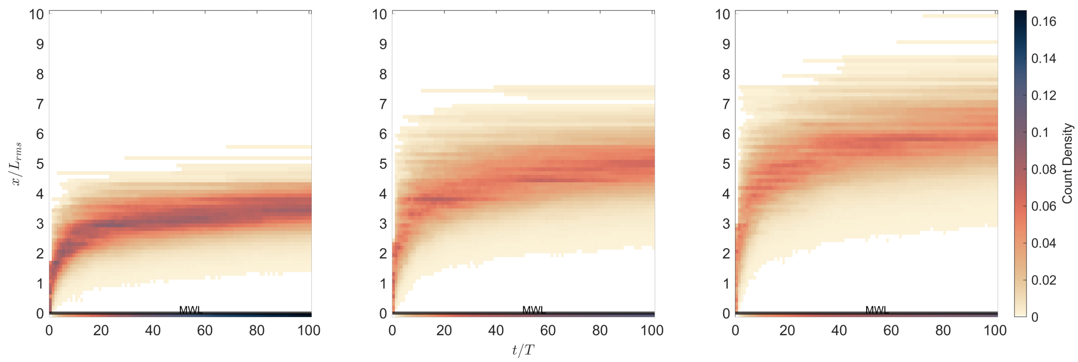

(a)

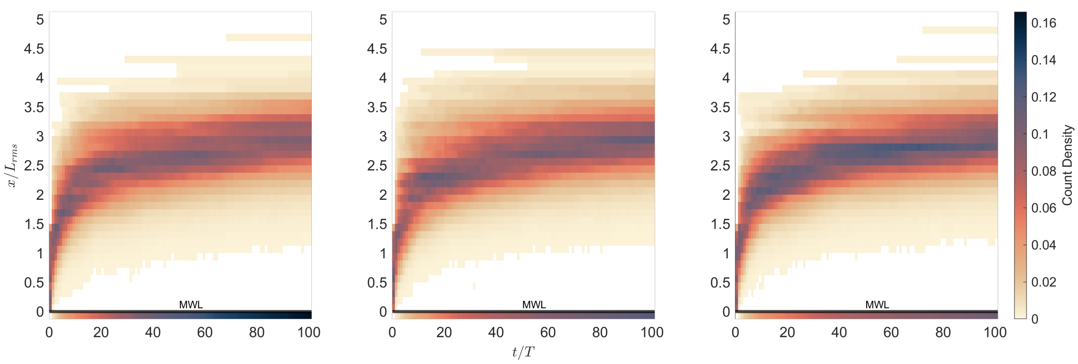

(b)

Figure 3.11: Particle count density of modeled particles on a beach as a function of wave and position, both (a) non-normalized and (b)normalized by L_{rms}, for three different wave distributions (L_{rms} = 1.19 m, L_{rms} = 1.69 m, and L_{rms} = 2.07 m, respectively). The color bar indicates the count density, while each panel represents a different wave distribution. Each heatmap is an average across 300 simulations starting with 1000 particles on the beach.

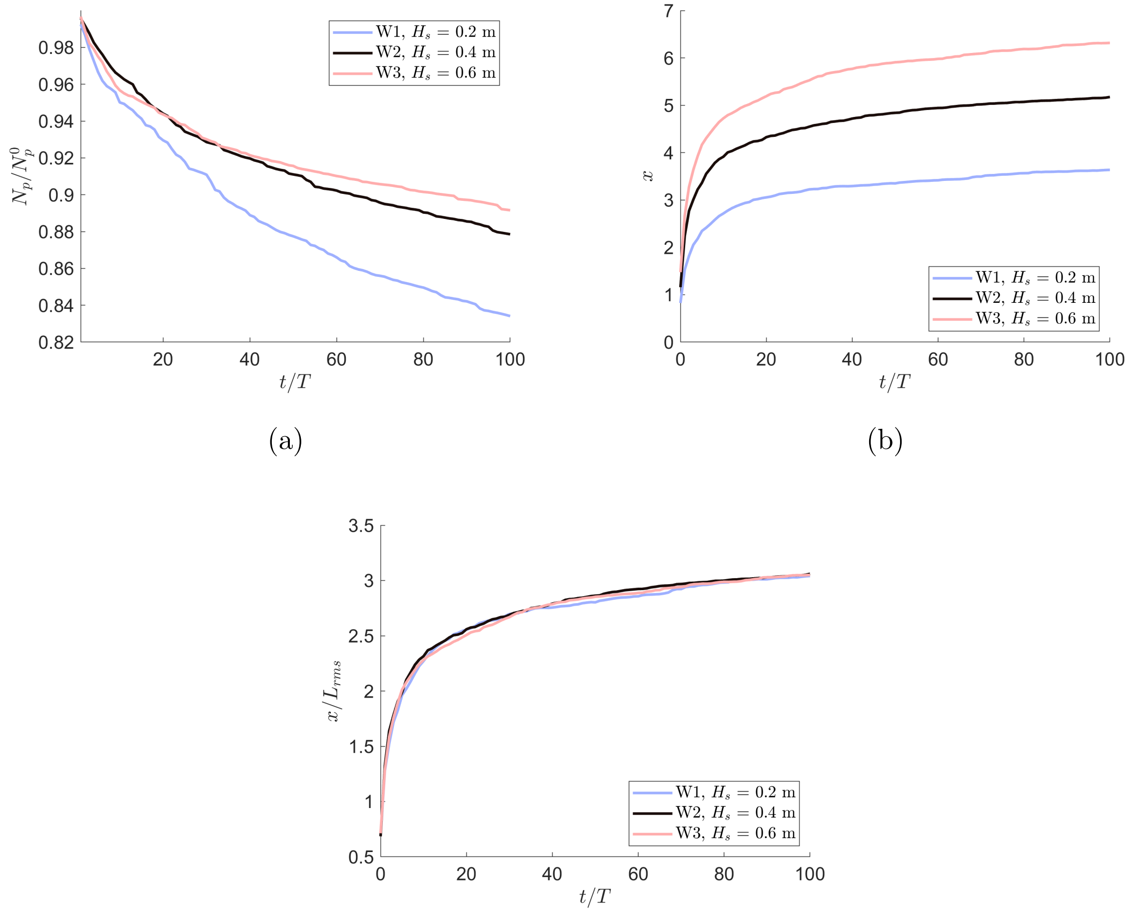

(a) (b)

(c)

Figure 3.12: (a) is the average particle count on the beach as a function of waves and L_{rms}. (b) is the average particle median positions on the beach as a function of waves and L_{rms}. (c) is the non-normalized average particle median positions on the beach as a function of waves and L_{rms}. The colors represent different L_{rms} from the wave distributions. Each line is averaged across 300 simulations.

3.3.4 Sensitivity to particle size

In addition to varying run-up distributions, we also test the sensitivity of the model to particle size. Using the same baseline run-up distribution ($L_{rms} = 1.19$ m), we vary the particle diameter across three values: $d_p = 0.005$ m, 0.007 m, and 0.01 m, referred to as P1, P2, and P3, respectively. We run 300 simulations for each test case.

In Figure 3.13, we plot normalized average heatmaps for the three particle diameters. The plots overall are similar, where we see the P3 test case has the most spread compared to P1 which has the least. This is consistent with P3 particles having an overall higher Stokes number than P1 particles. Higher Stokes number was parameterized to have higher spread because particles are more likely to lag the swash tip and end up lower on the beach.

As before, we see larger differences in the cases when we analyze particle fraction remaining on the beach over time as plotted in Figure 3.14a. In this plot, we see that particle fraction decreases fastest for the largest particle (P3) and slowest for the smallest particle (P1). Again, this can be explained through analysis of the particle Stokes number. Larger particles are more inertial and therefore more likely to lag the swash front and be washed off the beach in the backwash. Thus, the residence times for large particles are shorter compared to those for small particles under the same wave forcing.

Similar to when we varied the wave run-up distributions, all the cases have a similar normalized median position over time as plotted in Figure 3.14b. There is some small variation: the smallest particles (P1) tend to reach slightly higher median positions than P2 and P3. This reflects the fact that the smallest particles will typically have the lowest Stokes numbers, and thus they will be able to be easily mobilized and carried by the wave to the uppermost part of the swash. Ultimately, these results suggest that particle size affects how quickly particles leave the beach, but again the run-up length controls where the remaining particles accumulate.

3.3.5 Synthesis of particle residence times

The previous sections showed how the residence times of particles on a beach varied with both wave run-up length and particle size in ways consistent with their influence

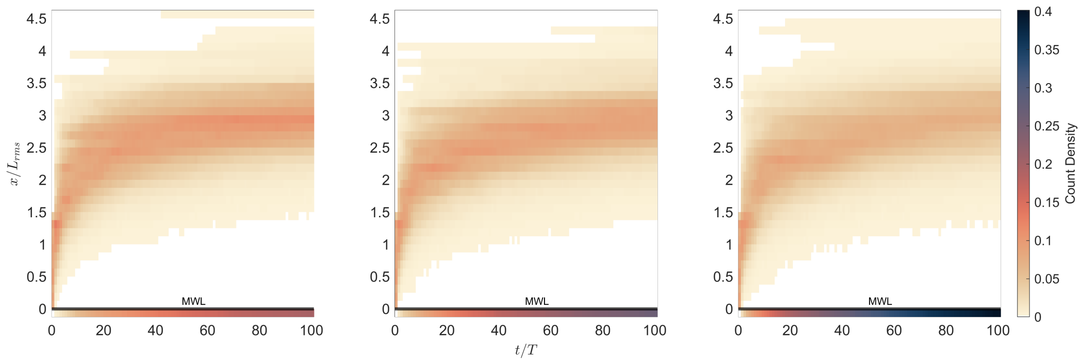

Figure 3.13: Particle count density of modeled particles on a beach as a function of wave and position for three different particle sizes. The colorbar indicates the count density, while each panel represents a different particle diameter d_p. Each panel is an average across 300 simulations starting with 1000 particles on the beach. Note all simulations are for the same wave distribution.

on the particle Stokes number St. For example, smaller run-ups and larger particles produced simulations with the lowest residence times, both of which correspond to larger Stokes numbers. In this section, we now directly analyze τ_r as a function of St.

Given that the St, as we have defined it, varies over each time step and particle position for a given simulation, we define a characteristic St for each simulation to compare across simulations. This characteristic St is defined at the midpoint ($x = 0.5L_{rms}$) of the root-mean-square wave (L_{rms}). Next, we run simulations over a range of d_p (0.005 - 0.01 m), and L_{rms} (1.1-2.9 m), running 300 simulations per scenario. The results of this parameter sweep are plotted in Figure 3.15, where we show the computed residence times as a function of the characteristic Stokes number. These results show that τ_r decreases monotonically with Stokes number, with all the data collapsing onto a single curve. Overall, this is consistent with the previous observations that our simulations with large particles in a distribution of small run-ups (i.e, high St) lead to the lowest τ_r.

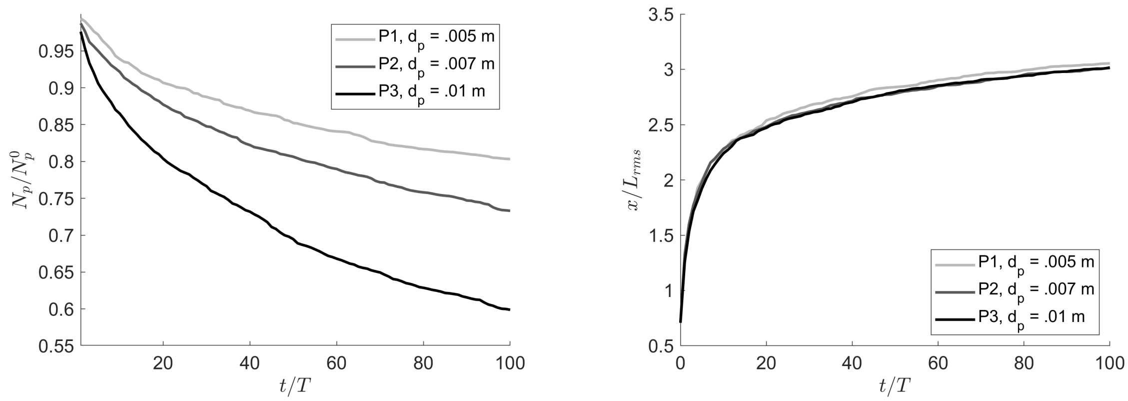

(a) (b)

Figure 3.14: (a) is the average particle count on the beach as a function of waves and d_p. (b) is the average particle median positions on the beach as a function of waves and d_p. The colors represent different particle diameters. Each line is averaged across 300 simulations. Note all simulations are for the same wave distribution.

This finding appears to contrast with Hinata, Mori, et al. (2017) who find that larger particles tend to remain on the beach longer. However, we should not directly compare our studies as their residence times were of particles which could consistently reenter the swash zone from the surf zone. In other words, their analysis includes transport from both the swash and the surf, whereas our study only includes the swash. Additionally, these differences can also come from the distinct particle size regimes. Hinata, Mori, et al. (2017) focused on larger particle regimes (i.e., > 10 mm), as opposed to microplastics. Larger particles high on the beach are significantly less responsive to the flow, especially near the wrack line where the fluid velocities are smallest. Thus, they may often fall in the highest St regime we defined where they are too large to be washed off the beach by most waves. Overall, while particle Stokes number controls τ_r in our simulations isolated to small particles in the swash zone, the relationship likely becomes more complex when larger particles and surf zone

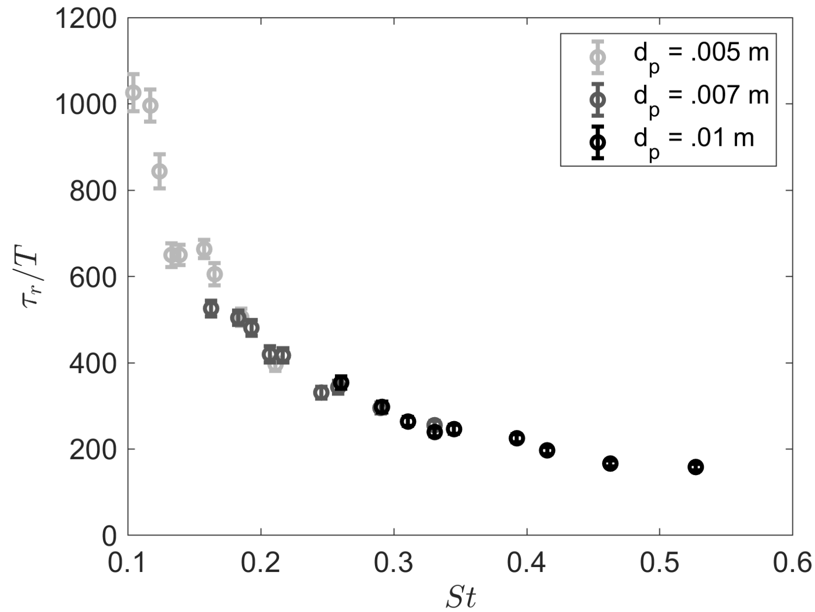

Figure 3.15: Normalized average particle residence time by the wave period T as a function of characteristic Stokes number. Each point represents the average across 300 simulations. Errorbars represent the 95% confidence intervals from the exponential fitting of τ_r. Each color represents the particle diameters listed in the legend.

dynamics are included.

3.3.6 Effects of tides

We finally examine how tides affect particle dynamics in our simulations by incorporating a sinusoidal tidal model, following the approach of Mørk et al. (2026). We use the same particles as in the baseline simulation: diameter $d_p = 0.005$ m, height $h_p = 0.00079$ m, and density $\rho_p = 970$. The wave run-up distribution is defined by the beach slope $\beta = 0.11$, wave period $T = 6$ s, and significant wave height $H_s = 0.5$ m, which results in an L_{rms} of 2.52 m. The tidal amplitude, or tidal excursion length, is first defined as $x_{tide} = 0.5L_{rms}$, which here represents a microtidal regime (Bosboom et al., 2023). Tides are modeled as a sinusoidal function of time, where at $t = 0$ the MWL is at $x = 0$ and at $t = 3$ hr the MWL reaches the maximum (or minimum) tidal amplitude, corresponding to one quarter of a semidiurnal tidal cycle. We simulate three-hour cycles ($N_w = 1350$) with $N_p^0 = 1000$ particles for three different test cases: a rising tide, a falling tide, and a no-tides control.

In Figure 3.16a, we show the particle fraction remaining on the beach over time alongside the tidal excursion curves. Simulations with a falling tide retain the most particles, while the rising tide retains the fewest. This result can be explained by particles being stranded on the beach as the water recedes during a falling tide, causing the particles to effectively be out-of-reach by subsequent wave run-ups. This is a similar result discussed in Mørk et al. (2026), where they find that the number of particles on the beach is maximized during falling tides. Meanwhile, a rising tide results in the fewest particles on the beach; as the MWL rises, particles are more likely to be impacted by run-ups, even if they are at the wrack line at previous time steps.

Next, we plot the median positions of particles during a rising tide, a falling tide, and no tides. In this analysis, we define two distinct median positions: 'global' and 'local'. The global median positions represent the median position of the particles relative to the original MWL or $x = 0$, while the local median positions refer to the mobile MWL or $x = x_{tide}(t)$. In Figure 3.16b, we plot the global medians as a function of time and see a large difference between test cases. As expected, the rising tide case leads to a higher global median because run-ups are consistently moving farther up the beach, causing particles that stay on the beach to move up with the wrack line. In contrast, during a falling tide, particles are decreasingly likely to be impacted by run-ups, meaning the wrack line remains consistent after initial formation. Next, we plot the local medians as a function of time in Figure 3.16c. This plot shows lower variation between the cases. Yet, it shows that in a rising tide, particles remain closer to the MWL compared to those in a falling tide. Inherently, this result makes sense, as the rising MWL is constantly approaching particles remaining on the beach. However, in a falling tide, particles are more likely to be stranded early due to quick transport up the beach and a receding MWL, leading to larger local median positions.

To explore a broader parameter range, we run additional simulations varying both the tidal excursion lengths and particle size (d_p = 0.005 m, 0.007 m, and 0.01 m). We vary x_{tide}/L_{rms} from -1 to 1 where a negative value refers to an initially falling tide and a positive value refers to an initially rising tide. In Figure 3.17, we plot the final particle fraction remaining on the beach as a function of normalized tidal excursion for each particle diameter. Note that rather than reporting τ_r, we plot the fraction remaining because the tidal forcing disrupts the clean exponential decay that characterizes the no-tide case. Even so, we find that the remaining particle fraction behaves similarly to τ_r as a function of particle size, where it decreases with increasing particle size. With respect to the tides, for a constant particle size we observe that final particle fraction decreases with an increasing rising tide and increases with an increasing falling tide. This indicates that larger falling tides are likely to leave more particles on the beach, as the MWL retreats more quickly in these cases.

3.4 Conclusions and future work

Our model utilizes wave and particle parameters to predict the transport of microplastics on a beach for a specified run-up distribution. By using inputs to derive a Stokes number St, we can predict particle beaching using empirically-derived beaching probabilities, applicable to isolated beaches with small run-ups. After running several simulations, we find that particle residence times τ_r are a function of both run-up lengths and particle sizes. Namely, residence time decreases with smaller run-up length and larger particle sizes. A small run-up length and a large particle size results in a high St; therefore, a high Stokes number would also lead to a shorter residence time. This result aligns with particle positions on the beach, such that high Stokes number particles reach lower median positions. In general, particles are quickly transported to

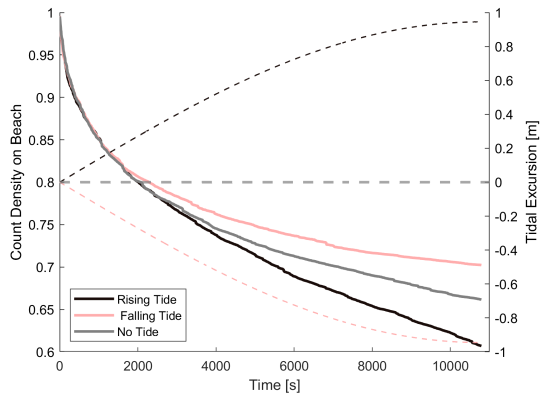

(a)

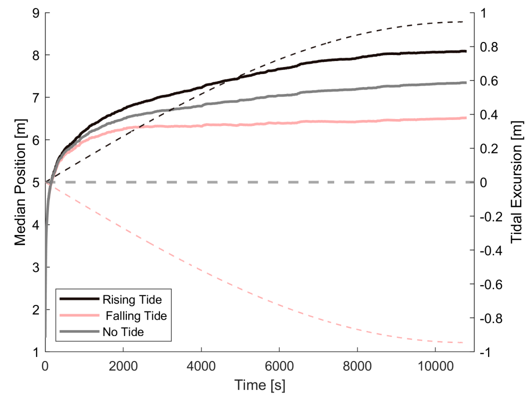

(b)

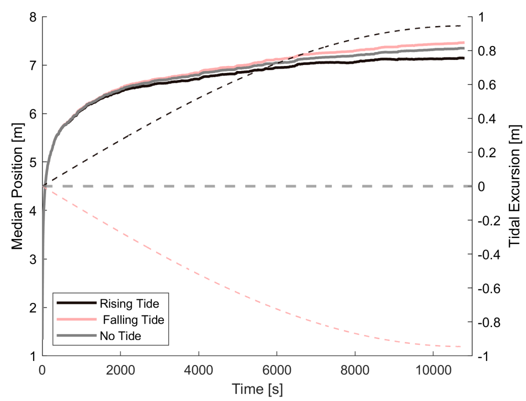

(c)

Figure 3.16: (a) is the average particle count on the beach as a function of waves and tidal variation. (b) is the global average particle median positions on the beach as a function of waves and tidal variation. (c) is the local average particle median positions on the beach as a function of waves and tidal variation. The colors differentiate whether the simulations start with a rising or a falling tide. Solid lines correspond to the left Y axis and are the averages of 300 simulations. Dotted lines correspond with the right Y axis and represent the position of the mean water line.

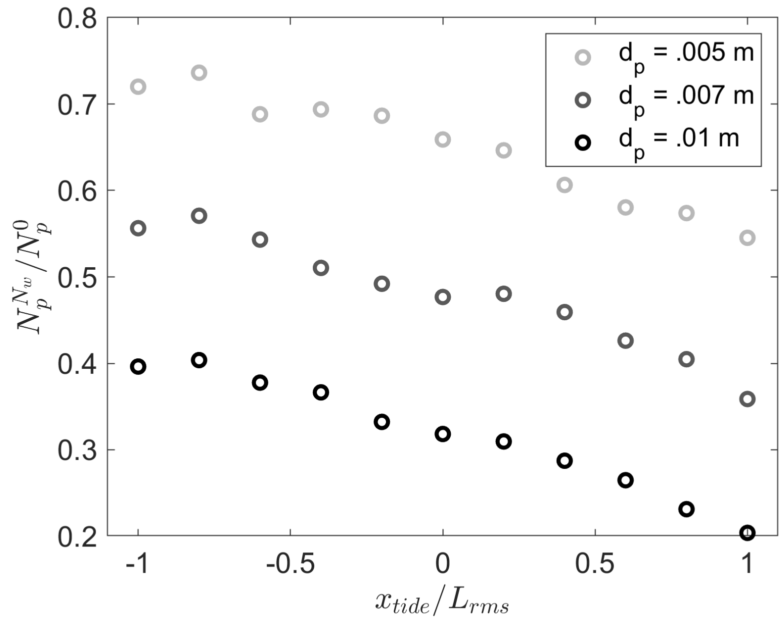

Figure 3.17: Final fraction of particles remaining on the beach as a function of normalized tidal excursion. Each point is the average across 300 simulations. The legend indicates the particle diameters used in the simulations.

high median positions or the wrack line and are continually pushed up the beach by large run-ups. However for higher St, particles are more likely to be spread below the wrack line, thus they are more frequently impacted by run-ups resulting in more particles leaving the beach.

Regarding tides, we find that a falling tide is likely to strand particles, leading to an increase in residence times. Conversely, a rising tide leads to more frequent run-up impacts; thus, particles are more susceptible to be washed off. In addition to tidal direction, tidal excursion length impacts residence time: larger falling tides lead to larger residence times on the beach, while larger rising tides are associated with smaller residence times. These trends are consistent for different particle sizes, although the magnitude may differ. Overall, our model predicts that smaller run-ups, larger particles, and rising tides all contribute to a decrease in the amount of particles that remain on the beach. For particles that remain on the beach, they generally accumulate near the wrack line, which is a function of the wave run-up lengths.

However, future work is necessary to improve model accuracy and applicability. Currently, this model only considers residence times and positions of particles on the beach. It does not include locations for particles that wash off the beach nor particles reentering the beach from the surf zone due to the lack of reliable statistical models. As a result, count densities differ between simulations and field observations. Therefore, it is important to develop a reliable, physics-informed statistical model to predict particles entering/exiting the surf zone.

Chapter 4

INCIPIENT MOTION OF BUOYANT PARTICLES IN THE SWASH ZONE

4.1 Motivation

In general, there is limited literature on the physics surrounding microplastic transport in the swash zone. Conversely, the transport of particles, like sediment, has a relatively large body of research. While both are particulates that are transported by the fluid flow, their transport can differ due to differing physical parameters, particularly when comparing sediments with buoyant microplastics. These physical differences complicate the direct application of sediment transport models to buoyant microplastics; however, sediment models may still inform buoyant microplastics transport.

Considering an open channel flow, previous work by Cowger et al. (2021) derives a modified Rouse profile, which is a measure of suspended sediment concentrations in a water column, for buoyant microplastics by considering buoyant particle rise velocity. This model predicted that smaller buoyant microplastics (0.3-1 mm) are more spread throughout the water column, due to smaller rise velocities, when compared to larger buoyant particles (1-5 mm). Using this modified Rouse profile, further work by Wickramarachchi et al. (2026) simulated buoyant microplastic transport modes of particles starting at the water's surface. They found that buoyant microplastics remain close to the water's surface and travel as a 'surface' load. However, it is important to note that these results are based on an open channel flow scenario. As opposed to open channel flows, flows in the swash zone are primarily wave-driven and unsteady, which means flow velocities are not constant and can depend on location along the beach.

As a result, the transport of buoyant microplastics in the swash zone can differ from open channel models and requires further research.

A recent work (Davidson et al., 2023) studied the transport of buoyant particles in the swash zone and aimed to identify important parameters that determine beaching. However, this study, along with previously discussed open channel flow studies, focuses on particles that start on the water's surface. For buoyant particles on a beach, they do not start at the water's surface, but rather they are initially submerged when hit by a wave, and then they lift from the bed to reach the water's surface. Thus, there is a necessity to explore the initial phases of particle transport mechanisms for buoyant particles on the beach in a swash flow. Abarca et al. (2026) explored how a buoyant particle's initial conditions on the beach impact their transport. In these experiments, we identified that our Stokes number at wave impact correlates with particle beaching, where a low Stokes number leads to higher particle beaching. Since these results contrast with previous work (Davidson et al., 2023), there are questions surrounding the correct Stokes number definition, and specifically determining the correct particle timescale. Therefore, we are motivated to explore the characteristic timescale for buoyant particles lifting off the bed after they are hit by a swash wave.

To explore this timescale, we need to understand their initial removal from the bed, which is referred to as their incipient motion. The incipient motion of particles from the bed governs when and how particles are transported. In this chapter, we first review the concept of incipient motion as it applies to negatively buoyant particles and sediment. This review focuses on the physical mechanisms that determine if a particle is removed from the bed. However, as opposed to negatively buoyant particles, incipient motion for positively buoyant particles is not a question of whether a particle will move, but when. Therefore following review of non-buoyant particles, we discuss the incipient motion of positively buoyant particles in the swash zone and propose a new way to characterize this incipient motion considering relevant forces.

4.2 *Incipient motion of a particle*

4.2.1 Sediment

The incipient motion of sediments by fluid motion is famously summarized in the work of Shields (1936). Shields defined a relationship of opposing mechanisms: shear stress τ that lifts particles from the bed and gravity that weighs the particle down. This relationship is summarized as the Shields parameter, also known as the nondimensional shear stress:

$$\theta = \frac{\tau}{(\rho_s - \rho_f)gD}, \tag{4.1}$$

where ρ_s is the sediment density, ρ_f is the fluid density, and D is the characteristic grain size. Specifically, the Shields parameter is defined for critical shear stress, where "critical" refers to the point sediment motion begins (Selim Yalin et al., 1979). This means that when shear stress reaches the critical value ($\tau = \tau_c$), then the corresponding Shields parameter is θ_c. As demonstrated by Shields (1936), the critical Shields parameter θ_c varies as a function of boundary Reynolds number Re_c, which describes flow conditions around the sediment bed (Buffington, 1999). Boundary Reynolds number is defined as $Re_c = u_c^* D/\nu$, where u_c^* is the critical shear velocity for incipient motion. The relationship between θ_c and Re_c is illustrated by the Shields curve in Figure 4.1. The Shields curve predicts the stress at which particle incipient motion occurs; particles above the curve are expected to move from the bed, while those below the curve do not experience enough lift to overcome gravity and incite motion. Note that this analysis only applies to negatively buoyant particles where gravity is opposing the shear-induced lift.

In the swash zone, shear stresses at the bed are higher during uprush compared to backwash (Barnes, O'Donoghue, et al., 2009), resulting in higher mobilized sediment concentrations during the initial swash phase. Previous work (Masselink, Evans, et al., 2005) aimed to characterize suspended sediment concentrations in the swash zone due to shear stresses using the Shields parameter θ. They analyzed an ensemble-averaged

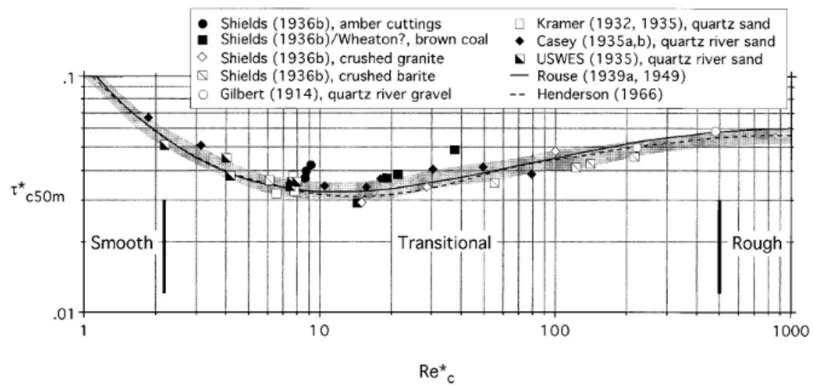

Figure 4.1: $\tau*_{c50m}$ or θ_{c50m} plotted as a function Re_c, provided by Buffington (1999). The subscript $50m$ represents the use of the median grain size for D, such that $D = D_{50m}$.

swash event to average over the effects of turbulence and velocity fluctuations when deriving instantaneous shear stresses. As expected, results show that higher values of θ correspond with increased sediment concentrations, where peak values occur during uprush.

Along with shear stresses, incipient motion of sediments in the swash zone can be caused by bore-generated turbulence. Other field studies (Butt et al., 2004; Puleo, Beach, et al., 2000) have investigated overall turbulent kinetic energy (TKE) and its impact on sediment concentrations. Swash zone TKE comprises of both turbulence from wave breaking and turbulence generated by bed shear. These studies demonstrate that high suspended sediment concentrations do correlate with high TKE values, particularly during uprush. In summary, the incipient motion of sediment in the swash zone is more complex compared to a channel flow, due to turbulence both advected from wave breaking and generated from bed shear stress.

4.2.2 Negatively buoyant microplastics

When compared to sediment transport, there is less literature on the incipient motion of negatively buoyant microplastics. Despite limited literature, previous experiments by Waldschläger et al. (2019), expanded upon by Goral et al. (2023), study the incipient motion of negatively buoyant microplastics in an open channel. These experiments involve placing microplastic particles on top of a sediment bed, gradually increasing the surrounding flow speed in the channel, and recording the speed at which particles initially move from the bed. The goal is to derive a Shields parameter for microplastic particles that accounts for both particle shape and the hiding-exposure effect. The hiding-exposure effect refers to the extent to which a plastic particle is covered by surrounding sediments, where smaller particles tend to be more hidden, while larger particles that are more exposed (Waldschläger et al., 2019; Yu et al., 2023). Using data from these experiments, Goral et al. (2023) established a framework that predicts the incipient motion of microplastics, demonstrating that their results fit within the transitional regime of a Shields curve, modified by considering particle shape, friction, and hiding-exposure. Despite the need for small modifications, these studies show that existing sediment transport models can be generally extended to negatively buoyant microplastics. Building on experimental results, Kramer (2025) derived a plastic Shields number which is applied in a model by Wickramarachchi et al. (2026) to predict the incipient motion of negatively buoyant microplastics in an open channel. Model results suggest that this modified Shields parameter can predict the incipient motion of negatively buoyant plastics from a sediment bed, as shown by a comparison of model data and previous experimental data plotted on a modified Shields curve. While highlighted works present a promising framework, they are focused on an open channel scenario, so there remains a need to study the incipient motion of these non-buoyant plastic particles in the swash zone.

There have also been a number of experimental studies which analyzed negatively buoyant microplastic transport in wave tanks (e.g., Guler et al. (2022) and Núñez et al. (2023)). Although these studies measure particle transport in the surf and swash zone, they do not specifically address the incipient motion of the particles. While general incipient motion models can be extended to negatively buoyant microplastics, there is uncertainty regarding the applicability to the swash zone due the varying initial conditions (i.e., flow speed is variable in time and space on a beach). Moreover, these uncertainties are amplified when considering buoyant microplastics because the balance of forces changes.

4.2.3 Positively buoyant microplastics

As discussed, the Shields parameter describes the incipient motion of negatively buoyant particles in a flow by analyzing the balance of shear stress and gravity. However, this balance breaks down when applied to positively buoyant particles, which represents roughly half of all microplastics in the ocean (Geyer et al., 2017). On a bed, submerged buoyant microplastics experience a net upward buoyancy force which acts in the same direction as the lift due to shear stress. Consequently, the Shields parameter no longer predicts incipient motion from the bed for positively buoyant microplastics. Considering this, previous work (Kramer, 2025) re-defined the 'Shields' parameter Θ for buoyant particles by focusing on the free surface, where shear stress opposes buoyancy. Thus, the Θ parameter determines whether floating microplastics will detach from the surface due to flow, similar to how the Shields parameter applies to particles lifting off the bed. Using this buoyant 'Shields' parameter, a model by Wickramarachchi et al. (2026) attempted to predict motion of buoyant particles from the free surface in an open channel flow scenario. They find that buoyant particles mostly remain at the free surface, and travel as a surface load. However, these results are for buoyant particles starting at the free surface in an open channel flow. This framework can not necessarily be applied to the swash zone where particles initially start on the beach and are not mobilized until they are impacted by an incoming wave. Therefore, we need a new framework to describe the incipient motion in the swash zone of buoyant particle motion from the bed, and not the surface.

From our literature review, we find that there are no studies focused on the incipient motion of buoyant microplastics on a beach. While our previous experiments measured the physical mechanisms that govern the transport of buoyant microplastics starting on the beach (Abarca et al., 2026), we focused on the particle's net transport and not the incipient motion. Moreover, our results suggest that the initial impact of the wave on the particle and the particle's inertia significantly impacts the particle's fate in the swash zone. However, this study did not take a detailed look at the particle's initial motion from the bed. Instead, we predicted a timescale to characterize this initial motion using a model for the particle's drag force from the fluid flow. This timescale is thought to relate to the buoyant particle's incipient motion, describing the time it takes for a buoyant particle on a beach to accelerate from rest to the surrounding fluid velocity after it is initially submerged by an incoming swash wave. In the following sections, we analyze the relevant forces for particles impacted by a swash wave, consider different potential timescales, and compare them to measured experimental values.

4.3 Methods

4.3.1 Relevant forces on the particle

First, we identify the forces acting on a particle in a swash flow. In the swash zone, we consider particles that are initially at rest on the beach before they are impacted by an incoming swash wave. Upon impact, particles are quickly submerged, as the swash bore flows over the particle. As previously discussed for sediments or negatively buoyant particles, the relevant forces for motion are the forces due to the external flow over the particle which generates a drag force in the direction of the flow and an upward lift force. The particle also has a net gravitational force downward and resistance due to bed friction opposing the flow, as shown in Figure 4.2a. The particle may move if the upward lift force can overcome gravity, and/or the drag can overcome resistance due to friction.

Next, we consider how the picture might change when the particle is buoyant. As in our experiments, we consider a disk particle resting flat on an impermeable bed. For simplicity, we assume the bed is horizontal. The particle is fully exposed, i.e., it is not covered by any sediment, and it is initially surrounded by air.Upon initial impact of an uprushing swash bore, the particle becomes submerged and is subjected to forces that both incite and resist motion from the bed. Similar to a negatively buoyant particle, there is a drag force from the outer flow F_D opposed by friction drag from below the particle F_f in the horizontal. In the vertical, the balance of relevant forces changes. For a buoyant particle, there is a net buoyancy force F_B acting upward, where here this force includes the gravitational weight and buoyancy. There can also be an additional upward force due to lift F_L from the flow traveling over the particle, shown in Figure 4.2b. In this case, the buoyant particle will always rise, as opposed to the negatively buoyant particle which doesn't necessarily move. However as the buoyant particle rises from the bed, a thin gap of fluid can form underneath the particle.As fluid flows into this gap, there will be a low pressure region resulting in a 'suction' force which will resist the upward motion of the particle. We will refer to this 'suction' force as the lubrication force F_ℓ. While lubrication forces can also be important for negatively buoyant sediment particles, this can be especially relevant for a buoyant, flat microplastic due to the formation of thin gaps under the particles and large contact areas with the bed (i.e., compared to spherical sediments). Overall, this means that for an initially submerged buoyant particle, incipient motion is not a question of if, but rather when a particle will move from the bed. This is due to the net buoyancy force F_B, which is dominant and causes the particle to lift off the bed. Therefore, the relevant forces to characterize incipient motion are shown in Figure 4.2c.

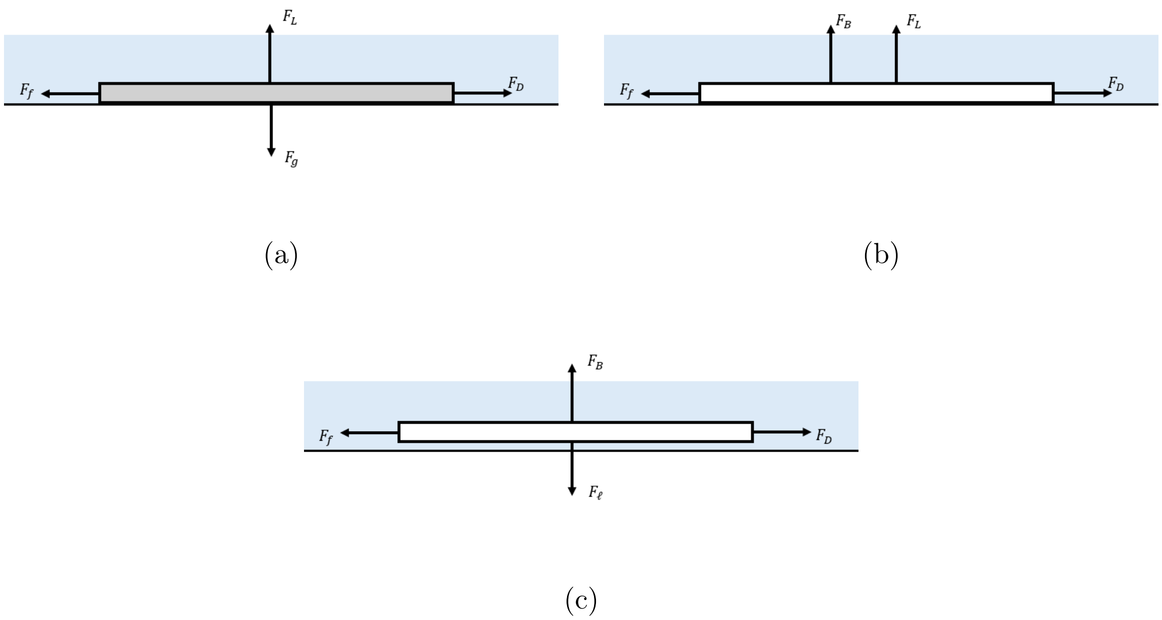

Figure 4.2: Schematic of forces acting on a (a) negatively buoyant particle, (b) a positively buoyant particle on the bed, and (c) a positively buoyant particle rising in a swash flow. Note: not to scale.

Our goal is to define a timescale which characterizes how long it takes for the particle to be "picked up" by the flow.Here we want to derive a timescale considering directly the forces in the vertical direction, similar to the balance of forces that give rise to the Shields parameter. Because we are considering a flat particle in a decelerating flow, the contribution of an initial F_L is likely small compared to buoyancy, which we show in Appendix E. Thus, we focus on the vertical forces due to buoyancy F_B and opposing force that occurs due to lubrication between the bed and the particle F_ℓ. In this section, we will derive a timescale for particle incipient motion due to F_ℓ using lubrication theory and compare it both to predictions from τ_p due to the drag force (reported in Chapter 2) and estimates of the timescale for particle pickup measured in our experiments τ_{exp}.

4.3.2 Lubrication timescale derivation

We consider the flow induced in a thin layer below the disk, between the disk and the bed, as it is initially lifted up. This exactly mirrors the flow described in a paper on the final stage of a falling plate (Wang, 1977). The problem is sketched for a cylindrical coordinate system (r, θ, z) in Figure 4.3, which considers a fully submerged positively buoyant disk (particle diameter d_p and particle height h_p) that is beginning to rise vertically off a flat, impermeable bed. For this scenario, we make the following assumptions: 1) there is no surrounding flow, thus no additional forces from the fluid (i.e., $F_D = 0$), 2) flow under the particle is incompressible (i.e., $\nabla \cdot \vec{u} = 0$), 3) the flow and particle are axisymmetric (i.e, $\partial/\partial\theta = 0$), and 4) the particle does not rotate about its axis (i.e., $u_\theta = 0$). Using these assumptions, we reduce the cylindrical Stokes equations:

$$\rho \left(\frac{\partial u_r}{\partial t} + u_r \frac{\partial u_r}{\partial r} + u_z \frac{\partial u_r}{\partial r} \right) = -\frac{\partial P}{\partial r} + \mu \left(\frac{1}{r} \frac{\partial}{\partial r} \left(r \frac{\partial u_r}{\partial r} \right) + \frac{\partial^2 u_r}{\partial z^2} - \frac{u_r}{r^2} \right), \tag{4.2}$$

$$\rho \left(\frac{\partial u_z}{\partial t} + u_r \frac{\partial u_z}{\partial r} + u_z \frac{\partial u_z}{\partial r} \right) = -\frac{\partial P}{\partial z} + \mu \left(\frac{1}{r} \frac{\partial}{\partial r} \left(r \frac{\partial u_z}{\partial r} \right) + \frac{\partial^2 u_z}{\partial z^2} \right) - \rho g. \tag{4.3}$$

Now, we apply lubrication theory to this scenario. For lubrication theory, the flow must be in a thin gap, such that the vertical lengthscale of the gap is much smaller than the horizontal lengthscale. In this scenario, the gap height is denoted as h, and the length of the gap is the particle diameter d_p, thus $h \ll d_p$. To apply this limit, we scale the Stokes equations, such that $r \sim d_p$ and $z \sim h$, to result in:

$$\frac{\partial^2 u_r}{\partial z^2} = \frac{1}{\mu} \frac{dP}{dr}, \tag{4.4}$$

$$\frac{dP}{dz} = -\rho g. \tag{4.5}$$

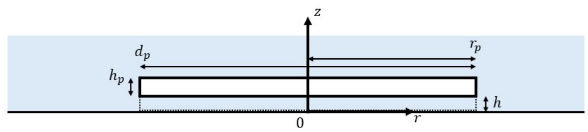

Figure 4.3: Schematic of a simple scenario where a buoyant disk just rises off the bed. The dotted box represents a control volume. Note: not to scale.

This shows us that the horizontal flow is governed by a pressure-viscous balance below the plate, and the vertical pressure gradient is hydrostatic. To derive the fluid velocity, we assume a no-slip boundary condition at both the particle and the bed, giving the following boundary conditions:

$$u_r = 0 \text{ at } z = 0, h. \tag{4.6}$$

Applying these boundary conditions, we integrate Equation 4.4 over the depth of the thin layer h to find the radial flow u_r underneath the particle as a function of the radial pressure gradient. The resulting expression gives us planar Poiseulle flow:

$$u_r(z) = \frac{1}{2\mu}\frac{dP}{dr}z(z-h). \tag{4.7}$$

In this scenario, water flows in below the particle from the sides as the particle rises at a speed v_z. The particle rising expands the volume of the thin layer below the particle which is balanced by the inflow, enforcing conservation of mass. To solve for the vertical fluid velocity u_z, we use the continuity equation in cylindrical coordinates (neglecting azimuthal terms):

$$\frac{1}{r}\frac{\partial}{\partial r}(ru_r) + \frac{\partial u_z}{\partial z} = 0. \tag{4.8}$$

Substituting Equation 4.7 into Equation 4.8 gives a differential equation for u_z in terms of the pressure gradient:

$$\frac{\partial u_z}{\partial z} = -\frac{1}{r}\frac{\partial}{\partial r}\left(r\left(\frac{1}{2\mu}\frac{dP}{dr}z(z-h)\right)\right). \tag{4.9}$$

Next, we integrate Equation 4.9 over the water depth under the particle:

$$\int_0^h \frac{\partial u_z}{\partial z}\,dz = \int_0^h -\frac{1}{r}\frac{\partial}{\partial r}\left(r\left(\frac{1}{2\mu}\frac{dP}{dr}z(z-h)\right)\right)\,dz, \tag{4.10}$$

$$v_z - 0 = -\frac{1}{r}\frac{\partial}{\partial r}\left(r\frac{dP}{dr}\right)\left[\frac{z^3}{3}-\frac{hz^2}{2}\right]\Bigg|_0^h, \tag{4.11}$$

where here we applied the boundary conditions where v_z corresponds to the vertical fluid velocity at the particle height h such that $u_z(z=h)=v_z$, and $u_z(z=0)=0$ enforcing impermeability at the bed. The resulting equation gives v_z defined in terms of the radial pressure gradient:

$$v_z = \frac{h^3}{12\mu}\frac{1}{r}\frac{\partial}{\partial r}\left(r\frac{dP}{dr}\right). \tag{4.12}$$

From here, we can solve for the pressure on the underside of the particle to determine the lubrication force. We rearrange to isolate pressure on the left-hand side:

$$\frac{\partial}{\partial r}\left(r\frac{dP}{dr}\right) = \frac{12\mu v_z r}{h^3}. \tag{4.13}$$

Before we integrate, we define two boundary conditions: 1) given that we assumed our particle (and the flow) was axis-symmetric, the horizontal pressure gradient $\frac{\partial P}{\partial r}$ must be equal to 0 at the particle's center, and 2) the pressure beyond the the radius of the particle is given by some reference pressure P_0:

$$\frac{dP}{dr} = 0 \text{ when } r = 0, \tag{4.14}$$

$$P = P_0 \text{ at } r = r_p \text{ where } r_p = d_p/2. \tag{4.15}$$

After integrating Equation 4.13 twice, applying both boundary conditions, and rearranging, we obtain an expression for the pressure P on the underside of the particle as a function of the vertical velocity of the particle v_z:

$$P = -\frac{3\mu v_z}{h^3}\left[r_p^2 - r^2\right]. \tag{4.16}$$

Using this expression for pressure, we can now derive the lubrication force F_ℓ by integrating the pressure over the particle's surface area to yield:

$$F_\ell = \frac{3\pi\mu v_z r_p^4}{2h^3}. \tag{4.17}$$

This is the net lubrication force due to the viscous inflow underneath the particle within a thin layer as it is lifted up. Now that we have defined the force, we consider the relative timescale over which this force is important.

As previously stated, the lubrication force resists the motion of a particle off a bed, but it does not completely prevent it. Thus, there is a characteristic timescale during which F_ℓ slows the particle which should determine how fast the particle can move away from the bed into the outer flow. We consider when the particle is first picked up and viscous forces dominate. In this case, we neglect the particle inertia as it it initially very small, and analyze the system when the buoyancy force balances the lubrication force, $F_B = F_\ell$:

$$(\rho_f - \rho_p) g (\pi r_p^2 h_p) = \frac{3\pi\mu r_p^4}{2h^3}\frac{dh}{dt}. \tag{4.18}$$

Note that we have rewritten v_z as dh/dt which is the change in particle height over time.

To find the timescale τ_ℓ, we integrate Equation 4.18 over time. Here, we need to decide on the bounds for integration. At $t = 0$, we define the initial height of the thin layer below the particle to be a roughness height characteristic of the bed h_0. The bed roughness height serves as an initial estimate for the minimum depth between the particle and the bed. We set the upper bound of the time integration to $t = \tau_\ell$ which corresponds to when the water depth below the particle is some 'lubrication' height $h = h_\ell$. Physically, this lubrication height refers to the height of water below the particle where the particle is fully lifted from the bed, leading to a significant weakening of F_ℓ where it becomes negligible. We leave these as a general parameter for now but analyze the sensitivity between τ_ℓ and the choice of h_ℓ in the next section.

Finally, with these bounds, we integrate the rearranged Equation 4.18:

$$\int_0^{\tau_\ell} dt = \int_{h_0}^{h_\ell} \frac{3\mu r_p^2}{2h_p g(\rho_f - \rho_p)} \frac{1}{h^3}\, dh. \tag{4.19}$$

After substituting $r_p = d_p/2$, we find τ_ℓ to be:

$$\tau_\ell = \frac{3\mu d_p^2}{16 h_p g(\rho_f - \rho_p)} \left(\frac{1}{h_0^2} - \frac{1}{h_\ell^2}\right), \tag{4.20}$$

which we see depends on the roughness and lubrication heights such that $\tau_\ell \sim \left(\frac{1}{h_0^2} - \frac{1}{h_\ell^2}\right)$. Overall, we see that the larger the particle diameter, the longer the timescale, and that the smaller the roughness height, the longer the timescale.

4.3.3 Experimental timescale

Next, we re-examine the data from our previously reported experiments in Chapter 2. To summarize, we initialize particles on the beach prior to a swash event. The particles remain at rest until impacted by an incoming swash wave. Once hit, the particles are quickly submerged and we track their transport. While we previously focused on the net transport, in this chapter we focus in the initial transport. From the particle tracking, we estimate a timescale t_{exp}, which represents the time it takes for particles to begin moving after initially being hit by the swash bore. As discussed in Chapter 2, tracking particle motion during initial wave impact was difficult due to the initially high speed of the bore and light refraction off the water surface.

Due to these experimental constraints, we cannot track all of the particles at the initial wave impact. Instead, we take a subset of the best images with minimal light refraction and analyze those. Subsets represent about 75% of the total data. We define t_{exp} as the time it takes a particle to move half a diameter in length, i.e., from $x = x_0$ to $x = x_0 + d_p/5$. While this choice is somewhat arbitrary, the bounds were chosen for two main reasons: 1) particle diameter is a measurable distance that can be applied across test cases, and 2) the resulting t_{exp} values from tracking are reasonable estimates, as they are close to timescales manually measured in experimental videos.

4.4 Results

4.4.1 Lubrication timescale

We next analyze the expression for τ_ℓ as a function of h_ℓ in the context of our swash zone experiments (Abarca et al., 2026). We use the fluid parameters of water (i.e., $\rho_f = 1000$ kg/m^3 and $\mu = 10^{-3}$ Pa $\cdot$ s) and define particle parameters as follows: diameter d_p of 0.005 m, height h_p of 0.00079 m, and density ρ_p of 970 kg/m^3. The roughness height h_0 is chosen as the thickness of the canvas layer used in the experiments, which is 0.00026 m. We vary h_ℓ from h_0 to 0.001 m and plot τ_ℓ as a function of h_ℓ in Figure 4.4. The plot clearly shows that the lubrication timescale increases with this lubrication height, with rapid increase for initial height increments of h_ℓ. As h_ℓ becomes larger, the increase in τ_ℓ slows down, to the point where differences in h_ℓ have negligible effects on the timescale. This makes sense as F_ℓ weakens as the particle moves further away from the bed. For all further analysis in this section, we set h_ℓ equal to our experimental particle height $h_p = 0.00079$ m. We choose this value as it is measurable and is sufficiently far from the bed, where differences in τ_ℓ become negligible as shown in Figure 4.4 marked with a blue dot.

Using $h_\ell = h_p$, we next test how the lubrication timescale τ_ℓ varies with particle diameter d_p and particle density ρ_p. First, we vary d_p starting from an infinitely small particle up to the largest particle size used in our experiments, where $d_p = 0.01$ m. We plot τ_ℓ as a function of d_p in Figure 4.5. In this plot, we see that the lubrication timescale increases parabolically with particle diameter. As expected, a larger d_p results in a larger τ_ℓ because greater d_p increases the area of the particle where water needs to inflow, increasing the area the lubrication-induced suction pressure can act on. Next, we vary the particle density ρ_p from $700 - 1000$ kg/m^3 to assess the differences in particle buoyancy for a range relevant to microplastics. In Figure 4.6, we plot the lubrication timescale as a function of particle density, for a constant $d_p =$ 0.005 m. We see τ_ℓ increases with increasing ρ_p at an increasing rate as the particles

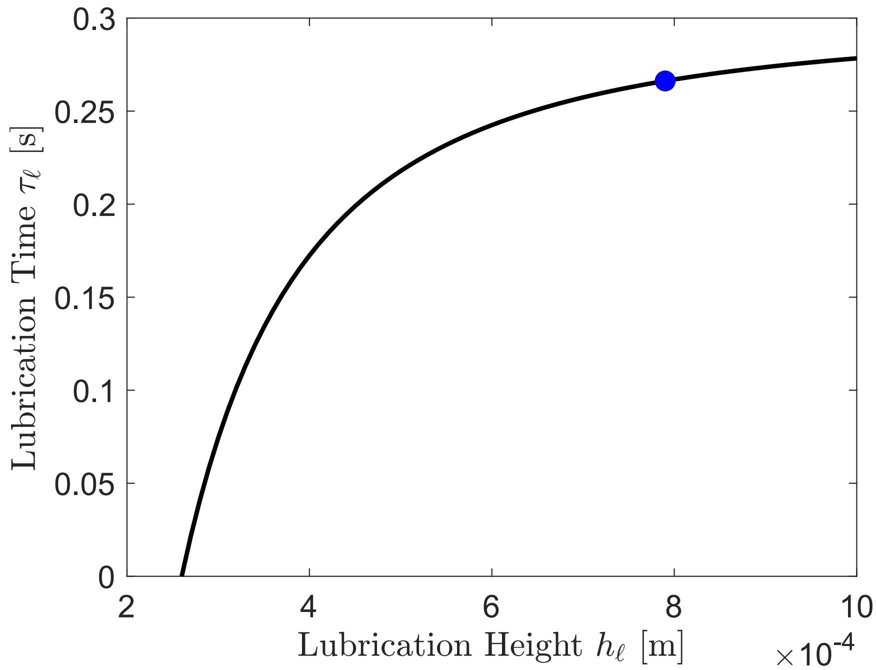

Figure 4.4: Lubrication timescale τ_ℓ plotted as a function of lubrication height h_ℓ, using Equation 4.20. Lubrication height is varied incrementally starting from h_0. The blue dot indicates when $h_\ell = h_p$. Particle diameter and density are held constant with values of 0.005 m and 970 kg/m^3, respectively.

approach the density of water. This is because lower density particles experience a strong buoyancy force, causing them to be removed from the bed more quickly compared to their higher density counterparts. Additionally, we see that τ_ℓ approaches infinity as $\rho_p \to \rho_f$. This is due to neutrally buoyant particles having no upward buoyancy force, which causes this timescale formulation to break down, thus this expression only applies to buoyant particles and modifications would be needed if applied to neutrally buoyant particles. In summary, we derived an expression for the lubrication timescale τ_ℓ which characterizes the time it takes for a flat particle initially on the bed to be lifted off the bed due to buoyancy. In the next subsection, we compare our estimate of τ_ℓ to the particle relaxation timescale τ_p.

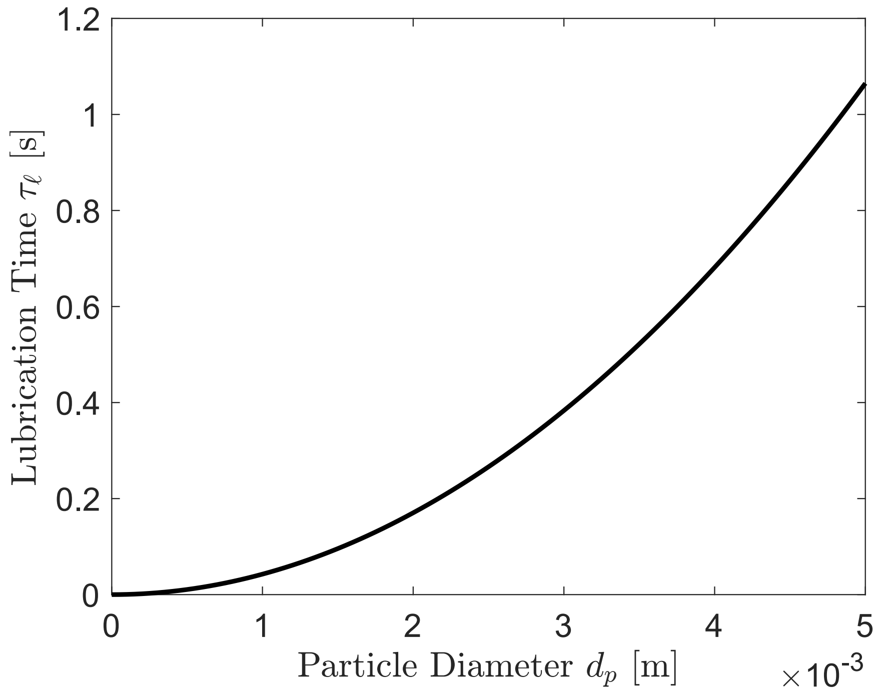

Figure 4.5: Lubrication timescale τ_ℓ plotted as a function of particle diameter d_p. Particle diameter is varied from .0001 m to .01 m. As stated, h_ℓ is set to 0.00079 m, and particle density is 970 kg/m^3.

4.4.2 Lubrication timescale vs. relaxation timescale

In this section, we compare τ_ℓ to the particle relaxation timescale τ_p used in the experiments (refer to Chapter 2 for experimental description). Choosing the appropriate particle timescale is important for these experiments, as it directly relates to the particle Stokes number St, which we found to be a key factor for determining particle beaching and beaching positions in the experiments. Both τ_ℓ and τ_p characterize resistant forces on the particle. While τ_ℓ characterizes the lubrication force which resists the particle's vertical motion, τ_p characterizes the drag force which resist's the particle's horizontal motion. Because buoyant particle pick-up in shallow swash flows is not a well-characterized system, it is not obvious which timescale is

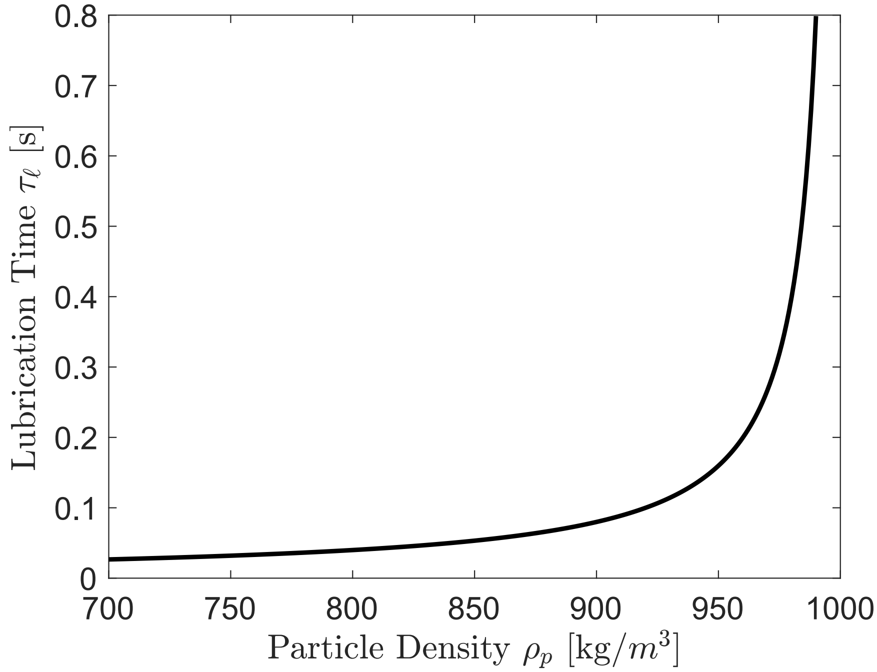

Figure 4.6: Lubrication timescale τ_ℓ plotted as a function of particle density ρ_p. Particle density is varied incrementally from 700 kg/m^3 to 1000 kg/m^3, which represents neutrally buoyant particles. Particle diameter is 0.005 m and h_ℓ is 0.00079 m.

the most appropriate. In this section, we will compare these two timescales in the context of our experimental results on particle transport.

While τ_ℓ depends on particle size, geometry, and density, it is not a function of the shoreline flow speed u_s, as we have derived it. In contrast, the relaxation time τ_p is a function of u_s and represents how quickly a particle can accelerate to the shoreline speed from rest, and is given by:

$$\tau_p = \frac{d_p^2(\rho_p/\rho_f + C_m)}{18\nu(1 + 0.15Re_p^{0.687})}, \tag{4.21}$$

where $Re_p = u_s d_p/\nu$ and $\gamma = \rho_p/\rho_w$ (see Chapter 2 for more details). Next, we compare these two separate timescales considering that one depends on the flow and one does not. To compare them, we derive a critical shoreline speed $u_{s,c}$, which is the speed when τ_ℓ is equal τ_p. This allows us to determine which timescale is shorter and which is longer for a given u_s. Specifically because $\tau_p \sim 1/u_s$, if $u_s > u_{s,c}$ then $\tau_p < \tau_\ell$. Thus, we expect that when the flow is fast, τ_p is the shorter timescale and drag is more relevant to incipient motion. In the limit where there is no flow and $u_s \to 0$, τ_ℓ will always be faster than τ_p, such that lubrication would be more relevant to characterizing initial motion. To derive $u_{s,c}$, we set $\tau_p = \tau_\ell$ and isolate the Reynolds number Re_p:

$$Re_p = \left(\frac{C-1}{0.15}\right)^{1/0.687}, \text{ where} \tag{4.22}$$

$$C = \frac{16 g h_p \rho_p(\rho_f - \rho_p)}{54\nu^2\rho_f^2}\left(\frac{1}{\frac{1}{h_0^2} - \frac{1}{h_p^2}}\right). \tag{4.23}$$

From these equations, we determine the critical shoreline speed as a function of particle size:

$$u_{s,c} = \frac{\nu}{d_p}\left(\frac{C-1}{0.15}\right)^{1/0.687}. \tag{4.24}$$

Using Equation 4.24, we plot the critical shoreline velocity $u_{s,c}$ as a function of particle diameter d_p in Figure 4.7. We see that $u_{s,c}$ increases as d_p decreases. This makes physical sense because smaller particles will have a shorter lubrication timescale, and consequently, to achieve an equally small relaxation time, a higher shoreline velocity is needed.

If there is no flow, the lubrication timescale will always be shorter than the relaxation timescale. However, for fluid velocities greater than 0.1 m/s, the lubrication timescale is longer than the relaxation timescale for particle diameters larger than 1 mm. This relation is due to the relaxation timescale scaling with $\sim d_p^2/Re_p^{0.687}$, which can be simplified to $d_p^{(n)}$, where n is roughly 1.313. Conversely, the lubrication timescale scales directly with d_p^2. Therefore if $\tau_\ell = \tau_p$, shoreline velocities must be small ($u_{s,c}$ on the order of $10^{-2} - 10^{-1}$ m/s). However, in our experimental swash zone, u_s values are an order of magnitude greater compared to the estimated $u_{s,c}$. In our experiments, shoreline velocities u_s are estimated at the point of initial wave impact. Shoreline speed values recorded in our experiments where particles are initialized range from $10^{-1} - 10^{0}$ m/s. Additionally, swash events in our experiments represent small run-ups on protected beaches, suggesting that u_s values on larger beaches are even higher. However, it should be noted that shoreline speeds approach zero at flow reversal, so lubrication timescales may be more comparable, or even shorter, than relaxation timescales at the highest part of the run-up. Overall, actual shoreline velocities are expected to typically be much faster compared to estimated $u_{s,c}$, leading to the conclusion that $\tau_p < \tau_\ell$ for many microplastics (< 5 mm) in typical swash zones.

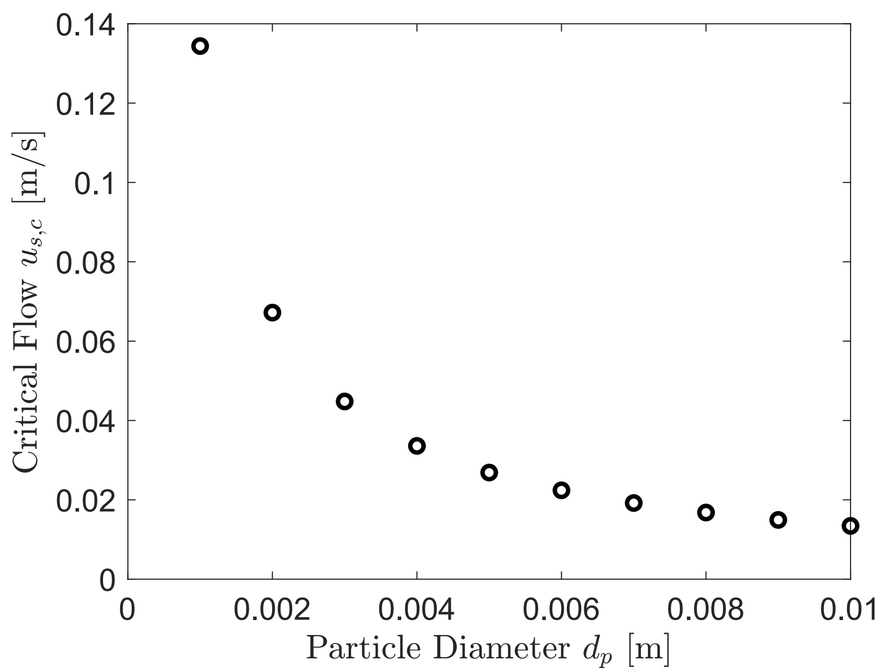

Figure 4.7: Critical shoreline velocity $u_{s,c}$ plotted as a function of particle diameter d_p, using Equation 4.24. Particle density is held constant at 970 kg/m^3, and h_ℓ is set to the particle height 0.00079 m.

4.4.3 Comparison to experiments

Finally, we evaluate τ_ℓ for the particles used in our experiments and compare it both to the predicted τ_p and the measured τ_{exp} characterizing the particle incipient motion. We plot τ_ℓ vs τ_p for each wave case and particle size combination in Figure 4.8. For a given combination, we find that the lubrication timescale is an order of magnitude greater than relaxation timescales. This means that the lubrication force may cause the particles to take a long time before they leave the bed and start being transported by the flow. From these estimated values of τ_p and τ_ℓ, we calculate a Stokes number for each timescale, i.e., $St_0 = \tau_p/\tau_f$ and $St_\ell = \tau_\ell/\tau_f$, where τ_f is the fluid timescale, calculated as u_s/g. In Figure 4.9, we plot the normalized final positions of particles on the beach (described in Chapter 2) as a function of both St_0 and St_ℓ. We observe a similar trend for both Stokes numbers: lower values of St lead to higher x_f/L. The data collapses slightly better with St_ℓ compared to St_0, however both plots are similar enough that it is not obvious which is most appropriate. Thus, to further compare the two timescales, we plot them directly against τ_{exp}.

We plot the t_{exp} values against the predicted values of both τ_p and τ_ℓ in Figure 4.10. In Figure 4.10a we see that the experimental timescale estimates are of a similar order of magnitude as the relaxation timescale estimates. Additionally, the two timescales show a good correlation; that is, higher t_{exp} corresponds with higher τ_p. There is some scatter and relatively large error bounds, but this is because of the slow frame rate of the camera which prohibited higher accuracy estimates. In contrast, Figure 4.10b does not reveal any significant trend, and we find t_{exp} values to be an order of magnitude less than the corresponding the τ_ℓ values.

Overall, our estimates of t_{exp} track much closer to the relaxation timescale than the estimated lubrication timescales, suggesting that the drag from the outer flow is more important to incipient motion in our experiments than the lubrication force (in the form we have derived). This also suggests that our lubrication timescale

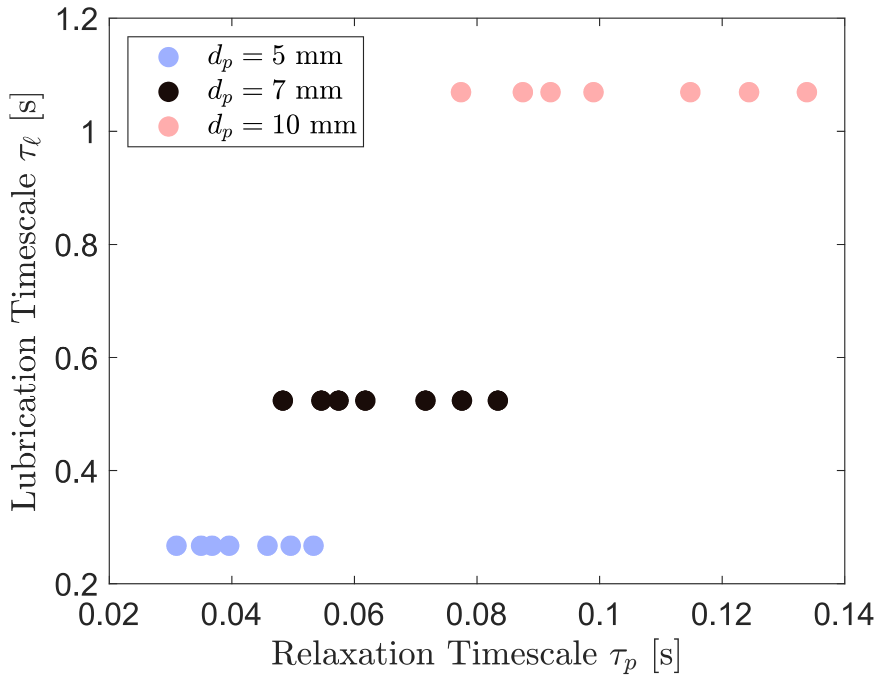

Figure 4.8: Lubrication timescale τ_ℓ plotted with the particle relaxation timescale τ_r. The legend entries indicate the varying particle diameters tested, which are the particle sizes used in previous experiments (Abarca et al., 2026).

derivation is not an accurate representation of the buoyant particle incipient motion in our experiment. Revisiting our assumptions in the derivation, it is likely that the assumption of purely vertical motion from the particle is inaccurate. Particles likely tilt off the beach at an angle. Previous derivations (Wang, 1977; Yih, 1974) show that the plates fall much faster at an angle, as opposed to flat. This means that the lubrication timescale for a rising particle will be much faster if it rises at an angle. Therefore, we suggest performing further analysis informed by a plate rotating off the surface(Yih, 1974). Yet, this analysis does bolster our confidence in τ_p being a relevant timescale to derive a Stokes number at initial wave impact.

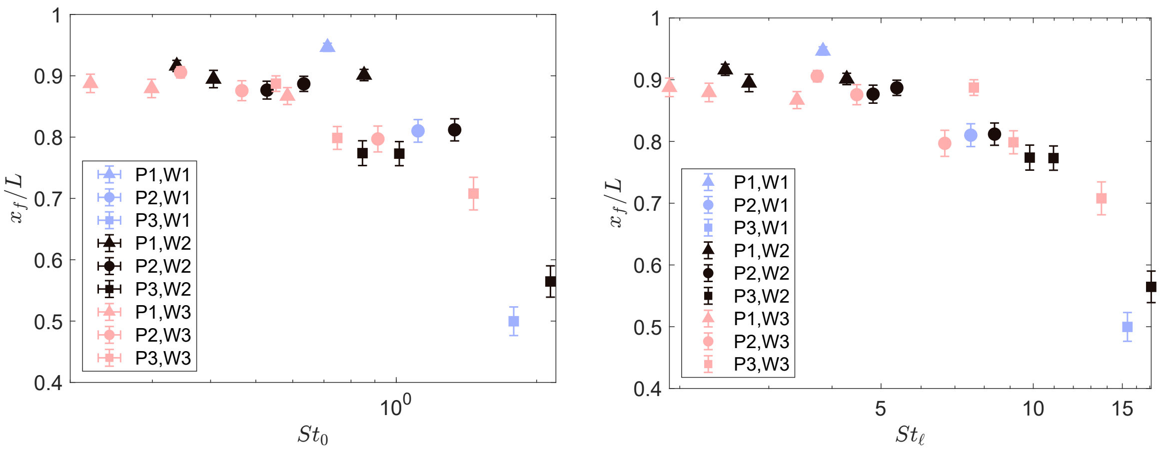

(a) (b)

Figure 4.9: Normalized particle final positions x_f/L plotted as a function of Stokes number. (a) is the Stokes number derived from τ_p, denoted as St_0. (b) is the Stokes number derived from τ_ℓ, denoted as St_ℓ. Legend entries indicate the particle and run-up lengths tested. Errorbars represent the standard error.

4.5 Conclusion & future work

In this chapter, we reviewed previous work on the incipient motion of negatively buoyant particles (i.e., sediment and heavy microplastics) in the swash zone. However, these concepts, including the Shield number, do not apply to the incipient motion of buoyant microplastics in this region. This is due to a differing balance of forces, such that forces that oppose motion do not prevent it, but rather only delay the initial motion of buoyant particles. We presented a method to characterize the incipient motion of buoyant particles by deriving a characteristic timescale using an appropriate force balance. Both lubrication and drag forces were identified as relevant forces to determine the timescale of incipient motion. Upon derivation, timescales due to lubrication and drag can differ depending on particle geometry, density, and local shoreline velocity. We compared these timescale derivations with experimental estimates, and

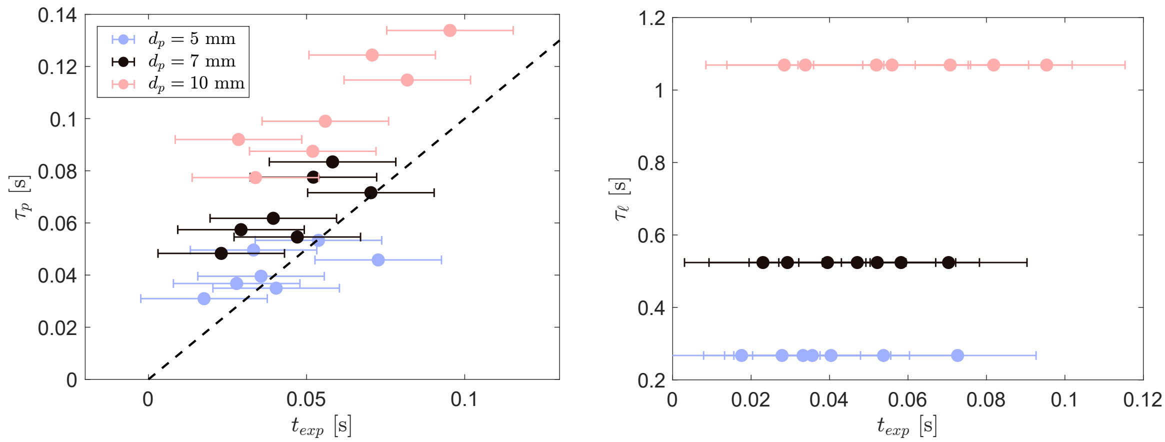

(a) (b)

Figure 4.10: (a) Particle relaxation time τ_p and (b) lubrication time τ_ℓ plotted with experimental timescales t_{exp}. Additionally in (a), a one-to-one line (–) plotted along side data points. Legend entries indicate the particle sizes. Errorbars represent the framerate of the recording camera.

found that the timescale for fluid drag best approximates the experimental timescales for buoyant particle incipient motion in the swash zone.

However, this does not meant the lubrication timescale is not relevant to the incipient motion. The lubrication timescale presented considers particles uniformly rising from the bed, but particles may rise asymmetrically off the bed. Therefore, we suggest future analysis to consider particles lifting at an angle, and could be informed by theory of a rotating plate on a surface. Additionally, the lubrication timescale is likely more relevant in regimes outside of our experimental study. In particular, particles that are near the highest parts of wave run-up experience slower shoreline velocities, as these velocities approach zero at flow reversal. Thus, we suggest future experimental work expand the range of experimental timescales for incipient motion. We recommend two main focuses: 1) experiments should clearly measure when and how (i.e., at an angle) particles lift off the beach, and 2) they should consider particles were flow speeds are low, as lubrication timescales may be more comparable to experimental values.

Chapter 5

CONCLUSIONS & FUTURE WORK

5.1 Conclusions

To combat increasing microplastic pollution, it is important to understand the transport of buoyant microplastics in the swash zone. Inherently, this is a complex area of research as transport is influenced by swash zone hydrodynamics, bed morphology, and particle parameters. Thus, the purpose of this work was to fill current gaps of knowledge involving small particle transport in the swash zone. Specifically, we focused on the identifying the physical mechanisms that dictate the probability of a particle remaining on the beach, and if so where. We consider beaches with small waves, characteristic of protected shorelines near urban areas which are exposed to high plastic pollution. To study this question, we simplified the system by studying the beaching of particles in an individual swash event on an impermeable beach. The first goal of this work was to study positions of particles after a swash event, using a small-scale experimental wave tank. The second goal was to extrapolate experimental results to multiple swash events, and subsequently model residence times of particles on the beach. The third goal was to investigate the incipient motion of buoyant particles in the swash zone, so to further identify and analyze the relevant forces for buoyant microplastic transport.

To address our first goal, we designed a small-scale wave tank where we recorded particle positions after individual swash events. First, we performed exploratory experiments on a sediment bed discussed in Appendix A. We found that final particle positions are influenced by particles sizes, run-up lengths, and particle initial positions. In Chapter 2, we expanded on exploratory experiments by characterizing the impact of initial conditions on final particle positions. These improved experiments utilize an impermeable bed, where buoyant particles are tracked during a swash event. We test 27 unique combinations of particle diameters, particle initial positions, and wave run-up length. We characterize the effect of these initial parameters by deriving a Stokes number St, or the particle's inertia relative to the fluid's inertia, at initial wave impact. In general, particles with low relative inertia were more likely to remain on the beach following a swash event compared to particles with relatively high inertia. This is due to low inertia particles closely following the swash bore front during uprush, thus resulting in these particles reaching higher points on the beach. In contrast, particles with high inertia tend to lag behind the swash bore front resulting in a higher probability of washing off the beach. Moreover, the high inertia particles that do remain on the beach tend to settle at lower positions on the slope compared to the low inertia particles. In summary, we find that the relative particle inertia at initial wave impact is deterministic of particle beaching during a swash event.

In Chapter 3, we address our second goal by developing a statistical model for particle beaching positions in the swash zone across multiple swash events. Rather than resolving the hydrodynamics, each model timestep corresponded to one swash event. The statistical model inputs included a wave run-up distribution to randomly select run-ups from, the number of run-ups to simulate, the number of particles, and particle size and density. Using these inputs, we derive a Stokes numbers to determine particle beaching likelihood and transport with probabilities empirically derived from our previous experiments. We conducted a number of simulations with varying input parameters to determine their impact on particle beaching positions and particle residence times on the beach. In general, particles that remained on the beach were quickly transported to higher positions on the beach. These high positions of accumulation served as a 'wrack' line, which is a function of the mean run-up length where the wrack is typically higher than L_{rms}. However, particles also continually left the beach during simulations, and we observed that particle counts on the beach decreased exponentially over time. Thus, we used an exponential fit to determine particle residence times on the beach. We found that residence times were largest for small particles and large run-ups. This was due to small particles in a large run-up corresponding to a small Stokes number, thus particles were more likely to reach high positions on the beach and remain there. Additionally, we found that residence time decreased with increasing Stokes number. Along with varying model inputs, we tested the impact of tides on simulation outputs. We found that particles were more likely to be stranded on the beach in a falling tide compared to a rising tide. This led to falling tides having a higher residence time when compared to both a rising tide and a no tides case. Furthermore, we found that the magnitude of tidal excursion also impacts particle count on the beach, such that large falling tides resulted in high residence times and large rising tides resulted in low residence times. In summary, we developed a statistical model based on the underlying physics of buoyant particle transport in the swash zone. This model was used to study the evolution of particle positions on a beach and their residence times under continuous wave forcing.

In Chapter 4, we addressed our third goal by both reviewing sediment transport literature and using an idealized analytical model to analyze the incipient motion of buoyant microplastics in the swash zone. We review how the Shields parameter is used to determine if sediment particles will move from the bed, and if so the critical shear stress that incites motion. However, we highlighted that a buoyant particle is always mobilized from the bed when submerged, thus there exists a characteristic timescale that describe how quickly a buoyant particle moves. First, we identified drag and lubrication as relevant forces, and derived timescales for each force. Similar to previous work, we determined the drag timescale to be the particle relaxation time. For lubrication, we derived a timescale from balancing the lubrication force with buoyancy, similar to the classic falling plate problem. Depending on the particle and flow parameters, the timescale of drag and lubrication can be quite different.

Therefore, we compared timescales of incipient from our experiments with derived force timescales. We found that the drag timescale, or particle relaxation time, best matched experimental values. In summary, the incipient motion of buoyant particles in the swash zone is characterized using a timescale derived from relevant forces acting on the particle.

5.2 Future work

In our experiments, we tested the effects of particle size, particle initial positions, and wave run-up length. However, we recommend future work to add complexity to the experiments by expanding the parameter space. In order to emulate microplastics on a real beach, we suggest considering particle shape, particle density, transport on a sediment bed, and swash wave-wave interactions. In our experiments, particle shape and density were held constant, but real microplastics can appear as pellets, fragments, or fibers with varying densities. Therefore, we suggest future work to derive Stokes numbers considering these additional parameters, and compare with results presented in Chapter 2. Regarding a sediment bed, we suggest tracking sediment motion along with microplastic transport. This would provide a direct comparison of sediment and microplastic motions, as well as characterize possible interactions. Finally, the addition of interactive swash events would mimic more of the complexity that can exist in real swash flows. While laboratory experiments will always be idealized when compared to field observations, using the techniques together will provide the best insights into particle transport on beaches.

Another realm of future work should focus on studying particles that leave the beach and their resulting transport. In our model, particles that are washed off are neglected for the remainder of simulations, as we do not have a reliable model to predict where they go in the surf zone. How they enter the surf zone (i.e., their position in the water column) likely controls how they re-enter the beach, and it is not obvious that particles entering the surf zone from offshore will have the same fate as particles which enter from the swash zone. We suggest future experiments that track the locations of particles that start on the beach after they are washed off. This work would improve our understanding of the transport of buoyant microplastics in the nearshore region.

Finally, we suggest further work on the incipient motion of buoyant microplastics in the swash. The goal of this future work should be to closely analyze the time and motion of buoyant particles beginning their transport. In Chapter 4, we noted that the derived lubrication timescale did not quite match our experimental timescale, but this does not mean that lubrication forces are not relevant. We recommend expanding the lubrication force analysis to consider particles which rise at an angle. Additionally, it is important to improve experimental measurements of the incipient motion timescale. Our current measurements are limited because of the challenges in imaging the particle at the moment of wave impact. Therefore, future work should improve techniques to track how the particles actually lift off the bed. Moreover, improved tracking can clarify the correct derivation for lubrication timescale by precisely characterizing the orientation of particles as they lift off the bed.

Appendix A

EXPLORATORY EXPERIMENTS ON A PERMEABLE BEACH

Prior to the main Chapters in this thesis, we present pilot experiments that we conducted to inform our study of buoyant microplastic transport in the swash zone. In general, the study of buoyant particle transport in the swash zone is complex, as it is difficult to isolate relevant parameters due to swash-swash interactions and particle initial conditions. Therefore, we design experiments where we aim to simplify the system by focusing on a single swash event and varying particle initial conditions. By using a single swash event, we can focus on the transport of a particle during each swash phase, i.e., if the particle follows the ballistic motion of the swash. Along with swash conditions, these experiments identify the importance of particle parameters, specifically particle size and particle initial position. The goal of these experiments is to determine how changing the initial conditions dictates the transport of a buoyant microplastic in the swash zone. In the following sections, we outline our experimental facility, methods, and results of these experiments.

A.1 Experimental facility

To isolate simple particle-swash interactions, we designed a wave tank to generate single swash events to observe the transport of positively buoyant particles in the swash. A schematic of the laboratory experimental facility is depicted in Figure A.1. The wave tank is 225 cm long, 30 cm wide, and 25 cm tall. It has a relatively narrow design to reduce alongshore variability, allowing us to focus on cross-shore forcing on the beach. In this setup, the cross-shore position is defined as x in our coordinate system, with $x = 0$ set at the mean water level. For these experiments, we used a permeable beach (slope or $\beta = .1$) made of coarse sand (with grain diameter $D_s \sim .75$mm). We wanted to capture the effects of permeability that may be seen on a real beach. However, our beach is an extreme example of permeability, given the large grain size (typical values range from $0.25 - .5$ mm) and low saturation. Waves in this facility are generated using a paddle wave maker, driven by a stepper motor.

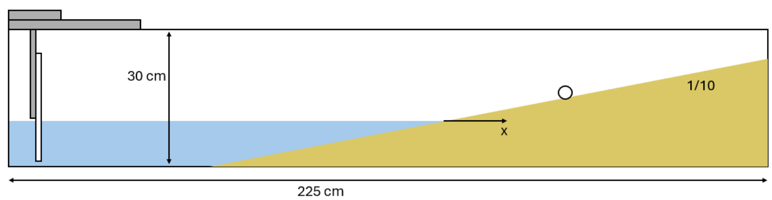

Figure A.1: Side view schematic of experimental wave tank equipped with wave paddle and permeable beach. Not to scale.

A.2 Experimental trials

We conducted experiments to characterize the transport of buoyant particles starting on the beach in an uprush-driven flow. Note that the uprush-driven flow is a result of the beach's high permeability, where the water in the swash is fully absorbed by the bed before backwash. We used two particle types from Cospheric: spheres and nurdles, which are small plastic pellets that are roughly spherical. Particle characteristics are listed in Table A.1. We attempted to use disks as well, but they were often buried by the sediment, so we decided not to include the data. We used two wave cases, which we labeled as "small" and "large", listed in Table A.2.

A typical experimental trial was as follows: Four particles were started on the beach aligned in the alongshore direction at initial position x_0, then a single wave was sent towards the beach, and once the water fully receded or was absorbed by the bed, we recorded the final positions of the particle x_f. We chose four evenly

Table A.1: Summary of particle parameters used in these experiments

	Small	Medium	Large
Shape	Sphere	Nurdle	Sphere
Density ρ_p (kg/m^3)	900	970	900
Diameter d_p (mm)	2.5	3.9	7.9

Table A.2: Wave parameters the two wave cases considered on the permeable beach. This data is recorded prior to experimental trials.

	Small	Large
Run-up L (m)	0.4	0.5
Wave height H (m)	0.015	.018
Initial Water depth (m)	.07	.10

spaced x_0 as a function wave run-up L for each wave case. Final positions x_f were hand-recorded from the side of the tank using a measuring tape. During each swash event, the beach was deformed due to the inevitable transport of sediment. To ensure consistency across our trials, we reshaped the beach before each run. For each initial position, wave, and particle, we ran 16 trials for a total of 64 data points for each set of initial conditions.

A.3 Results & *discussion*

First, we examine the final positions of particles as a function of their initial position. We present the data for the small and large waves in Figure A.2, as (a) and (b) respectively, using probability distribution functions (PDF) to show the results based on particle size. In both plots, we observe that the distributions are skewed with more particles at higher x_f/L. This suggests that particles, regardless of size, tend to beach high on the slope. If we compare particle sizes, we see that the spread of beaching positions correlates with particle size, such that the largest particles have the largest spread away from the top of wave run-up. When comparing across wave cases, distributions peak slightly lower on the slope in the large wave case compared to the small wave case, most notably for the large particles. This is likely due to the large wave case, which has a greater water depth compared to the small wave case, displaying a minimal backwash before fully being absorbed by the bed. Overall, we find that both the wave size and particle size influence the final beaching positions of the particles and their spread.

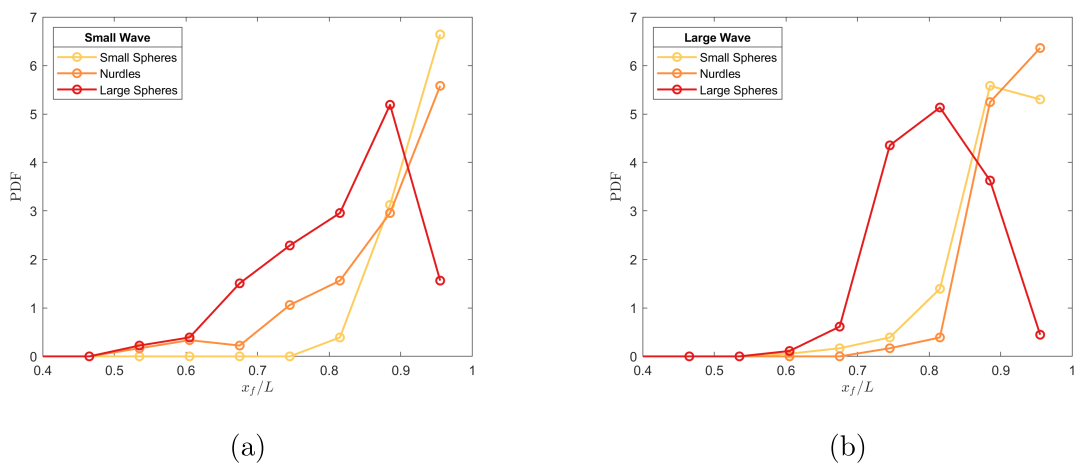

Figure A.2: Probability density functions (PDf) of normalized particle final position x_f/L for all particles and both the small wave (a) and large wave (b). These consider data from all initial positions.

To explore the spread further, we calculate the standard deviation of particle beaching positions σ_{x_f} for each x_0. In Figure A.3, we plot σ_{x_f}/L as a function of normalized initial position x_0/L, for both the small and large wave case. In the small wave case, we see a slight trend where the spread of beaching positions decreases as particles start higher on the slope, or higher x_0/L. Whereas in the large wave case, the spread is more consistent across all initial positions. However, in both wave cases, the smallest spread occurs at the highest x_0, which makes sense as these particles have less time to spread during uprush. Our data suggests initial position is important to the spread of the beaching position; thus, even though the particles and the flow are identical, the time at which they enter the flow causes their trajectories to diverge.

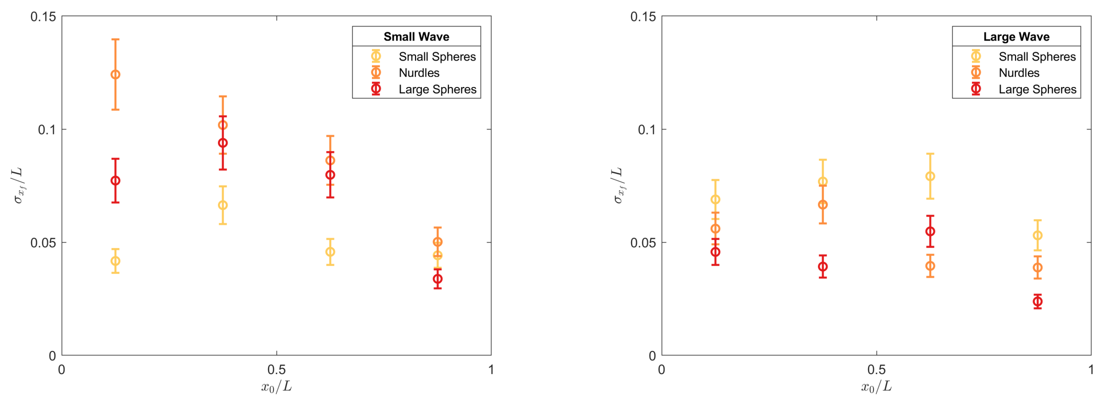

(a) (b)

Figure A.3: The standard deviation of particle beaching positions σ_{x_f} plotted as a function of normalized initial position x_0/L. (a) is the spread of all particles in the small wave, while (b) is the spread in the large wave. Errorbars indicate the standard error.

Finally, we consider the effects of the initial position on the mean particle beaching positions. We plot the dimensionless average final position x_f/L as a function of the dimensionless initial position x_0/L for each particle and wave case in Figure A.4. We also include a one-to-one line for reference, where points to the left of the line represent particles that beach higher than where they started, whereas points on the line do not move from their initial position. In the small wave case, we see x_f increases with increasing x_0, and notably, the smallest particles reach the highest x_f. In the large wave case, we find no clear trend, but the differences between particle sizes are similar to those in the small wave case, where small and medium particles have higher x_f than large particles. In both wave cases, we find particles that start at the highest x_0 are most likely to have x_f close to the one-to-one line. We believe this is likely because of two effects: 1) the particles having little room to travel in uprush, and 2) the flow being so shallow near maximum run-up that the particles barely move from their initial positions.

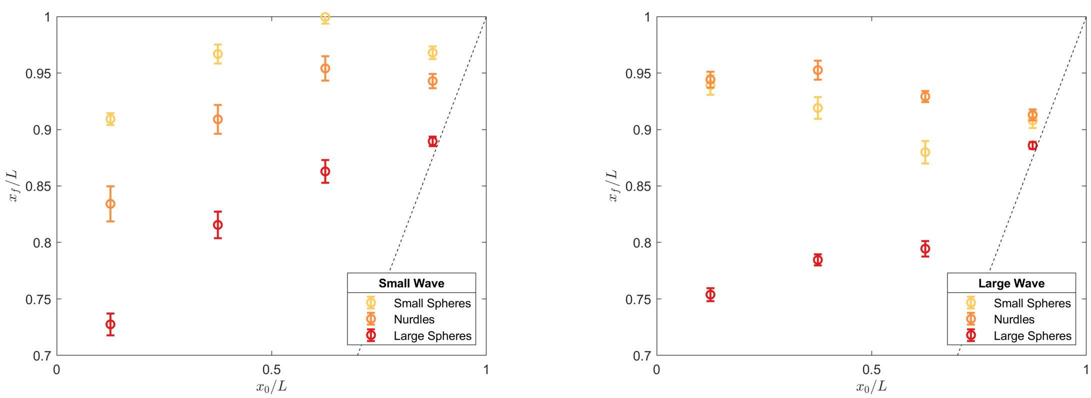

(a) (b)

Figure A.4: The average normalized final position x_f/L as a function of the normalized initial position x_0/L for each particle and wave case. Errorbars indicate the standard error.

Our results indicate that the wave case, particle size, and particle initial position are all important to the particles' final beaching positions. Notably, we observe that small particles travel farthest in this uprush-driven swash flow which suggests that they may follow close to the swash bore front. We hypothesize that this is due to small particles responding to the surrounding flow quicker than large particles. However, in these experiments, it is difficult to validate the particles' response time since we do not track the particles during the swash event due to instrumental limitations and the motion of sediment. Moreover, the experimental sediment bed minimized backwash, and therefore the experiment is not representative of beaches with smaller grains. Thus, these results provide insight to particle transport on the beach, motivating the more careful experiments we present in the Chapter 2.

Appendix B

EXPERIMENTAL SWASH FLOW COMPARISON WITH FIELD SCALE

To compare our experimental swash flows to a field-scale swash event, we use run-up data from Stockdon et al. (2006) given that it is a well-established reference swash dataset in the literature. This data set represents large run-ups, compared to those used in the experiments; therefore, we ask whether the small-scale experimental flow can represent the uppermost portion of the large field-scale flow. The specific data we use is from a beach with a similar slope ($\beta = 0.11$) (Stockdon et al., 2006); the observations report a maximum run-up measurement of $L = 13.9$ m. For the modeling, we use $f = 0.007$ for a sandy beach based on the average from Puleo and Holland (2001), and from these values we estimate $U_s = 6.78$ m/s using the Hughes and Baldock (2004) model. Plotting the modeled swash velocity for the reference cycle in Figure B.1a, we see that the experimental data all roughly follow the simulated swash data, showing how the swash shoreline velocity can be self-similar across varying run-up lengths. Furthermore, we plot the water depth, as we did in Chapter 2, of the field scale swash in Figure B.1b. As expected, we see that the field swash is much deeper compared to our experimental setup. Although real swash flows will likely deviate from this simple model, the swash model used here predicts self-similarity across run-ups for shoreline velocity. This suggests that a small scale lab flow can capture some of the physics of the uppermost portion of a large scale flow. This is especially relevant for studying the dynamics near the wrack line.

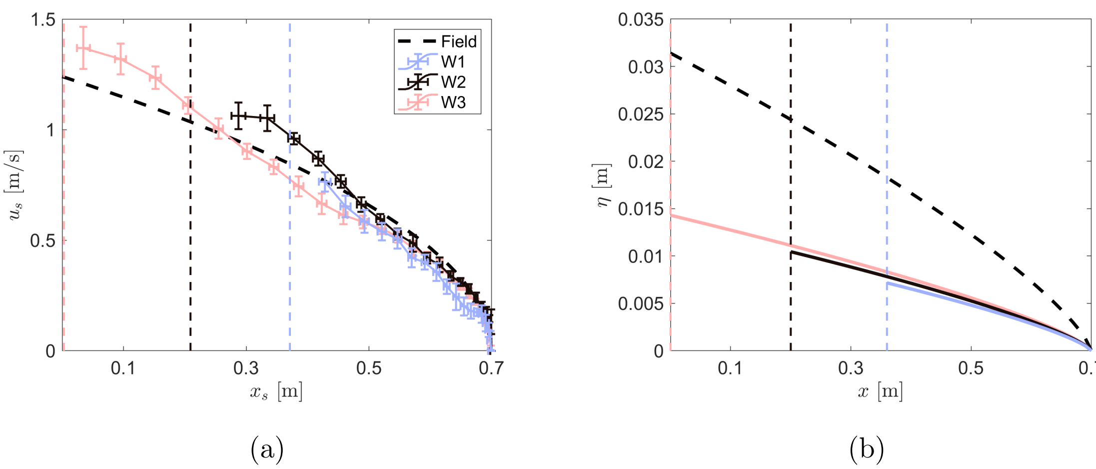

Figure B.1: Modeled field scale and experimental data comparison for (a) shoreline velocity and (b) water depth plotted against shoreline position. The modeled field example is shown by the black (–) line. The vertical dashed lines represent the reference mean water line ($x = 0$) for each experimental wave case. Errorbars indicate the standard deviation.

Appendix C
MODEL SENSITIVITY ANALYSIS

In Section 3.2.3, we plot beaching probabilities as a function of Stokes number, shown in Figure C.1. However, there is uncertainty in our model fit, especially for the intermediate Stokes regime $1 < St \leq 2$. While we emphasize that our model is flexible to the addition of new data, we want to test the sensitivity of the current beaching probabilities used in our model. First, we define our test cases across our 3 regimes. In the regime of $St \leq 1$, the probabilities were set at a constant 0.99, as experiments suggest particles are essentially guaranteed to remain on the beach. To test model sensitivity to this choice, we lower the value of this regime to 0.95. In our intermediate Stokes regime, we identify that the beaching probability decreases linearly with increasing St. We justify this choice physically in Section 3.2.3, but there is uncertainty of the fit in the regime. To test the sensitivity in this regime, we alter the equation such that we either increase or decrease the slope while maintaining the same value at $St = 1$. In our third regime of $St > 2$, we originally set a value of 0.95 because many particles within this regime remained at their original positions. However, there is uncertainty in this constant value, therefore we test this regime with a constant of 0.9 and 0.99. Using beaching probability variations, we identify the effects on model outputs. Note that p_{beach} variations are tested individually, which means we only alter one regime at a time while the other two regimes are consistent with Equation 3.10.

Median positions of the particles on the beach do not change with changing p_{beach}. While it may change particle count, the particles that remain on the beach maintain the same behavior for given St, described in Section 3.2.3. Therefore, we focus on the

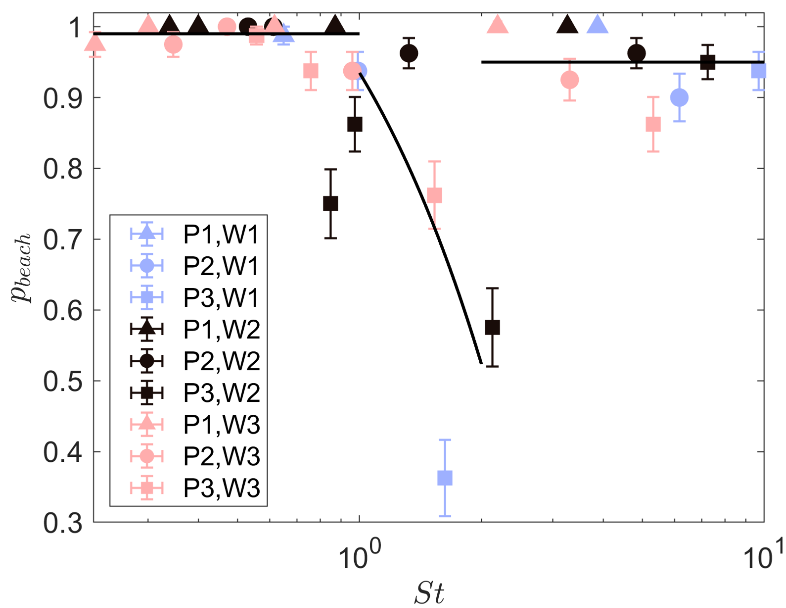

Figure C.1: Experimental and modeled beaching probabilities as a function of Stokes number, containing particles with $St > 2$. Legend entries indicate experimental data. Modeled probabilities from Equation 3.10 (-).

residence times τ_r for particle on the beach. To find τ_r, we look at the count density of particles on the beach as a function for all p_{beach} variations. In Figure C.2a, we show the variation for the regime of $St > 1$. We see that the count density of particles on the beach over time sharply decreases, and equivocally residence times decrease, when we lower p_{beach} for $St \leq 1$. In general, $St > 1$ is a common Stokes value in our simulations due to the relative size of run-ups (> 1 m) to particles (< 0.005 m), therefore decreasing p_{beach} should majorly change residence times. Next in Figure C.2b, we plot the count densities over time while varying p_{beach} for $1 < St \leq 2$. Here we find that increasing/steepening the slope of the fit slightly decreases particle count density and τ_r. In contrast, decreasing/softening the slope increases particle count density and τ_r. This makes sense as decreasing the slope increases the overall p_{beach}

in this regime, as higher St values less likely to leave the beach. Finally, we look at the count densities with varying p_{beach} for $St > 2$ in Figure C.2c. As expected, this figure shows that the residence times increase with increasing p_{beach} and decrease with decreasing p_{beach}. These trends are similar to those seen across p_{beach} variations. Overall, we find that the particle count density exponentially decreases over time for all test cases, although count density values and residence times vary with varying p_{beach}. Residence time values are most sensitive to p_{beach} changes for $St \leq 1$, as this is a common Stokes regime given the small particles. However, our previous experimental data suggests that 0.99 of particle beaching is a good approximation for this regime.

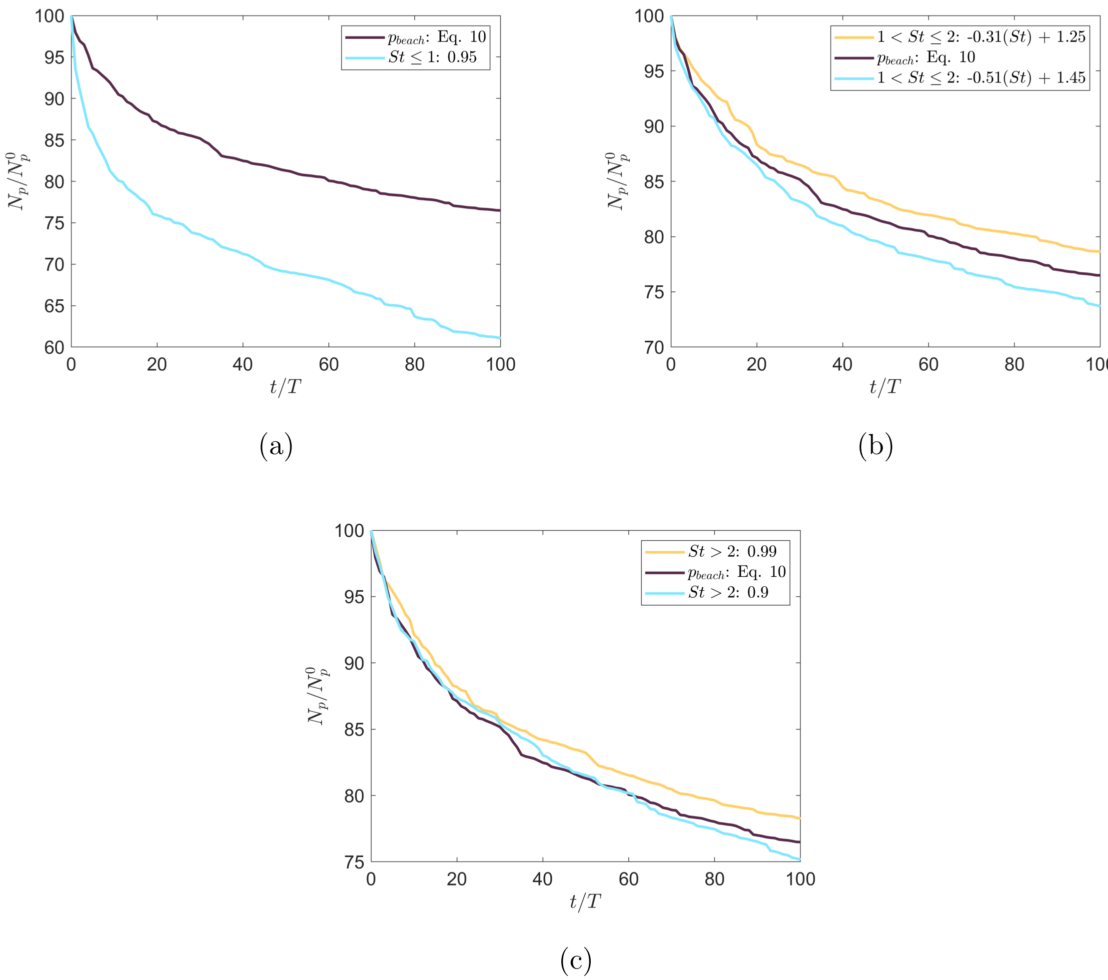

Figure C.2: The average particle count on the beach as a function of time, with varying p_{beach} for (a) $St \leq 1$, (b) $1 < St \leq 2$, (c) $St > 2$. Legened entries indicate p_{beach} values. Each line is averaged across 300 simulations.

Appendix D

MATLAB CODE FOR STATISTICAL MODEL IMPLEMENTATION

The codes used to produce the model were written and run in MATLAB. They are available online, along with a README, at the Github Repository: https://github.com/DiBenedettoLab/Statistical-Swash-Model

Appendix E

SCALING OF LIFT WITH BUOYANCY

In Chapter 4, we suggest that the lift force F_L is weak compared to the buoyancy force F_B. Here we present a scaling analysis comparing the two forces. For this comparison, we consider the scenario of a submerged disk rising symmetrically off of a flat bed in a swash flow, shown in Figure E.1. The lift force is defined as a function of the local flow speed such that:

$$F_L = \frac{1}{2}\rho_f U^2 A C_L, \tag{E.1}$$

where U is the flow speed and C_L represents the coefficient of lift. Then, we compare the lift with buoyancy force F_B of the particle:

$$\frac{F_L}{F_B} = \frac{\frac{1}{2}\rho_f U^2 A C_L}{(\rho_f - \rho_p) g V_p}, \tag{E.2}$$

where V_p is the submerged volume. Since we assume the particle to be fully submerged, V_p is simplified to Ah_p, where h_p is the particle height. Therefore, Equation E.2 reduces to:

$$\frac{F_L}{F_B} = \frac{\rho_f}{2h_p(\rho_f - \rho_p)} U^2 C_L. \tag{E.3}$$

Therefore, we see that the ratio of forces depends on how buoyant the particle is and how fast the flow is. In a swash flow, U decelerates over time, so the lift force should be least important near the top of the run up. Moreover, if the particle is flat and parallel to the flow, there would be a small pressure difference above and below the particle which means a small C_L. In summary, we expect the lift force to be smaller than buoyancy for particles with a larger density difference in slower flows with low lift coefficients.

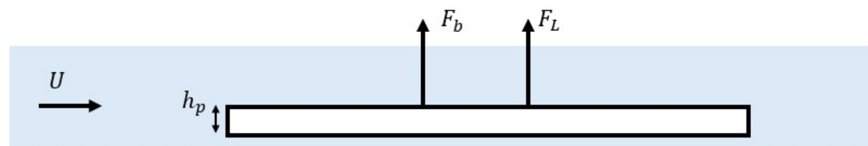

Figure E.1: Schematic of upward forces acting on a buoyant disk in the swash zone. Note: not to scale.

BIBLIOGRAPHY

Abarca, Carlos A, Tong Ling, and Michelle H Dibenedetto (2026). “Buoyant particle transport in a model swash flow”. *In Review*.

Alsina, Jose M., Silvia Falchetti, and Tom E. Baldock (May 2009). “Measurements and modelling of the advection of suspended sediment in the swash zone by solitary waves”. *Coastal Engineering* 56.5-6, pp. 621–631. DOI: 10.1016/j.coastaleng.2009.01.007.

Alsina, José M. and Iván Cáceres (Aug. 2011). “Sediment suspension events in the inner surf and swash zone. Measurements in large-scale and high-energy wave conditions”. *Coastal Engineering* 58.8, pp. 657–670. DOI: 10.1016/j.coastaleng.2011.03.002.

Baldock, T. E., R. Grayson, et al. (2014). “Flow convergence at the tip and edges of a viscous swash front - Experimental and analytical modeling”. *Coastal Engineering* 88, pp. 123–130. DOI: 10.1016/j.coastaleng.2014.02.008.

Baldock, Tom E. and Patrick Holmes (1997). “Swash Hydrodynamics on a Steep Beach”. *Coastal Dynamics - Proceedings of the International Conference*, pp. 784–793.

Barnes, David K.A., Francois Galgani, et al. (July 2009). “Accumulation and fragmentation of plastic debris in global environments”. *Philosophical Transactions of the Royal Society B: Biological Sciences* 364.1526, pp. 1985–1998. DOI: 10.1098/rstb.2008.0205.

Barnes, M. P., T. O’Donoghue, et al. (Aug. 2009). “Direct bed shear stress measurements in bore-driven swash”. *Coastal Engineering* 56.8, pp. 853–867. DOI: 10.1016/j.coastaleng.2009.04.004.

Battisti, Corrado et al. (June 2020). "Giant Reed (Arundo donax) wrack as sink for plastic beach litter: First evidence and implication". *Marine Pollution Bulletin* 155. DOI: 10.1016/j.marpolbul.2020.111179.

Battjes, Jurjen A (1971). "Run-up Distributions of Waves Breaking on Slopes". *Journal of the Waterways, Harbors, and Costal Engineering Division*.

Borrelle, Stephanie B et al. (2020). "Predicted growth in plastic waste exceeds efforts to mitigate plastic pollution". *Science*.

Bosboom, Judith and Marcel J.F. Stive (Jan. 2023). *Coastal dynamics*. TU Delft, pp. 1–580. DOI: 10.5074/T.2021.001.

Brocchini, M. and T. E. Baldock (Sept. 2008). "Recent advances in modeling swash zone dynamics: Influence of surf-swash interaction on nearshore hydrodynamics and morphodynamics". *Reviews of Geophysics* 46.3. DOI: 10.1029/2006RG000215.

Buffington, John M (1999). "The Legend of A. F. Shields". *Journal of Hydraulic Engineering*.

Butt, Tony et al. (2004). "The influence of bore turbulence on sediment transport in the swash and inner surf zones". *Continental Shelf Research* 24.7-8, pp. 757–771. DOI: 10.1016/J.CSR.2004.02.002.

Cesarini, Giulia et al. (Oct. 2021). "Is the weight of plastic litter correlated with vegetal wrack? A case study from a Central Italian beach". *Marine Pollution Bulletin* 171. DOI: 10.1016/j.marpolbul.2021.112794.

Chardón-Maldonado, Patricia, José Carlos Pintado-Patiño, and Jack A. Puleo (Sept. 2016). "Advances in swash-zone research: Small-scale hydrodynamic and sediment transport processes". *Coastal Engineering* 115, pp. 8–25. DOI: 10.1016/j.coastaleng.2015.10.008.

Chassignet, Eric P., Xiaobiao Xu, and Olmo Zavala-Romero (Apr. 2021). "Tracking Marine Litter With a Global Ocean Model: Where Does It Go? Where Does It Come From?" *Frontiers in Marine Science* 8. DOI: 10.3389/fmars.2021.667591.

Chubarenko, I., A. Bagaev, et al. (July 2016). “On some physical and dynamical properties of microplastic particles in marine environment”. *Marine Pollution Bulletin* 108.1-2, pp. 105–112. DOI: 10.1016/j.marpolbul.2016.04.048.

Chubarenko, I. P., E. E. Esiukova, et al. (July 2018). “Three-dimensional distribution of anthropogenic microparticles in the body of sandy beaches”. *Science of the Total Environment* 628-629, pp. 1340–1351. DOI: 10.1016/j.scitotenv.2018.02.167.

Chubarenko, Irina, Polina Krivoshlyk, et al. (Nov. 2024). “Natural sorting of sediments in the wave run-up zone works for microplastics as well”. *Marine Pollution Bulletin* 208. DOI: 10.1016/j.marpolbul.2024.117060.

Clift, Roland, John Grace, and Martin E. Weber (2005). *Bubbles, Drops, and Particles.*

Conley, Daniel C. and John G. Griffin (Mar. 2004). “Direct measurements of bed stress under swash in the field”. *Journal of Geophysical Research: Oceans* 109.3. DOI: 10.1029/2003jc001899.

Corcoran, Patricia L. et al. (Dec. 2020). “A comprehensive investigation of industrial plastic pellets on beaches across the Laurentian Great Lakes and the factors governing their distribution”. *Science of the Total Environment* 747. DOI: 10.1016/j.scitotenv.2020.141227.

Cowger, Win et al. (May 2021). “Concentration Depth Profiles of Microplastic Particles in River Flow and Implications for Surface Sampling”. *Environmental Science and Technology* 55.9, pp. 6032–6041. DOI: 10.1021/acs.est.1c01768.

Critchell, Kay and Jonathan Lambrechts (Mar. 2016). “Modelling accumulation of marine plastics in the coastal zone; what are the dominant physical processes?” *Estuarine, Coastal and Shelf Science* 171, pp. 111–122. DOI: 10.1016/j.ecss.2016.01.036.

Davidson, Benjamin, Jamie Brenner, and Nimish Pujara (Nov. 2023). “Beaching model for buoyant marine debris in bore-driven swash”. *Flow* 3. DOI: 10.1017/flo.2023.31.

Efimova, Irina et al. (Sept. 2018). “Secondary Microplastics Generation in the Sea Swash Zone With Coarse Bottom Sediments: Laboratory Experiments”. *Frontiers in Marine Science* 0.SEP, p. 313. DOI: 10.3389/FMARS.2018.00313.

Esiukova, E. et al. (Mar. 2026). “The fate of marine microplastics in the swash zone”. *Marine Pollution Bulletin* 224. DOI: 10.1016/j.marpolbul.2025.119100.

Forsberg, Pernille Louise et al. (Apr. 2020). “Behaviour of plastic litter in nearshore waters: First insights from wind and wave laboratory experiments”. *Marine Pollution Bulletin* 153, p. 111023. DOI: 10.1016/J.MARPOLBUL.2020.111023.

Geyer, Roland, Jenna R Jambeck, and Kara Lavender Law (2017). “Production, use, and fate of all plastics ever made”.

Goral, Koray Deniz et al. (June 2023). “Shields Diagram and the Incipient Motion of Microplastic Particles”. *Environmental Science and Technology* 57.25, pp. 9362–9375. DOI: 10.1021/acs.est.3c02027.

Guard, P. A. and T. E. Baldock (Apr. 2007). “The influence of seaward boundary conditions on swash zone hydrodynamics”. *Coastal Engineering* 54.4, pp. 321–331. DOI: 10.1016/j.coastaleng.2006.10.004.

Guerrero-Meseguer, Laura, Puri Veiga, and Marcos Rubal (Dec. 2020). “Spatio-temporal variability of anthropogenic and natural wrack accumulations along the driftline: Marine litter overcomes wrack in the northern sandy beaches of Portugal”. *Journal of Marine Science and Engineering* 8.12, pp. 1–15. DOI: 10.3390/jmse8120966.

Guler, Hasan Gokhan et al. (Aug. 2022). “Experimental study of non-buoyant microplastic transport beneath breaking irregular waves on a live sediment bed”. *Marine Pollution Bulletin* 181, p. 113902. DOI: 10.1016/j.marpolbul.2022.113902.

Hinata, Hirofumi, Keita Mori, et al. (2017). “An estimation of the average residence times and onshore-offshore diffusivities of beached microplastics based on the population decay of tagged meso- and macrolitter”. *Marine Pollution Bulletin* 122.1-2, pp. 17–26. DOI: 10.1016/j.marpolbul.2017.05.012.

Hinata, Hirofumi, Nao Sagawa, et al. (Mar. 2020). “Numerical modeling of the beach process of marine plastics: A probabilistic and diagnostic approach with a particle tracking method”. *Marine Pollution Bulletin* 152. DOI: 10.1016/j.marpolbul.2020.110910.

Hughes, Michael G (1995). “Friction Factors for Wave Uprush”. *Source: Journal of Coastal Research* 11.4, pp. 1089–1098.

Hughes, Michael G. and Tom E. Baldock (Aug. 2004). “Eulerian flow velocities in the swash zone: Field data and model predictions”. *Journal of Geophysical Research: Oceans* 109.8. DOI: 10.1029/2003JC002213.

Hughes, Michael G. and Adrienne S. Moseley (Sept. 2007). “Hydrokinematic regions within the swash zone”. *Continental Shelf Research* 27.15, pp. 2000–2013. DOI: 10.1016/j.csr.2007.04.005.

Isobe, Atsuhiko et al. (Dec. 2014). “Selective transport of microplastics and mesoplastics by drifting in coastal waters”. *Marine Pollution Bulletin* 89.1-2, pp. 324–330. DOI: 10.1016/J.MARPOLBUL.2014.09.041.

Jambeck, Jenna R et al. (May 2015). “Plastic waste inputs from land into the ocean”. *Science* 347.6223, pp. 768–771. DOI: 10.1126/science.1260879.

Kataoka, Tomoya, Hirofumi Hinata, and Shigeru Kato (2013). “Analysis of a beach as a time-invariant linear input/output system of marine litter”. *Marine Pollution Bulletin* 77.1-2, pp. 266–273. DOI: 10.1016/j.marpolbul.2013.09.049.

— (2015). “Backwash process of marine macroplastics from a beach by nearshore currents around a submerged breakwater”. *Marine Pollution Bulletin* 101.2, pp. 539–548. DOI: 10.1016/j.marpolbul.2015.10.060.

Kerpen, Nils B. et al. (Nov. 2020). “Wave-Induced Distribution of Microplastic in the Surf Zone”. *Frontiers in Marine Science* 7. DOI: 10.3389/fmars.2020.590565.

Kikkert, G. A. et al. (Feb. 2012). “Experimental study of bore-driven swash hydrodynamics on impermeable rough slopes”. *Coastal Engineering* 60.1, pp. 149–166. DOI: 10.1016/j.coastaleng.2011.09.006.

Kim, Yeulwoo et al. (Feb. 2017). "Large eddy simulation of dam-break-driven swash on a rough-planar beach". *Journal of Geophysical Research: Oceans* 122.2, pp. 1274–1296. DOI: 10.1002/2016JC012366.

Kramer, Matthias (Sept. 2025). "Surface Detachment and Bed Entrainment of Fluvial Plastics". *Water Resources Research* 61.9. DOI: 10.1029/2025WR040088.

Lanckriet, Thijs and Jack Puleo (2013). "Near-bed turbulence dissipation measurements in the inner surf and swash zone". *J. Geophys. Res. Oceans* 118, pp. 6634–6647. DOI: 10.1002/2013JC009251.

Landrigan, Philip J. et al. (2020). "Human health and ocean pollution". *Annals of Global Health* 86.1, pp. 1–64. DOI: 10.5334/aogh.2831.

Larsen, Bjarke Eltard et al. (Feb. 2023). "Experimental investigation on the nearshore transport of buoyant microplastic particles". *Marine Pollution Bulletin* 187. DOI: 10.1016/j.marpolbul.2023.114610.

Lebreton, Laurent C.M. et al. (June 2017). "River plastic emissions to the world's oceans". *Nature Communications* 8. DOI: 10.1038/ncomms15611.

Masselink, Gerhard, Darren Evans, et al. (Apr. 2005). "Suspended sediment transport in the swash zone of a dissipative beach". *Marine Geology* 216.3, pp. 169–189. DOI: 10.1016/j.margeo.2005.02.017.

Masselink, Gerhard and Jack A. Puleo (Apr. 2006). "Swash-zone morphodynamics". *Continental Shelf Research* 26.5, pp. 661–680. DOI: 10.1016/j.csr.2006.01.015.

Maxey, Martin R. and James J. Riley (1983). "Equation of motion for a small rigid sphere in a nonuniform flow". *Physics of Fluids* 26.4, pp. 883–889. DOI: 10.1063/1.864230.

Mørk, Jenny M. et al. (Jan. 2026). "A Lagrangian model of wave-induced beaching and resuspension of plastic particles". *Marine Pollution Bulletin* 222. DOI: 10.1016/j.marpolbul.2025.118718.

Nielsen, Peter and David J Hanslow (1991). "Wave Runup Distributions on Natural Beaches". *Source: Journal of Coastal Research* 7.4, pp. 1139–1152.

Núñez, Paula et al. (Feb. 2023). "Wave-induced cross-shore distribution of different densities, shapes, and sizes of plastic debris in coastal environments: A laboratory experiment". *Marine Pollution Bulletin* 187. DOI: 10.1016/j.marpolbul.2022.114561.

O'Donoghue, T., D. Pokrajac, and L. J. Hondebrink (May 2010). "Laboratory and numerical study of dambreak-generated swash on impermeable slopes". *Coastal Engineering* 57.5, pp. 513–530. DOI: 10.1016/J.COASTALENG.2009.12.007.

Onink, Victor et al. (June 2021). "Global simulations of marine plastic transport show plastic trapping in coastal zones". *Environmental Research Letters* 16.6, p. 064053. DOI: 10.1088/1748-9326/ABECBD.

Peregrine, D H (1983). "Breaking Waves on Beaches". *Ann. Rev. Fluid Mech* 15, pp. 149–78.

Pujara, Nimish, Philip L.F. Liu, and Harry Yeh (Aug. 2015). "The swash of solitary waves on a plane beach: Flow evolution, bed shear stress and run-up". *Journal of Fluid Mechanics* 779, pp. 556–597. DOI: 10.1017/jfm.2015.435.

Puleo, J A, R A Beach, et al. (2000). "Swash zone sediment suspension and transport and the importance of bore-generated turbulence". *JOURNAL OF GEOPHYSICAL RESEARCH* 105.C7, pp. 21–38. DOI: 10.1029/2000JC900024.

Puleo, Jack A and K Todd Holland (2001). *Estimating swash zone friction coefficients on a sandy beach*. Tech. rep., pp. 25–40.

Puleo, Jack A., Chris Blenkinsopp, et al. (Jan. 2014). "Comprehensive Field Study of Swash-Zone Processes. I: Experimental Design with Examples of Hydrodynamic and Sediment Transport Measurements". *Journal of Waterway, Port, Coastal, and Ocean Engineering* 140.1, pp. 14–28. DOI: 10.1061/(asce)ww.1943-5460.0000210.

Puleo, Jack A., Thijs Lanckriet, et al. (June 2015). "Sediment transport partitioning in the swash zone of a large-scale laboratory beach". *Coastal Engineering* 113, pp. 73–87. DOI: 10.1016/j.coastaleng.2015.11.001.

Rey, Savannah Franklin, Janet Franklin, and Sergio J. Rey (Feb. 2021). “Microplastic pollution on island beaches, Oahu, Hawai‘i”. *PLoS ONE* 16.2 February. DOI: 10.1371/journal.pone.0247224.

Ruju, Andrea et al. (June 2016). “Sediment transport dynamics in the swash zone under large-scale laboratory conditions”. *Continental Shelf Research* 120, pp. 1–13. DOI: 10.1016/j.csr.2016.03.015.

Sebille, Erik van et al. (May 2020). “The physical oceanography of the transport of floating marine debris”. *Environmental Research Letters* 15.2, p. 23003. DOI: 10.1088/1748-9326/AB6D7D.

Selim Yalin, By M and Emin Karahan (1979). “Inception of Sediment Transport”. *Journal of the Hydraulics Division*.

Shen, M. C. and R. E. Meyer (1963). “Climb of a bore on a beach Part 3. Run-up”. *Journal of Fluid Mechanics* 16.1, pp. 113–125. DOI: 10.1017/S0022112063000628.

Shields, A. (1936). “Application of similarity principles and turbulence research to bed-load movement”. *Hydrodynamics Laboratory Publ.*

Steenhauer, K. et al. (2011). “Subsurface processes generated by bore-driven swash on coarse-grained beaches”. *Journal of Geophysical Research: Oceans* 116.4. DOI: 10.1029/2010JC006789.

Stockdon, Hilary F. et al. (May 2006). “Empirical parameterization of setup, swash, and runup”. *Coastal Engineering* 53.7, pp. 573–588. DOI: 10.1016/j.coastaleng.2005.12.005.

Thornton, Laura and Nancy L Jackson (1998). “Spatial and Temporal Variations in Debris Accumulation and Composition on an Estuarine Shoreline, Cliffwood Beach, New Jersey, USA”. *Marine Pollution Bulletin* 36.9, pp. 705–711.

Vianello, A. et al. (Sept. 2013). “Microplastic particles in sediments of Lagoon of Venice, Italy: First observations on occurrence, spatial patterns and identification”. *Estuarine, Coastal and Shelf Science* 130, pp. 54–61. DOI: 10.1016/j.ecss.2013.03.022.

Waldschläger, Kryss and Holger Schüttrumpf (2019). "Erosion Behavior of Different Microplastic Particles in Comparison to Natural Sediments". *Environmental Science and Technology*. DOI: 10.1021/acs.est.9b05394.

Wang, Chang Yi (1977). "Final stage of a falling plate". *Physics of Fluids* 20.1, pp. 164–165. DOI: 10.1063/1.861706.

Wickham, Sara B. et al. (Feb. 2020). "Sea wrack delivery and accumulation on islands: Factors that mediate marine nutrient permeability". *Marine Ecology Progress Series* 635, pp. 37–54. DOI: 10.3354/MEPS13197.

Wickramarachchi, Charuni et al. (2026). "Rethinking Vertical Transport of Buoyant Plastics in Open Channels".

Yeh, Harry H., Abdulhamid Ghazali, and Ingunn Marton (1989). "Experimental study of bore run-up". *Journal of Fluid Mechanics* 206, pp. 563–578. DOI: 10.1017/S0022112089002417.

Yih, Chia Shun (1974). "Fluid mechanics of colliding plates". *Physics of Fluids* 17.11, pp. 1936–1940. DOI: 10.1063/1.1694647.

Yu, Zijian et al. (Aug. 2023). "Investigation of the Sheltering Effects on the Mobilization of Microplastics in Open-Channel Flow". *Environmental Science and Technology* 57.30, pp. 11259–11266. DOI: 10.1021/acs.est.3c02500.

Zhang, Qinghai and Philip L.F. Liu (Dec. 2008). "A numerical study of swash flows generated by bores". *Coastal Engineering* 55.12, pp. 1113–1134. DOI: 10.1016/j.coastaleng.2008.04.010.